Development of Aluminum-Based Dissolvable Alloys for Hydraulic Fracturing Applications

by

Ezz Qaderi Ahmed

A thesis submitted in partial fulfillment of the requirements for the degree of

Master of Science

in

Materials Engineering

Department of Chemical and Materials Engineering
University of Alberta

Abstract

The application of dissolvable materials is becoming widely used in hydraulic fracturing, especially in low permeability reservoirs. To date, most of the DAs are based on Al alloys (AAs) or Mg alloys, which offer desirable dissolvability, yet limited mechanical properties. This work aims to develop a series of new Al-based DAs with desirable dissolution and mechanical strength.

Given the enormous possibilities in tunning the structures and compositions of potential DAs, a literature review was initially done to summarize the effects of various alloying elements on AAs. It was found that the abundant electrochemical data in the literature were reported in NaCl solutions, while the downhole environments contained KCl. Therefore, electrochemical studies were performed to analyze the cation type effects (K^+ vs. Na^+) on AAs. It was concluded that the associated cation type had insignificant effects on the corrosion behavior of the selected AAs, and the electrochemical data obtained from the literature in NaCl environment could be used for the selection of the alloying elements for the design of the new Al-based DAs. The selected alloying elements are Ga, In, Sn, (GIS), and Ag, which are expected to give the desired dissolvability, as well as Cr and Zr to enhance the mechanical properties.

The base alloy of Al-Zn-Cu-Mg was used in this study. After the selection of the alloying elements, Taguchi's method (L27) was utilized to change the chemistry of the base alloy to facilitate the design and further investigate the elemental selection. Scheil-Gulliver model was used to predict the phases formed as well as their fractions through ThermoCalc simulations. The results predicted the formation of 6 main phases: α-Al, η-$MgZn_2$, Mg_2Zn_{11}, Mg_2Sn, θ-Al_2Cu, Al_3Zr, and $Al_{45}Cr_7$ in all the alloys. Based on the simulation results, DA13, DA18, DA25, and DA27 were targeted as they had considerable fractions of desired phases (i.e., η-$MgZn_2$, Mg_2Zn_{11}, and θ-

Al_2Cu) and were anticipated to potentially yield high mechanical properties and active corrosion behavior.

The four selected DAs were further studied to evaluate the microstructure, corrosion behavior, and mechanical properties. The alloys were cast and machined for sample preparation. The microstructures of the DAs were analyzed using X-ray diffraction (XRD) and scanning electron microscopy with energy dispersive spectroscopy (SEM/EDS). Immersion corrosion tests were conducted to evaluate the corrosion behavior at 90 °C in 0.59 M KCl. For mechanical properties, hardness and tensile testing were performed on the as-cast alloys. The results presented the formation of the main predicted phases distributed in the as-cast microstructure, namely, $\eta\text{-MgZn}_2$, Mg_2Sn, $\theta\text{-Al}_2\text{Cu}$, Al_3Zr, and $\text{Al}_{45}\text{Cr}_7$. The results also suggested there existed a trade-off between dissolvability and mechanical properties. The presence of low melting point intermetallic phases was crucial for the dissolvability of the alloys. DA18 (containing the highest GIS content of 3 wt.%) corroded intensely (177.76 mg/cm^2 h) compared to the alloys with less GIS content, yet its mechanical properties were at their minimum (46.27 MPa for UTS and 113 HV for the microhardness). All the DAs were reported to be brittle with limited elongation (maximum elongation was 0.053% for DA27). It was concluded that In-containing phases are the main source of Al degradation. In addition, the presence of coarse phases tended to reduce the strength of the alloy (besides the liquid embrittlement caused by GIS phases).

PREFACE

This thesis is an original work by Ezz Ahmed under the supervision and edition of Dr. Jing Liu, Dr. Hani Henein, and Dr. Ahmed Qureshi.

Part of Chapter 2, Chapter 3, and Chapter 4 has been published and presented as *Ahmed, E., Henein, H., Qureshi, A., Liu, J. (2022). Development of Aluminum-Based Dissolvable Alloys for Hydraulic Fracturing Applications. In: TMS 2022 151st Annual Meeting & Exhibition Supplemental Proceedings. The Minerals, Metals & Materials Series. Springer, Cham.*

DEDICATION

To my family and wife, I would not have made it without your faith in me and your continuous encouragement. I am so grateful to have you close even though the distance, Thank you!

ACKNOWLEDGMENTS

First and foremost, I would like to express my deepest acknowledgment and gratitude to my advisors Dr. Jing Liu, Dr. Hani Henein, and Dr. Ahmed Qureshi for their time, effort, and guidance during the course of the program. Without your encouragement and mentorship, I would have not become the researcher I am today. I will always be so grateful for believing in me and pushing me forward.

Thank you to Marcellino, Meifeng, Ry, and Aleeza for your exceptional help in my experimental work.

To my research colleagues, thank you for your continued support and your friendship. You made me feel I was not in this alone. It has been a pleasure to work alongside each of you – Haoxiang, Daniella, Yeifan, Idil, Bilal, Lucas, Haofei, Henery, Vanda, Emily, and Ben.

Thank you to all my friends, you made Canada feels like home.

Finally, I would like to acknowledge the financial support of the Natural Science and Engineering Research Council of Canada (NSERC) and the Hadhramout Foundation (HF).

Contents

List of Figures

List of Tables

List of Abbreviations

AA: Aluminum alloy.	4
BSE: Backscattered electrons.	31
DA: Dissolvable alloy.	3
DFP: Dissolvable frac plug.	3
EDS: Energy dispersive spectroscopy.	31
GIS: Gallium, indium, and tin.	11
IGC: Intergranular corrosion.	8
LPR: Linear polarization resistance.	21
MLI: Mean linear intercept.	35
OCP: Open circuit potential.	21
RE: Reference electrode.	21
SE: Secondary electrons.	31
SEM: Scanning electron microscopy.	31
SG: Scheil-Gulliver.	27
WE: Working electrode.	21
XRD: X-ray diffraction.	31

List of Symbols

λ: wavelength.	34
A: Surface area (cm^2).	38
B: Stern-Geary coefficient (V).	22
b_a: Anodic Tafel slope (V/decay).	22
b_c: Cathodic Tafel slope.	22
CR: Corrosion rate (mg/cm^2 h).	38
D: Density (g/cm^3).	38
d: Interplanar spacing.	34
f_s: Fraction of the solid formed.	27
i_{corr}: corrosion density (A/m2).	22
K: Constant for unit conversion.	38
k_i: Partition coefficient.	28
n: The order of reflection (an integer).	34
T: Time (h).	38
W: mass loss (g).	38
x_0: Initial composition of the alloy.	28
$x_{s,i}$: composition of a solid phase,	27
ρ: Density (g/m^3).	22

Chapter 1. Introduction

1.1 Background

Multi-stage hydraulic fracturing by plug-and-perf is one of the most successful and economical methods for oil and gas extraction in unconventional reservoirs [1]. Since hydraulic fracturing was developed on a commercial scale in 1949, the frac plug technology has undergone three distinct step changes based on construction materials. Walton et al. [2] summarized these three stages into cast iron (1950s through 1990s), composite with the birth of the horizontal completion (1990s – Today), and dissolvable materials – (2010s-Today). Hydraulic fracturing technologies have been utilized in more than 175,000 wells over the last 60 years in Western Canada [3]. Figure 1.1 shows the production of tight oil (i.e., light oil being extracted via horizontal wells and multi-stage hydro-fracturing) over the course of time between 2005 and 2013. The exponential growth reflects the intensity of the increasing usage of hydraulic fracturing technology over the period. By 2035, it is forecasted that the tight and shale gas production will occupy 80% of the natural gas production in Canada [4].

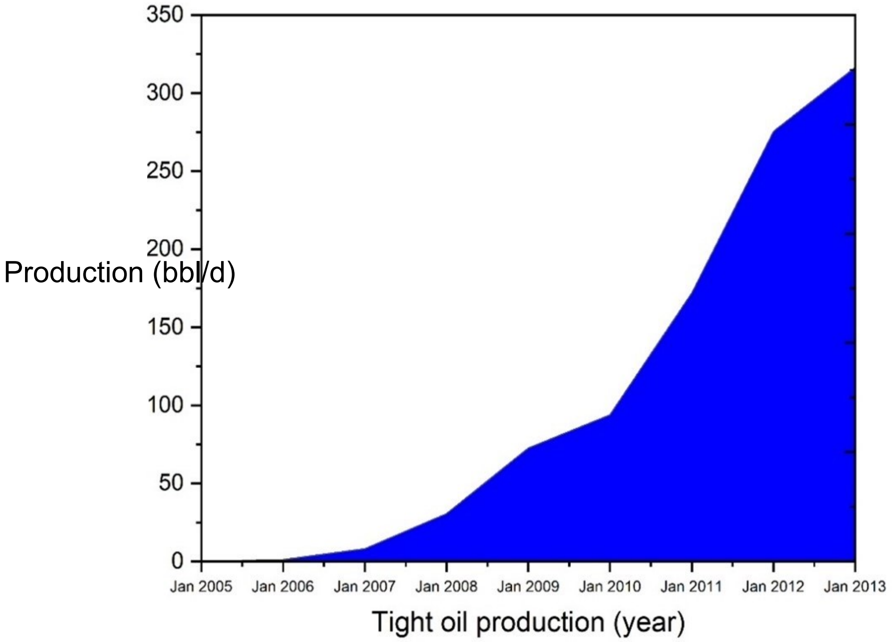

Figure 1.1. The exponential growth of tight oil production between 2005 and 2013 [4].

All plug-and-perf systems require frac plugs to isolate zones in a wellbore. Initially, perforation guns are used to create perforations into the formation at the desired distance of the horizontal well at the well toe. Fluids are then pumped down a well at high pressures into a formation to complete the first stage of fracking. The fracturing fluid is mainly composed of water and sand (99 percent), plus a number of process-improving chemicals [3]. The frac plug is set at the desired distance to isolate the previously fractured zone to perforate the second stage. The process is then repeated until all stages are fractured. The frac plugs then need to be removed (using coil tubing) before the well is put into production. Traditional frac plugs are constructed from cast iron, composite materials, and non-dissolving elastomers. The mill-out process is costly, problematic, risky, and can sometimes lead to production delays [5]. Inevitably, this inspired the idea of a dissolvable plug that would simply vanish and resolve the issues in milling-out processes.

The use of degradable materials, such as polyglycolic acid (PGA) and dissolvable Magnesium (Mg) alloys, provide an effective method to solve the issues related to the mechanical interventions needed for milling out. Successful application of dissolvable materials in multi-stage hydraulic fracturing was reported. Li et al. (2018) [6] provided a case study discussing issues encountered in Weiyuan Gasfiled including blocking and sticking. As traditional mill out was not applicable, the use of a fully dissolvable frac plug (DFP) was reported successful. Barker Hughes developed a dissolvable nano-structured material [7]. Magnum Oil Tools International also reported the development of a new dissolvable material called Magnum Fastball DM [8].

1.2 Motivation

Driven by efficiency and advancements in available materials, dissolvable materials are currently used to create DFPs that greatly reduce the need for milling with coiled tubing. At the end of 2017, roughly 2% of all frac plugs deployed in the field were made of dissolvable metals. The market is expected to grow to over 5% of all frac plugs deployed in the field through 2025 [9]. DFPs are made of dissolvable materials and designed to degrade completely leaving an unrestricted wellbore for production. DFPs are applied in a downhole environment containing roughly 3-4 wt.% KCl aqueous solution at temperature and pressure ranges from 80 – 120 °C and 50 – 70 MPa, respectively [10–12]. Ideally, the dissolution rate (at 90 °C, 4.46 wt. % KCl) for a dissolvable alloy (DA) is in the range of 35 mg/cm^2 h with yield strength, ultimate yield strength, and elongation of 125 MPa, 171 MPa, and 2 %, respectively, at room temperature. Obviously, material selection is the key. The selected high-strength dissolvable metal must allow dissolution in water-based wellbore fluid, formation fluid, or production fluid [13]. Downhole chemistry and temperature are the two primary variables considered when determining the right material composition for dissolvability in any given application. Most alloys used in today's DFPs are Mg or Aluminum (Al)-based, also requiring that the operator understands the exact chemistry of the well fluid to predictably estimate how long it will take for that plug to dissolve. However, downhole chemistry changes constantly. It varies dramatically from the vertical to the heel, and from heel to the toe. It varies from one well to the next, even on a multi-well pad. It is affected by the original water source and the fluid being pumped into the well. With so many variables, predicting how long it will take for the plug to dissolve is complicated. In turn, the material selection for desirable DFPs is complicated.

As promising materials, Al and Al alloys (AA) have favorable properties that if exploited properly, can yield the desired controlled dissolution and the necessary mechanical strength. Even though pure Al possesses desirable corrosion rates, Al is a soft, ductile, and relatively weak material to be utilized in the target downhole application [14]. The low strength can be compensated by alloying with other elements such as Mg, Zn, Cu, etc. AA 7075, 7050, and 7049 are AAs with high strength, among which AA 7075 possesses the highest strength [15]. The high mechanical properties of AA 7075 make it a good base material for the development of dissolvable alloys (DAs), yet its corrosion behavior needs to be adjusted to adapt to the targeted dissolvability in wellbore conditions. Another downside of AAs is the formation of stable protective oxide film formed on the surface, which in turn passivates its electrochemical (EC) activity. Al activation can be approached by (1) depassivation, i.e., alloying with low melting point metals (e.g., Ga, In, Sn and their respective low melting point intermetallic phases with Mg, Zn, etc.) [16], and (2) micro-galvanic corrosion, i.e., alloying with elements that trigger localized galvanic corrosion such as Ag [12]. The alloying elements' search space, as well as the elemental composition ranges, are huge. Furthermore, most corrosion data found in the literature are reported in NaCl electrolytes, while wellbore fluid creates environments containing KCl solution – adding another challenge to overcome.

1.3 Research objectives

This work aims to develop a series of new Al-based DAs, providing faster corrosion rates and ideally high material strength than current DAs for hydraulic fracturing applications. Four objectives are defined below.

- Objective 1: literature review. Given the enormous possibilities in tuning the structures and compositions of potential DAs, a literature review was first done to summarize the effects of various alloying elements on the microstructures, corrosion resistance, and mechanical properties of AAs.

- Objective 2: alloying element selection. The main chemistry in downhole environments is KCl while the abundant electrochemical data of AAs are in NaCl electrolytes. To maximize the available electrochemical data of AAs, the effects of the associate cation type (K^+ vs. Na^+) on the corrosion of selected alloys were investigated by comparing the electrochemical values obtained under the same Cl^- molar concentration of KCl vs. NaCl solutions. Objectives 1 and 2 lead to the compositions of potential Al-based DAs with a group of targeted alloying elements (with wt.% ranges).

- Objective 3: prediction of intermetallic phases. Phase simulation with ThermoCalc software and Scheil-Gulliver’s model was done to predict the to-be-formed phases in the potential Al-based DAs. Based on the simulation results, the most promising DAs that would yield a high corrosion rate and good mechanical strength were selected for further analysis.

- Objective 4: casting and performance evaluation of the selected DAs. Four DAs recommended in objective 3 were cast. After casting, microstructure characterization, corrosion, and mechanical behaviors of the newly designed Al-based DAs were investigated in detail.

1.4 Outline

The thesis is structured into four main chapters as follows.

In Chapter 2, a literature review is conducted on corrosion phenomena related to Al dissolution, activation of Al corrosion, and alloying elements' impact on dissolvability and mechanical properties of AAs. Chapter 3 presents the experimental procedures taken to produce and evaluate the DAs understudy. The results and discussion are covered in Chapter 4 in which the cation type effects, the intermetallic phases prediction, the microstructure characterization, and corrosion and the mechanical performance of the new DAs are presented. Finally, in Chapter 5, a summary of the significant results, as well as the possible future directions regarding the topic, are addressed.

Chapter 2. Literature Review

Common structural AAs often offer good corrosion resistance due to the passive films formed on the surface. This film will behave as a barrier to slow down or prevent further electrochemical reactions between Al and water. In order to obtain a fast corrosion rate, the breakdown of this barrier is necessary to activate the Al corrosion reactions. Therefore, Chapter 2 first reviews the depassivation, i.e., activation of Al corrosion mechanisms. Furthermore, several studies gave insight into how to promote the reaction between Al and water by means of alloying Al with different elements, like Al-In-Ga, Al-Zn-Ga [17], Al-In [18], and Al-Zn-In [19]. Other alloying elements such as Hg, Sn, and Bi have also been reported to shift Al's potential to the more electronegative direction [20–22]. Alloying elements can change the microstructure and the morphology of the second phases significantly, causing a change in the mechanical behavior of AAs [23]. The second part of this review focuses on the effects of the alloying elements on the dissolvability (i.e., corrodibility) and mechanical properties of various AAs. Chapter 2 leads to the compositions of potential Al-based DAs with a group of targeted alloying elements (with wt. % ranges).

2.1 Activation of Al Corrosion

It is known that pure Al forms a continuous passive layer when contacted with water. This film prevents the hydrolysis reaction of Al, yet the breakdown of the protective layer gives the light metal application in cathodic protection and energy storage systems. Therefore, this study considers Al depassivation, and intergranular galvanic corrosion to achieve the desired degradable AA. The thin 100 A° passive layer normally formed on the Al surface at ambient conditions prevents the continuous reaction of Al with water [24]. The reaction is presented by

$$Al + 3H_2O \rightarrow Al(OH)_3 + 1\frac{1}{2}H_2$$

(2. 1)

Production of hydrogen gas that can be utilized in other engineering applications [25]. The breakdown of the protective layer, or in other words, the activation of Al has been a focal point of many studies [26–31]. One method to promote the reaction is by using an alkaline solution [32, 33]. The first step in the Al oxide layer dissolution involves the adsorption (at a sufficient rate) of the reactive anion such as chloride on the charged surface of the oxide layer [34]. After which the chloride anions penetrate the film and react with Al ions causing depassivation of the protective layer [34, 35]. This in turn exposes the metal surface to direct corrosion attacks, as depicted in Figure 2.1.

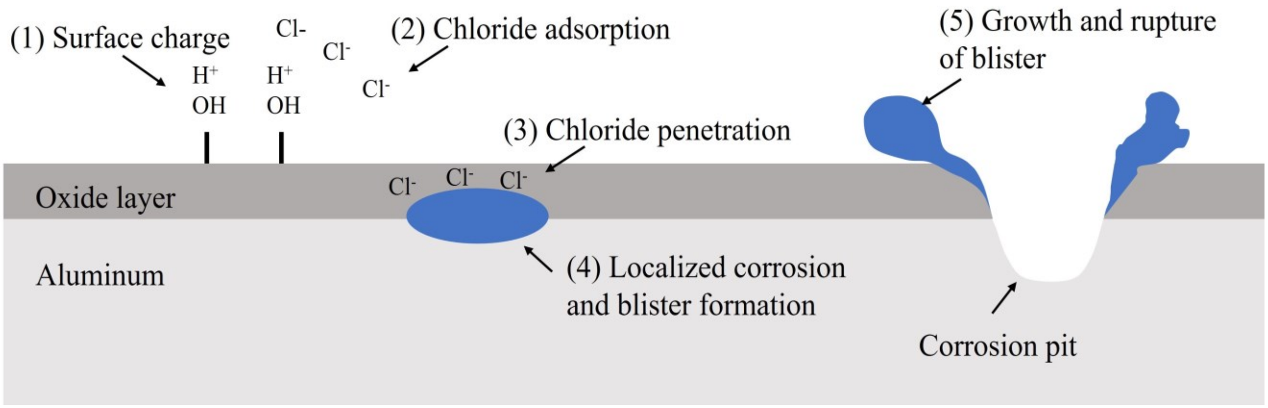

Figure 2.1. Illustration of localized corrosion of Al in presence of chloride (Cl^-).

Intergranular corrosion (IGC) is another type of localized corrosion. This form of micro-structurally influenced corrosion takes place preferentially at grain boundaries and the matrix or adjacent alloy microstructure [36, 37]. This phenomenon occurs in most alloys when exposed to an appropriate environment. AAs, for instance, are susceptible to IGC in chloride solutions due to the formation of hardening phases upon certain heat treatment. As depicted in Figure 2.2, when the micro-galvanic cell is developed, the anodic Al matrix gives away electrons migrating to the cathode at which reduction reactions take place. The cathodic intermetallic particles in the grains and grain boundaries do not dissolve. After the dissolution process, the corrosion products do not interfere with the production process of gas and oil [12]. The presence of more noble phases makes the Al matrix prone to corrosion as is the case in Al-Cu alloys owing to the precipitation of Al_2Cu which is nobler than Al. In Al-Mg alloys, however, the formed intermetallic phase of Mg_2Al_3 is more active than the Al matrix. Therefore, the degradation of the dissolvable Al-based alloy will involve the reaction of the cathodic phase and the anodic Al matrix in the presence of the wellbore fluidic environment.

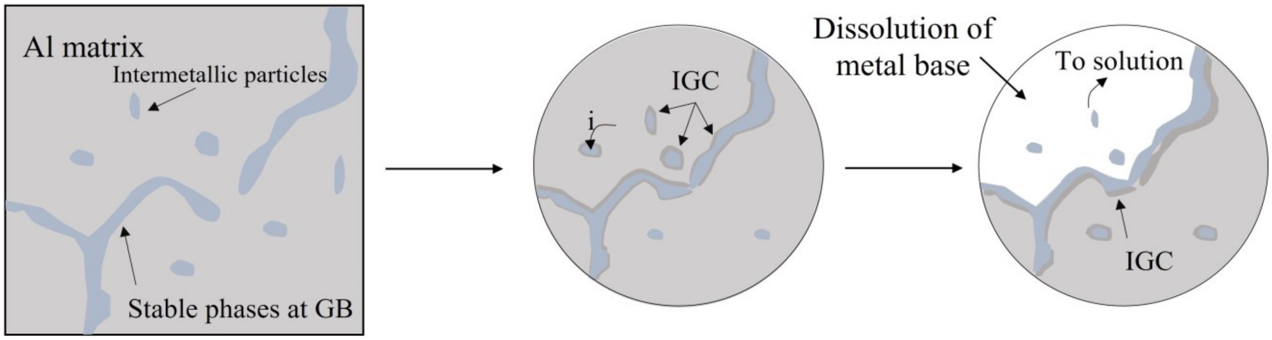

Figure 2.2. Presentation of the dissolution of the anodic phase (Al matrix) and the cathodic phases (intermetallic phases) in intergranular corrosion.

In addition, alloying with low melting point metals has also been reported effective in breaking down the passive layer [38, 39]. Woodall et al. [40] proposed a mechanism for the continuous hydrolysis reaction in Al-Ga and Al-Ga-In-Sn alloys. The reaction starts at a liquid phase of Ga-In-Sn containing Al particles. As shown in Figure 2.3, upon contact with water, Al atoms in the liquid phase first react, disturbing the equilibrium of the grain boundaries. This in turn enables

Al atoms to diffuse into the grain boundaries where the hydrolysis reaction is taking place. The reaction continues consuming Al atoms and generating hydrogen and Al oxide. Another reason for continuity of the reaction is that Al does not passivate as is the case in pure Al. A detailed review of the effects of alloying elements is presented in the following section.

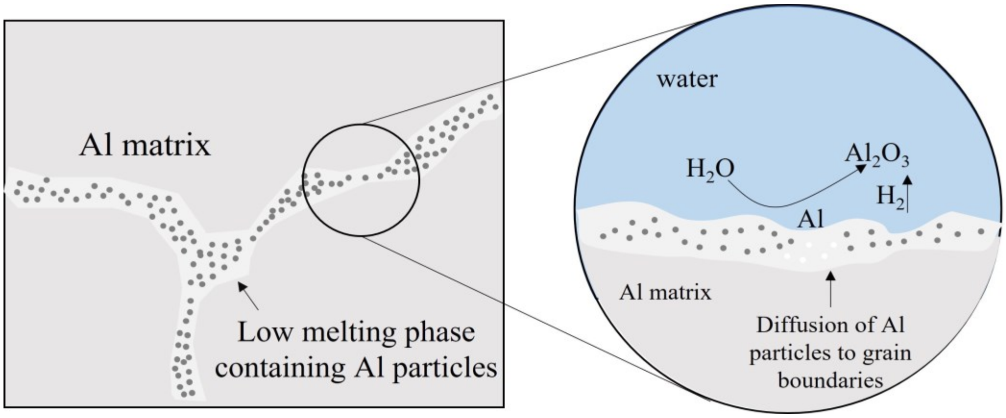

Figure 2.3. Schematic of the continuous hydrolysis reaction of Al.

2.2 Effects of alloying elements on the dissolvability and mechanical properties of Al alloys

Given the enormous possibilities in tuning the structures and compositions of potential DAs, a literature review is presented below to summarize the effects of various alloying elements on the microstructures, corrosion resistance, and mechanical properties of AAs. The alloying elements considered in this study are Ga, In, Sn, Mg, Zn, Cu, Ag, Cr, Er, and Zr. The selection was initially made based on the known effects those elements have on the mechanical properties as well as the electrochemical behavior of Al and AAs.

2.2.1 Effects on the corrodibility

First of all, there are lots of corrosion studies on AAs with various alloying elements, yet most of the published data was obtained in NaCl electrolytes [41, 42, 51, 43–50]. For example, Figure 2.4 presents the corrosion potentials of various intermetallic phases usually found in AAs in different NaCl concentrations [37]. The corrosion potentials of the phases give an insight into whether Al matrix would act as an anode or as a cathode with respect to the formed phases. However, one should question if the data in NaCl solutions found in literature applies to the KCl environment of a well. This question will be investigated in terms of cation effects (Na^+ vs. K^+) on corrosion at the same Cl^- concentration. To maximize the available electrochemical data of AAs, the corrosion data of AAs in NaCl electrolytes were considered at the review stage. These values provide insight into the dissolution of the targeted design of the dissolvable AAs.

Ga-In-Sn (GIS). As previously mentioned, the designed AAs will be dissolvable if the low melting point intermetallic phases are present. Different alloying elements can be added to Al to yield such phases, such as Ga, Hg, In, and Sn. The activation of Al by adding Ga, In, and Sn has been investigated by several researchers [16, 52–54].

Ziebarth et al. [52] studied the effect of the liquid GIS phase on a bulk AA. The liquid GIS phase, with a melting point of 10.4 °C [55], is the key factor for the depassivation of Al-Ga-In-Sn alloy. It was confirmed that Al present in the liquid Ga or GIS phases first reacted with water. The consumed Al in the reaction causes a drop in Al equilibrium concentration. This results in a chemical potential gradient as the driving force for Al diffusion from grains. This in turn consumes Al atoms in the alloy as the hydrolysis reaction continues.

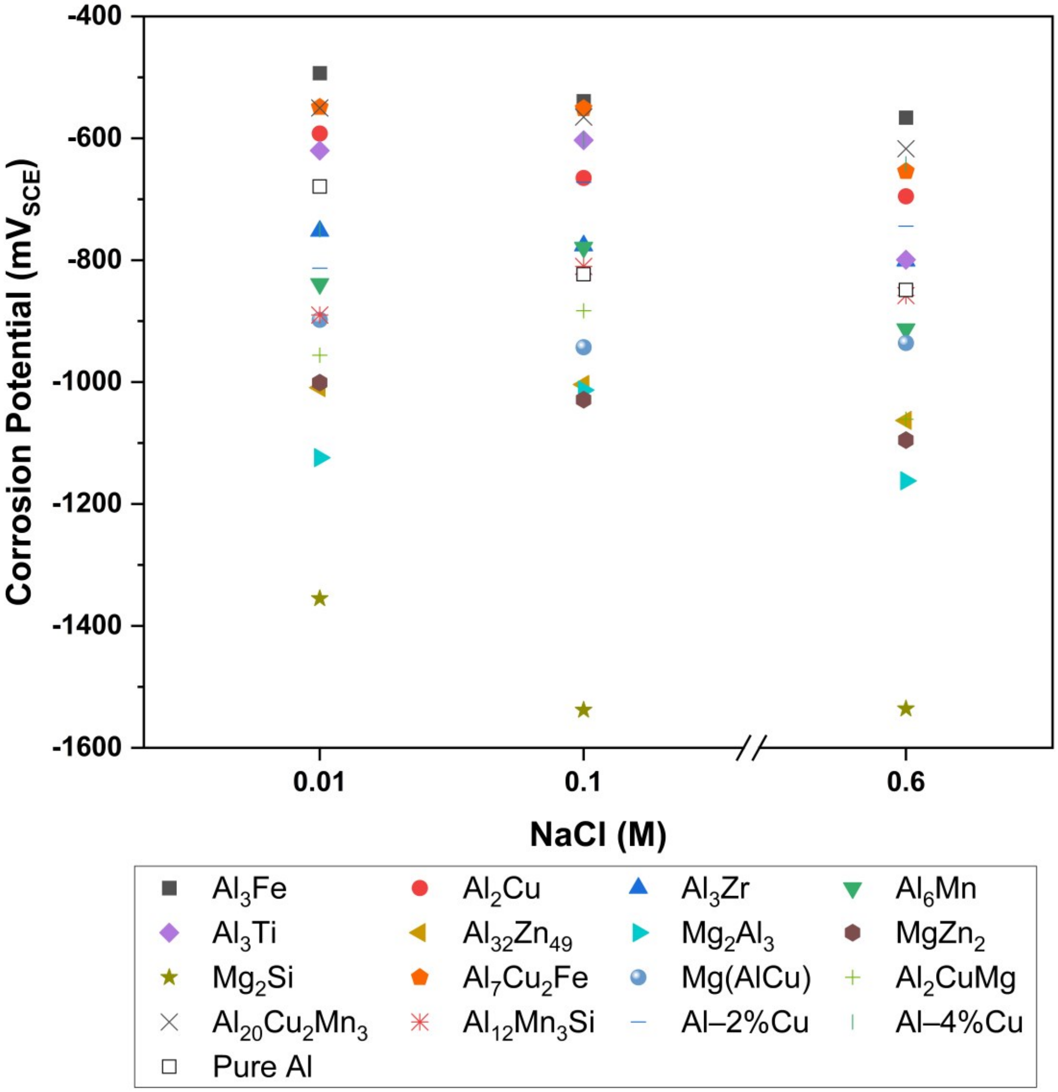

Figure 2.4. Corrosion potentials of intermetallic phases are common in AAs in NaCl solution [37].

On the other hand, intermetallic phases such as $TiAl_3$ and Al_2Cu do not involve in the reaction [54]. He et al. [53] studied the microstructure and interface reactions of Al-Ga-In-Sn alloys, with different In/Sn mass ratios. It was concluded that the activation of Al did not necessarily take place in the presence of the GIS eutectic. Other GIS mixtures, Ga with β (In_3Sn) and γ ($InSn_4$), could also dominate Al activation at reaction temperatures of their respective melting points. Al-Ga-In-Sn alloy exhibits high reactivity with water at GIS eutectic composition at mass ratios of Ga:In:Sn = 65:22:13, thus, the alloys considered in this study have total GIS composition ranges of 1.5, 3, and 6 wt.%, at which a high activity is achieved [53, 56]. Nevertheless, it is believed that adding Ga, In, and Sn will increase the corrosion of AAs; the lower end of 1.5 wt.% GIS content is chosen here to address the concern of liquid embrittlement caused by those low melting point metals.

Zn, Cu, and Mg. Another way to interfere with the protective oxide films of Al is by adding Zn. Several studies reported the effectiveness of this method, especially in Al-air battery anode [41, 46, 49, 57]. Zn addition in the Al electrode resulted in a more active potential in alkaline solutions, owing to the formation of Zn passive films [58]. Ternary Al-Zn-X alloys (where X is Ga, In, or Sn) have been shown to possess a more electronegative behavior. Al-Zn-Ga exhibits a ternary eutectic at 23 °C with the composition of Al-2Zn-14Ga. Aragon et al. [57] suggested that the mechanism for Al activation is similar to the liquid GIS eutectic discussed above. Venugopal and Raja [46] investigated the influence of In and Zn on the electrochemical behavior of Al-Zn-In alloy in a chloride medium. The researchers also observed In segregation owing to its low solubility in both Zn and Al according to their phase diagrams. This in turn promotes intergranular corrosion at In-rich and Zn-rich zones formed during solidification and surface diffusion. Further, similar behavior was observed by Khireche et al [49] in the study of Sn addition to Al-Zn alloy. Alloying Sn with Al-5Zn shifted the polarization curves to a more active position and increased the corrosion current density. No passive regions were observed in the Al-Zn-Sn alloys due to the active dissolution of Sn to $Sn(OH)_2$, SnO, and SnO_2 [59].

Figure 2.5 shows the effects of alloying with Zn, Cu, and Mg, respectively in Alx-Ga-In-Sn alloys (where x is Zn, Cu, or Mg) on the activation of Al in terms of hydrogen generation rates. It was confirmed that adding Cu or Mg hindered the hydrolysis reaction of Al. The reduction is more severe for Mg than Cu since Mg tends to form intermetallic phases with Ga, Sn, and In (i.e., preventing the formation of low intermetallic phases). The effect of Cu on the activation of Al was explained by the decrease in the contact area of the GIS phase with the Al matrix owing to the formation of the θ-Al_2Cu phase [60]. These particles tend to increase in size as more Cu is introduced into the alloy, hence the lower amount of hydrogen generation.

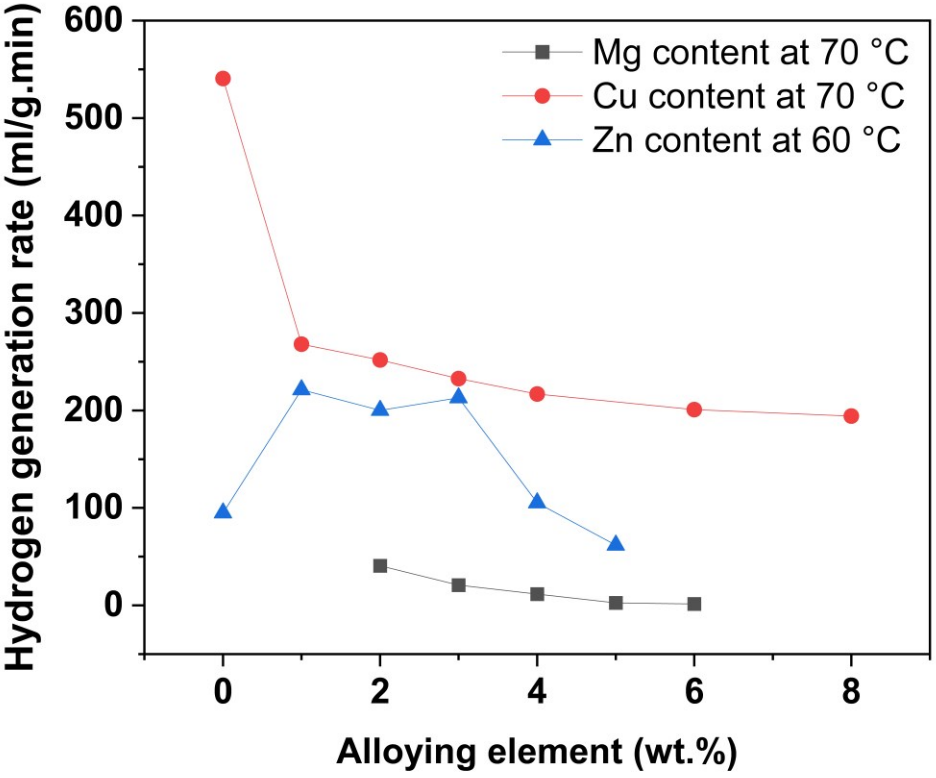

Figure 2.5. Effect of alloying elements content on hydrogen generation rate [56, 60–62].

Unlike alloying with Mg, the addition of Zn to Al-Ga-In-Sn alloy showed the presence of the In_3Sn phase [61]. However, the presence of Zn in grain boundaries dictates changes in Al and grain boundary phases (e.g., GIS phases) interactions. As Zn has a higher melting point than the other grain boundary phases, an increase in activation energy was confirmed causing a barrier to the hydrolysis reaction. Adding Zn up to 2 wt. % was reported to present no significant change in Al reactivity (i.e., micro-galvanic cells of Al-Zn compensate for the reduced effectiveness of GIS eutectic) while increasing Zn content up to 5 wt. % could decrease the dimensions of grain boundaries. The Al activity will then be hindered owing to the higher activation energy. [61] The Zn content in the base AA 7075 is 5.80 wt. %. Zinc will be adjusted for desirable Zn/Mg ratios. In addition, fixed Zn content in dissolvable Al and Mg alloys was reported to be 4-6 wt.% [17, 49, 62, 63]. This study will consider Zn content of 4 wt. % as a lower level (corresponding to a Zn/Mg ratio of 1.67), and of 12 wt. % as a higher level (corresponding to a Zn/Mg ratio of 5).

2.2.2 Effects on the mechanical properties

Even though AAs have a wide range of industrial applications for the excellent mechanical and physical properties they possess, the development of new AAs is continuing owing to the wide possibilities of improvement at hand. Those outstanding properties can be obtained using simple and affordable techniques such as alloying and/or heat treating. Zinc, magnesium, copper, silicon, iron, nickel, lithium, manganese, silver, tin, and titanium are some of the elements that can be added to Al [64]. The principal types of AAs obtain their strength by alloying with copper (2xxx series), manganese (3xxx series), silicon (4xxx series), magnesium (5xxx series), and zinc (7xxx series) [65]. The attention in this work will be directed to the age-hardening 7xxx series for better mechanical properties, the 7075 alloys in particular. However, the effect of the common alloying elements is briefly discussed in the following subsections.

Magnesium (Mg). Recently, the influence of alloying Mg in Al-Mg-Ga-In-Sn has been investigated [56, 66, 67]. According to the Al-Mg binary phase diagram [68], adding Mg greater than 2 wt. % enables the formation of the β phase (Al_3Mg_2). The formation of β phase and other grain-boundary precipitates, in higher Mg content alloys, has been related to stress corrosion cracking (SCC). These precipitates can be developed slowly at ambient temperatures, or the process can be accelerated at a temperature in the range of 37.78 to 176.67 °C [69]. Du et al. [56] examined the effects of varying Mg content in Al-xMg-3.8Ga-1.5In-0.7Sn with 2.4 wt. % Al-5Ti-1B as grain refiners. Binary phase diagrams predict the formation of MgIn, Mg_2Sn, $MgGa_2$, MgGa, $MgGa_2$, and Mg_5Ga_2 phases during solidification [68]. Interestingly, the formation of the In_3Sn phase reported previously [16, 53] was not observed when adding Mg in as-cast alloys. However, β-In_3Sn was present in the rapidly solidified alloys regardless of Mg addition [69]. The appearance of β-Al_3Mg_2 phase occurred only with Mg content at 5 wt. % and greater. Baer et al. [47] also concluded that the thickness of oxides remained unchanged, showing no impact on the dissolution of Al. Even though adding Mg could improve the mechanical properties of AAs, it potentially reduces the Al reactivity with water (i.e., reducing cathodic sites) [70]. The base material chosen for this study, AA 7075, has 2.1-2.9 wt. % Mg. Therefore, Mg will not be considered a design factor in this study.

Copper (Cu). As Cu has low solubility in Al at low temperatures (maximum solubility of 5.7 wt. % Cu at 550 °C [68]), changes in intermetallic phases at grain boundaries, especially low melting point phases, are expected owing to the formation of Cu-bearing intermetallics at grain boundaries. He et al [60] reported further increase in Cu content at grain boundaries occurred when Cu content increased up to 8 wt. %. In addition, they also found that the formation of θ-Al_2Cu led to a decrease in Al grain size. It was concluded that the addition of Cu to form Al-Cu-Ga-In-Sn alloys slows the reaction as the θ-Al_2Cu phase occupies GIS sites and decreases the Al-GIS contact area [60]. El Warraky et al. [42] investigated the impact of increasing the Cu content up to 11 wt.% on Al. It was shown that higher localized corrosion activity was obtained at higher Cu content. Moreover, Cu-bearing intermetallic phases such as S-Al_2CuMg and η-$Mg(Zn,Al,Cu)_2$ are susceptible to the de-alloying process in chloride solutions which further alter the corrosion behavior [71–73]. A wide range (4.1 – 11 wt. %) of Cu content would be considered in this study to show the influence of the amount and type of precipitates' phases on the corrosion and mechanical strength.

Silver (Ag). A small addition of Ag to AAs increases the mechanical strength through precipitation strengthening [74, 75]. In Al-Zn-Mg alloys, a small quantity of Ag reduces the width of precipitate-free zones (PFZs) owing to the increased nucleation site density; thus, improving mechanical properties [74, 75]. Moreover, Ag and Sn have a dual effect on improving the tensile properties of Al-Zn-Mg alloys [74]. In terms of corrosion behavior, Ag, as a noble metal, accelerates corrosion on other active metals since it does not readily polarize. Thus, localized galvanic cells between Ag particles and Al matrix would form and enhance corrosion [76]. The influence of Ag content on the mechanical properties and corrosion behavior would be considered in a range between 0.07 and 4.2 wt.%. The lower level would reveal the influence on mechanical properties based on the discussion above, while the higher level would give insight into the localized galvanic corrosion behavior.

Chromium, Zirconium, and Erbium (Cr, Zr, Er). The addition of Cr to Al not only reduces stress corrosion and improves toughness, but also controls grain structure and grain growth in Al-Mg-Si or Al-Mg-Zn alloys during heat treatment [77]. The intermetallic compounds are produced upon adding Cr and Zr to AAs, which also influence the corrosion behavior [75]. The addition of Cr will improve the corrosion resistance of AAs owing to the enhanced passivation due to the formed intermetallic phases as well as the increased Cr density in the solid solution [51]. H.C. Fang et al. [50] also studied the influence of alloying with Cr, Zr, and Er on the mechanical and electrochemical properties of Al-Zn-Mg-Cu alloys. They concluded that adding those alloying elements improved the mechanical and corrosion-resistant behavior as they would restrict the recrystallization at grain boundaries. It was observed that adding 0.16 wt. % Zr resulted in Ultimate Tensile Strength (UTS) and Yield Strength (YS) of 704.0 and 683.6 MPa, respectively, while adding 0.16 wt. % Zr, 0.3 wt. % Er, and 0.18 wt. % Cr resulted in UTS and YS of 743.9 and 728.1 MPa, respectively. Alloying with Zr alone shifted the corrosion potential to the more active position and did not decrease the corrosion current density compared with alloying with Zr, Er, and Cr together. AA 7075 has very few amounts of Cr and Zr, 0.19 and 0.02 wt. %, respectively. Therefore, Cr and Zr would be considered as grain refiners in this study, and their influence on mechanical properties would be studied up to 1 wt. % at a higher level.

2.3 Summary

To sum up, the design of the DA will consider the intergranular corrosion and the hydrolysis reaction of water through the low melting point phases. This work would put the scope on the alloying elements influencing the dissolvability and mechanical properties of the targeted DAs. The selected elements are:

- Ga, In, and Sn added at the GIS eutectic mass ratio of 68:22:13, respectively, and at the total composition of 1.5, 3, and 6 wt. %; expecting a boost in the corrosion rates of the designed alloys,

- Cu and Zn in lower and higher levels of 4.1 – 11 wt. % and 4 – 12 wt. %, respectively, as well as Mg at a fixed composition of 2.4 wt. %; forming intermetallic phases which enhance the mechanical properties,

- Ag in the range of 0.07 – 4.2 wt. %; forming micro-galvanic cells that enhance corrosion as well as improve mechanical properties via PFZs reduction,

- Cr and Zr as grain refiners in amounts up to 1 wt. %; expecting an increase in mechanical strength and control over grain growth and structure.

Chapter 3. Experimental Procedures

The materials and the experimental methods will be discussed in this section. The first objective was to investigate the effect of electrolytes' cation type on the corrosion of commercial AAs. This study was performed to confirm the applicability of the corrosion data tested in the NaCl environment found in the literature to the downhole environment that contained KCl. Electrochemical analyses (EC) were used to study the corrosion potentials (E_{corr}) and corrosion current densities (i_{corr}).

To design a new Al-based DA, the adapted experimental approach started with reviewing the effects of alloying elements on the corrosion behavior and mechanical properties. This provided a selection of promising elements with their compositional ranges, as concluded in Chapter 2. Then Taguchi's method (L27) was implemented as a robust design of experiment (DoE) to determine the chemistries of the alloys understudy. To reduce the number of experiments, hence the number of castings as well as the quantities of materials used, the 27 alloys resulting from the DoE were first investigated using Scheil solidification simulations. The Scheil solidification simulations predicted the phases potentially formed in each alloy along with their amounts. The corrosion behavior and mechanical properties can be altered by the present intermetallic phases. Therefore, Scheil simulation would give an insight into the most promising DAs out of the 27 alloys. Further analyses were carried out on the selected promising DAs including microstructural analysis, immersion measurements for corrosion (or dissolving) rates, and mechanical properties (such as hardness, UTS, elongation, etc).

In summary, the types of experiments adopted in this study are EC analyses, Taguchi's method (L27), solidification simulations, microstructure characterization, immersion measurements, and mechanical testing. Each of these experimenting techniques is described along with the used experimental procedures in the following subsections.

3.1 Electrochemical measurements

EC measurements allow for the characterization of corrosion properties of metals which gives insight into not only preventing and/or anticipating any harmful metal-environment interactions but also provide guidelines for developing corrosion-resistant alloys. Out of many EC techniques, two types of tests are adopted in our study: Open Circuit Potential (OCP) and Linear Polarization Resistance (LPR).

OCP measurements fall under no-applied-signal tests. It is the potential established between the working electrode (WE) and the electrolyte with respect to the reference electrode (RE). OCP is used for identifying the resting potential of a metal which can be used to predict the galvanic coupling of different metals [78]. One technique to measure the corrosion current density (i_{corr}) is the LPR. It provides measurements of corrosion rates in the vicinity of the corrosion potential (E_{Corr}) at different process conditions [79]. The polarization resistance (R_p) is inversely proportional to the corrosion current and is defined as [80]

$$R_p = \frac{dE}{di} \tag{3. 1}$$

LPR is a small-signal polarization method where a small potential scan is applied to a specimen while recording the resulting current. The polarization resistance can be determined by the slope of the potential-current curve. The corrosion density is related to the polarization resistance by the Stern-Geary equation [81]

$$i_{corr}(\mu A/cm^2) = 10^6 \frac{B}{R_p},$$

(3. 2)

where R_p is in Ω cm^2 and B is the Stern-Geary coefficient in V that can be calculated using Tafel slopes using

$$B = \frac{b_a b_c}{2.303\ (b_a + b_c)},$$

(3. 3)

where b_a and b_c are the anodic and cathodic Tafel slopes, respectively, in V/dec. The corrosion rates can be evaluated by knowing the corrosion current density by

$$CR\left(\frac{mm}{y}\right) = K\,\frac{i_{corr}EW}{\rho},$$

(3. 4)

where EW is the equivalent weight, ρ is the density in g/cm^3, and K is a constant with a value of 3.27×10^{-3} mm g/μA cm y [81].

In this work, OCP and LPR tests were conducted to study the effect of electrolytes' cation type on the corrosion potential and corrosion currents. Commercial AA 2024, AA 6061, AA 7075, and Al-based DA (Table 3.1) were used in EC testing. The samples were mounted in epoxy resin and were polished with SiC papers up to 600 grit. The exposed area for all specimens was approximately 1.00 cm^2. OCP and LPR measurements were performed using an EC potentiostat in aqueous NaCl and KCl solutions at the same Cl^- molar concentration. The wt. % concentration of KCl is 4.46 wt. %, which is calculated to be equivalent to 3.5 wt. % NaCl. The EC cell consisted of a three-electrode arrangement with the potential being recorded with respect to saturated Ag/AgCl reference electrode and graphite as a counter electrode (Figure 3.1). The EC cell was connected to VersaStat 3F Potentiostat workstation (AMTEK Scientific Instruments). LPR tests were performed in voltage ranging from -0.1 V vs OCP to 0.1 V vs OCP at a scan rate of 0.5 mV/s.

Table 3.1. Compositions (wt.%) of selected AAs.

Alloy	Zn	Mg	Cu	Ag	Ga	Cr	Fe	Si	Mn	Ti	Zr	V	Al
AA 2024	-	1.42	3.53	-	-	-	0.22	-	0.22	-	-	-	Bal.
AA 6061	0.05	1.00	0.32	-	-	-	0.50	0.73	0.03	-	-	-	Bal.
AA 7075	5.80	2.40	1.50	-	-	0.19	0.17	0.08	0.04	0.03	0.02	0.01	Bal.
Al-based DA	-	2.60	4.10	2.10	2.00	-	-	-	-	-	-	-	Bal.

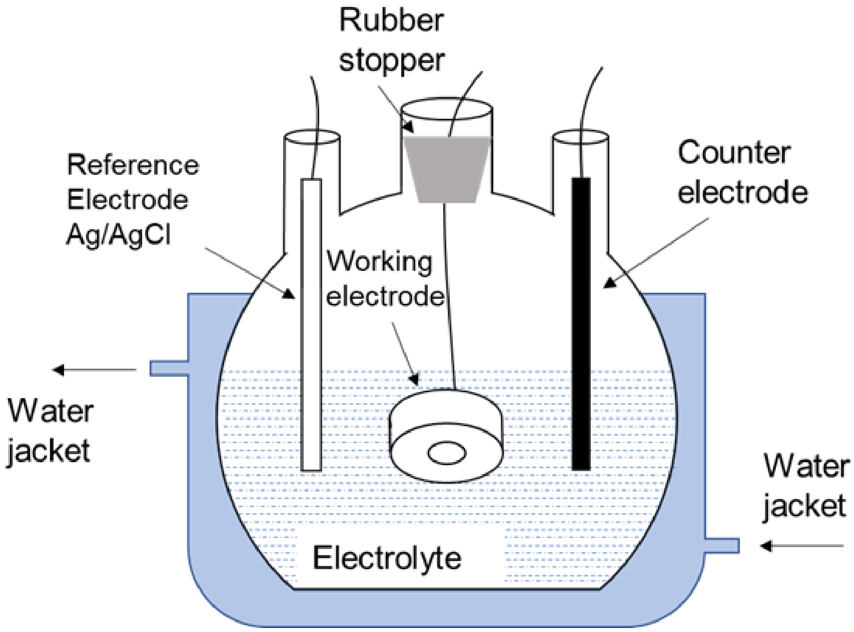

Figure 3.1. Schematic of a three-electrode electrochemical cell.

In addition, EC experiments were also performed to characterize the electrochemical behavior of the selected DAs understudy. OCP and LPR tests were conducted at 90 °C on approximately 1 cm^2 samples of the DAs mounted in high-temperature epoxy (service temperature up to 225 °C, MG Chemicals). The samples were mechanically prepared. Successive grinding using 320, 400, and 600 grit SiC grinding papers was used, after which the samples were cleaned with ethanol in an ultrasonic cleaner. The measurements were conducted in 0.59 M KCl solution in a three-electrode arrangement corrosion cell. The reference electrode used was saturated Ag/AgCl, and graphite was used as a counter electrode. OCP measurements were conducted for 21600 seconds (6 hours). After achieving equilibrium, LPR measurements were taken from -0.15 V to 0.15 V at a scan rate of 1 mV/s. versus OCP.

3.2 Taguchi's method and Scheil solidification simulations

The Taguchi method is a robust statistical technique that replaces a full factorial experiment with an Orthogonal array, minimizing the total number of tests. For this purpose, it is used to enhance the manufacturing processes industrially as it is insensitive to noise variables. [82] The total number of tests is dependent on the number of design factors to be studied as well as their levels. As previously concluded in Chapter 2, the Taguchi method (L27) was implemented with 6 design factors at 3 levels. The design factors considered for the simulation are the alloying elements with their compositional ranges. Table 3.2 summarizes the values for each respective design factor at each level. Further, the chemical compositions of the designed alloys considered for phase simulation are shown in Tables 3.3 and 3.4. Those alloys represent a systemic approach with L27 orthogonal array of Taguchi's method.

Table 3.2. Design factors and their range of study for the phase simulation analysis.

Design factors	levels	Values (wt. %)		
		Low	Mid	High
		-1	0	1
Cu	3	4.1	7.55	11
Zn	3	4	8	12
Ag	3	0.7	2.14	4.2
GIS	3	1.5	3	6
Cr	3	0.19	0.6	1
Zr	3	0	0.5	1

Table 3.3. Composition (wt. %) of the designed DAs used in the simulation.

DA	Cu	Zn	Mg	Ag	Ga	In	Sn	Cr	Zr	Ti	V	Al
1	4.10	4.00	2.40	0.70	0.88	0.37	0.25	0.19	0.00	0.03	0.01	87.07
2	4.10	4.00	2.40	0.70	0.88	0.37	0.25	0.60	0.50	0.03	0.01	86.16
3	4.10	4.00	2.40	0.70	0.88	0.37	0.25	1.00	1.00	0.03	0.01	85.26
4	4.10	8.00	2.40	2.14	1.75	0.75	0.50	0.19	0.00	0.03	0.01	80.13
5	4.10	8.00	2.40	2.14	1.75	0.75	0.50	0.60	0.50	0.03	0.01	79.22
6	4.10	8.00	2.40	2.14	1.75	0.75	0.50	1.00	1.00	0.03	0.01	78.32
7	4.10	12.00	2.40	4.20	3.80	1.50	0.70	0.19	0.00	0.03	0.01	71.07
8	4.10	12.00	2.40	4.20	3.80	1.50	0.70	0.60	0.50	0.03	0.01	70.16
9	4.10	12.00	2.40	4.20	3.80	1.50	0.70	1.00	1.00	0.03	0.01	69.26
10	7.55	4.00	2.40	2.14	3.80	1.50	0.70	0.19	0.50	0.03	0.01	77.18
11	7.55	4.00	2.40	2.14	3.80	1.50	0.70	0.60	1.00	0.03	0.01	76.27
12	7.55	4.00	2.40	2.14	3.80	1.50	0.70	1.00	0.00	0.03	0.01	76.87
13	7.55	8.00	2.40	4.20	0.88	0.37	0.25	0.19	0.50	0.03	0.01	75.62
14	7.55	8.00	2.40	4.20	0.88	0.37	0.25	0.60	1.00	0.03	0.01	74.71
15	7.55	8.00	2.40	4.20	0.88	0.37	0.25	1.00	0.00	0.03	0.01	75.31
16	7.55	12.00	2.40	0.70	1.75	0.75	0.50	0.19	0.50	0.03	0.01	73.62
17	7.55	12.00	2.40	0.70	1.75	0.75	0.50	0.60	1.00	0.03	0.01	72.71
18	7.55	12.00	2.40	0.70	1.75	0.75	0.50	1.00	0.00	0.03	0.01	73.31
19	11.00	4.00	2.40	4.20	1.75	0.75	0.50	0.19	1.00	0.03	0.01	74.17
20	11.00	4.00	2.40	4.20	1.75	0.75	0.50	0.60	0.00	0.03	0.01	74.76
21	11.00	4.00	2.40	4.20	1.75	0.75	0.50	1.00	0.50	0.03	0.01	73.86

Table 3.4. Continued composition (wt.%) of the designed DAs used in the simulation.

DA	Cu	Zn	Mg	Ag	Ga	In	Sn	Cr	Zr	Ti	V	Al
22	11.00	8.00	2.40	0.70	3.80	1.50	0.70	0.19	1.00	0.03	0.01	70.67
23	11.00	8.00	2.40	0.70	3.80	1.50	0.70	0.60	0.00	0.03	0.01	71.26
24	11.00	8.00	2.40	0.70	3.80	1.50	0.70	1.00	0.50	0.03	0.01	70.36
25	11.00	12.00	2.40	2.14	0.88	0.37	0.25	0.19	1.00	0.03	0.01	69.73
26	11.00	12.00	2.40	2.14	0.88	0.37	0.25	0.60	0.00	0.03	0.01	70.32
27	11.00	12.00	2.40	2.14	0.88	0.37	0.25	1.00	0.50	0.03	0.01	69.42

Calculation of phase diagrams (CALPHAD) has proven to provide high-quality results close to experimental observations for multi-component systems including AAs [83, 84]. It is based on the mathematical modeling of thermodynamic properties of individual phases, where thermochemical data and phase equilibria data are used to evaluate models' parameters [84]. CALPHAD considers the Gibbs energy of all phases and attempts to give a true equilibrium by minimizing the total Gibbs energy of the system. CALPHAD modeling has widely been used with the calculations of phase formation during solidification [85].

Conventional solidification processes are practically non-equilibrium, which can be described by the Scheil-Gulliver (SG) equation. SG model is a quantitative description of solute redistribution during solidification that has been widely used to simulate solidification processes. The model approximates non-equilibrium solidification and assumes local equilibrium achieved at the solid/liquid interface front. It also assumes no diffusion in the solid phase and fast diffusion in the liquid phase. [85–88] The model relates the composition of solid phases ($x_{s,i}$) with the fraction of the solid form (f_s) by

$$x_{s_i} = k_i x_0 (1 - f_s)^{k_i - 1},$$

(3. 5)

where x_0 is the initial composition of the alloy and k_i is the partition coefficient [89].

Implementing CALPHAD modeling enables the calculation of phases to form during solidification for a number of constituents. SG model was further improved by considering back-diffusion for systems containing fast diffusing elements in the solid. SG model with back-diffusion, similar to the classic SG model, assumes fast diffusion in the liquid phase and equilibrium at the solid/liquid interface. However, the difference lies in the diffusion of all elements in the primary solid phase, where the diffusion is calculated using mobility databases. If the degree of back-diffusion is small, the classic SG model can provide satisfactory results [85, 90].

In the present work, the classic SG model was used as a screening process for the selection of candidate DAs. Thermo-Calc software (2021b) was used to perform CALPHAD calculations and SG solidification simulations using the TCAL7 database that is designed for AAs.

3.3 New Alloy Casting

Four potential DAs out of the 27 alloys were selected based on the SG model results, which will be discussed in depth later in Chapter 4, and were cast for further experimental validation. The nominal compositions of these four DAs are listed in Table 3.5.

Table 3.5. Compositions of prepared alloy ingots (wt. %).

Alloy	Cu	Zn	Mg	Ag	Ga	In	Sn	Cr	Zr	Ti	V	Al
DA13	7.55	8.00	2.40	4.20	0.88	0.37	0.25	0.19	0.50	0.03	0.01	75.62
DA18	7.55	12.00	2.40	0.70	1.75	0.75	0.50	1.00	0.00	0.03	0.01	73.31
DA25	11.00	12.00	2.40	2.14	0.88	0.37	0.25	0.19	1.00	0.03	0.01	69.73
DA27	11.00	12.00	2.40	2.14	0.88	0.37	0.25	1.00	0.50	0.03	0.01	69.42

The ingots, 33 mm in diameter and 150 mm in length, were prepared using traditional melting and casting methods. Figure 3.2 shows the experimental setup for casting. Each ingot was melted in a clay graphite crucible at 1200 °C in a closed box furnace (CM Rapid-Temp, CM furnaces Inc.). The high temperature is to ensure the melting of the master alloys with a high melting point. The melt was stirred to ensure homogeneity of the alloys' composition. After stirring, argon gas was funneled into the melt to remove metal oxides before pouring into a pre-heated graphite mold at 600 °C. The used raw materials consisted of commercially pure Al, Mg, and Zn of 99.9, 99.8, and 99.9 wt. % purity, along with Ga, In, and Sn with purities of 99.9 wt. %. The commercial master alloys used were Al-33Cu, Al-15Ag, Al-5Cr, Al-5Zr, Al-5Ti, and Al-5V, supplied from Stanford Materials, US. Casting was repeated in order to ensure the reproducibility of the following experimental characterization.

(a)

(b)

(c)

Figure 3.2.Illustration of (a) box furnace, (b) clay graphite crucible, and (c) graphite mold.

3.4 Microstructure characterization

Conducting microstructure analysis provides in-depth characterization and reveals valuable information in different areas such as the performance of materials, failure mechanisms, and corrosion. Out of several techniques that can be used for materials characterization, scanning electron microscopy (SEM) with energy-dispersive spectroscopy (EDS), and x-ray diffraction (XRD) are the ones adopted in the present study.

SEM is a characterizing technique used for magnifying and imaging solid surfaces to examine their morphology. This is achieved through scanning an area of interest with a focused high-energy beam of electrons, which is produced by an electron gun under a vacuum [91]. Upon the incident of the beam on a sample surface, various signals are produced, mainly the backscattered electrons (BSE), secondary electrons (SE), and characteristic X-rays [91, 92]. The produced signals provide an insight into the topography of the surface as well as the specimen chemistry. BSEs are electrons from the primary electron beam that are scattered back from the surface and provide atomic number contrast [91, 92]. SEs are excited electrons previously existed on the sample's surface with energies less than 50 eV, which reveal a sample's surface topography [93]. SEM is a nondestructive evaluation technique that produces images of high resolution at magnifications reaching 300,000x, surpassing optical microscopy [93, 94]. It consists of two components: a microscope column and a control console.

The microscope column components can be further categorized into three parts: the electron optics, the specimen chamber, and the support system. As shown in Figure 3.3, the column optics consists of the electron gun, where the electron beam is generated, and two electron lenses (condenser lens and objective lens) that focus the beam into a small probe on the surface of the sample. The energy of the electron beam generated by the electron gun ranges from 0.1 to 30 KeV [93], while the beam is typically generated by thermionic sources (tungsten or La/CeB$_6$) or field emission sources (tungsten single crystal needles) [91, 95]. Through the use of electromagnetism, the lenses, which are made of copper wires coiled around iron fixtures, focus the electron beams to a focal plane in a similar manner as in an optical lens [95, 96]. A deflection system (i.e., scan coils) placed in the objective lens functions as a beam sweeper to scan a rectangular area on the surface of the sample that is placed inside the specimen chamber. The SEM chamber also contains the primary detectors (i.e., mounted to detect SEs and BSEs) as well as x-ray detectors, wavelength-dispersive spectrometers (WDSs), or energy-dispersive spectrometers (EDSs). X-ray detectors enable the quantification and the determination of the chemical characterization of a sample [97]. The SEM support system depends on its capabilities. However, the minimum requirement includes electrical power to yield the electron beam, and vacuum pumps for high vacuum conditions in both the column and the chamber. Further discussion on the supporting system can be found in [91].

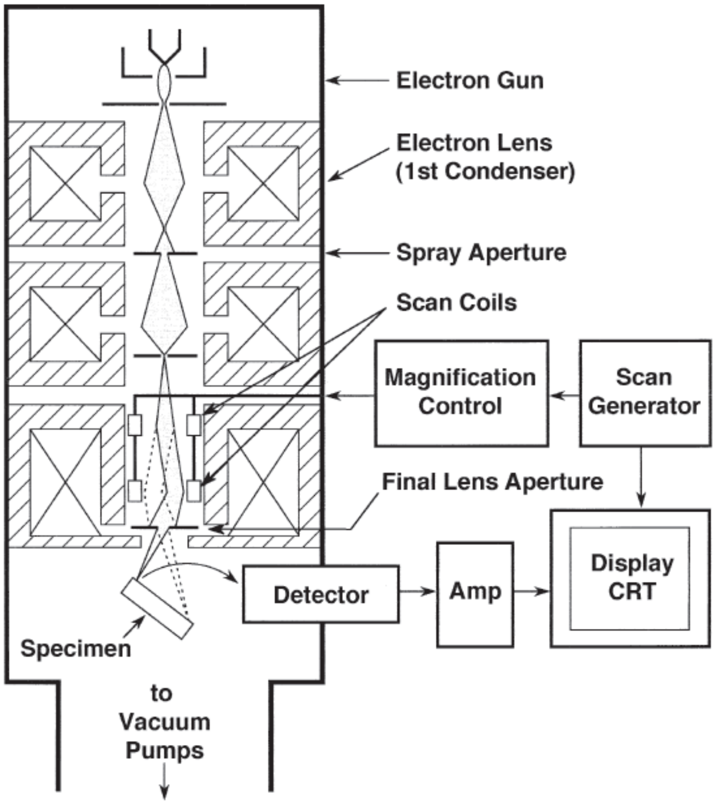

Figure 3.3. Schematic of basic SEM components [9].

XRD technique is a rapid and nondestructive test used to characterize crystalline materials. Application of XRD reveals information at an atomic level ranging from the crystallinity and structure of solid materials to phase identification [98]. XRD is based on the wide-angle elastic scattering of an X-ray beam passing through the specimen [99]. The constructive interference of scattered X-ray produces diffraction peaks (Figure 3.4a). The peaks are materials specific as they are determined by the atomic arrangement in a unit cell; therefore, the diffraction patterns can be used to identify phases and materials [100]. An X-ray diffractometer mainly consists of an X-ray source, a specimen mount, and an X-ray detector (Figure 3.4b).

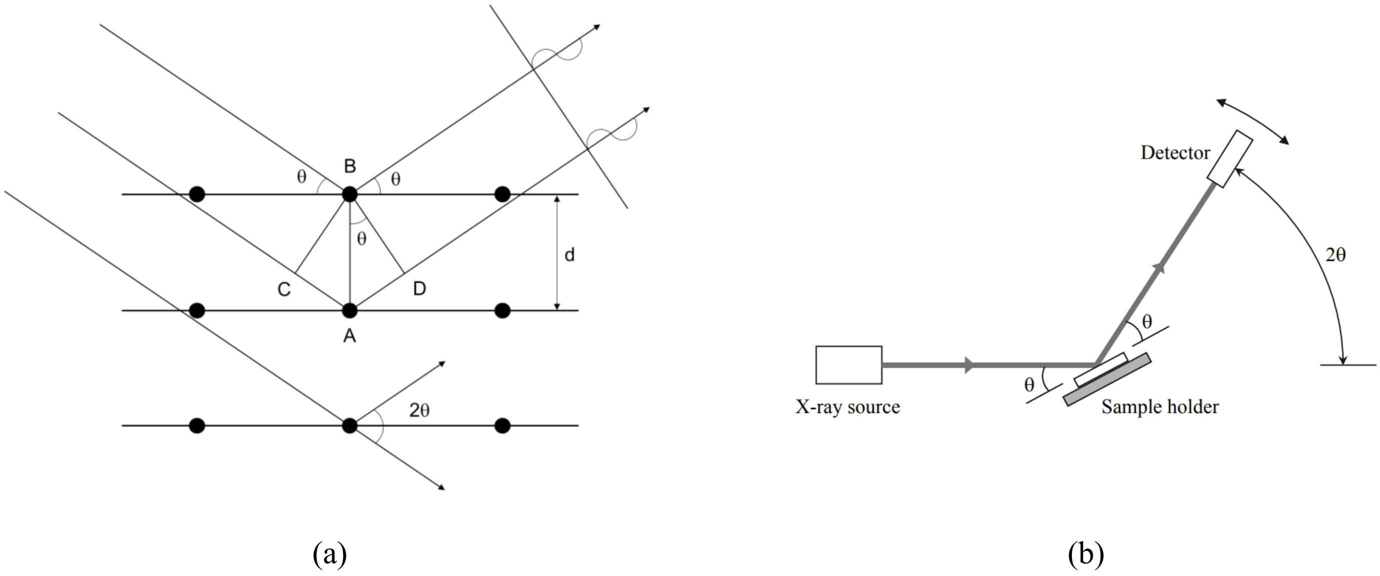

Figure 3.4. (a) X-ray diffraction by a crystal, and (b) schematic of XRD components [101].

The working principle of this method is Bragg's law, which relates the wavelength (λ) of the incident radiation with the spacing of the atomic planes by

$$n\lambda = 2d\ sin\theta, \tag{3. 6}$$

where d is the interplanar spacing, θ is Bragg's angle (i.e., the incident angle), and n is an integer (i.e., the order of reflection). Bragg's equation is satisfied when a peak intensity is observed. This in turn allows for the calculation of the interplanar spacing knowing the angles at which the peaks are observed. Peak searches are conducted on a computer where the observed patterns are matched with standard patterns utilizing commercial software (e.g., MDI/JADE – ICCD) for crystal structure and phase identification.

For the microstructure analysis in this study, the phase compositions were identified using Rigaku Ultima IV diffractometer using $Cu_{K\alpha}$ radiation generated at 40 kV and 44 mA. The scan of 2θ was collected in the range of 15° to 80°. The microstructure characterization was carried out using Tescan Vega3 SBH SEM equipped with Oxford EDS detector for chemical composition identification of phases. The ingots were cut along the vertical axis, and the samples were mounted in epoxy resin. Successive hand grinding and polishing steps were performed using oil-based suspended slurries (Table 3.6). Hand polishing was used instead of auto-polishing to minimize the pullout of low melting intermetallic phases. Keller's reagent (2.5 wt.% HNO_3, 1.5 wt.% HCl, 1 wt.% HF, and distilled water) was used to etch the specimens. The grain sizes were measured using the mean linear intercept (MLI) method according to ASTM E112-13 utilizing ImageJ software (v. 1.53e). The surface morphology of corroded samples, as well as tensile fractured specimen, were characterized using SEM for corrosion mechanism analysis and fractography.

Table *3.6*. Mechanical polishing procedures.

Abrasive/size	Surface	Speed rpm	Time
SiC - 600grit Alcohol cooled	CarbiMet Waterproof Paper	150	Until plane
SiC - 1200grit Alcohol cooled	ChemoMet Cloth	150	5
9 µm MetaDi Oil Based Dimond Slurry	ChemoMet Cloth	120	6
3 µm MetaDi Oil Based Dimond Slurry	ChemoMet Cloth	120	4
1 µm MetaDi Oil Based Dimond Slurry	ChemoMet Cloth	120	2

3.5 Immersion measurements

Immersion corrosion tests were carried out according to NACE TM0169/G31-21 standards [102]. The experimental setup consisted of a jacketed corrosion glass kettle of 1000 mL, rubber plugs, a specimen support system, and a water bath for temperature control. Two corrosion cell beakers were connected in series with a water bath to facilitate the experiments as shown in Figure 3.5.

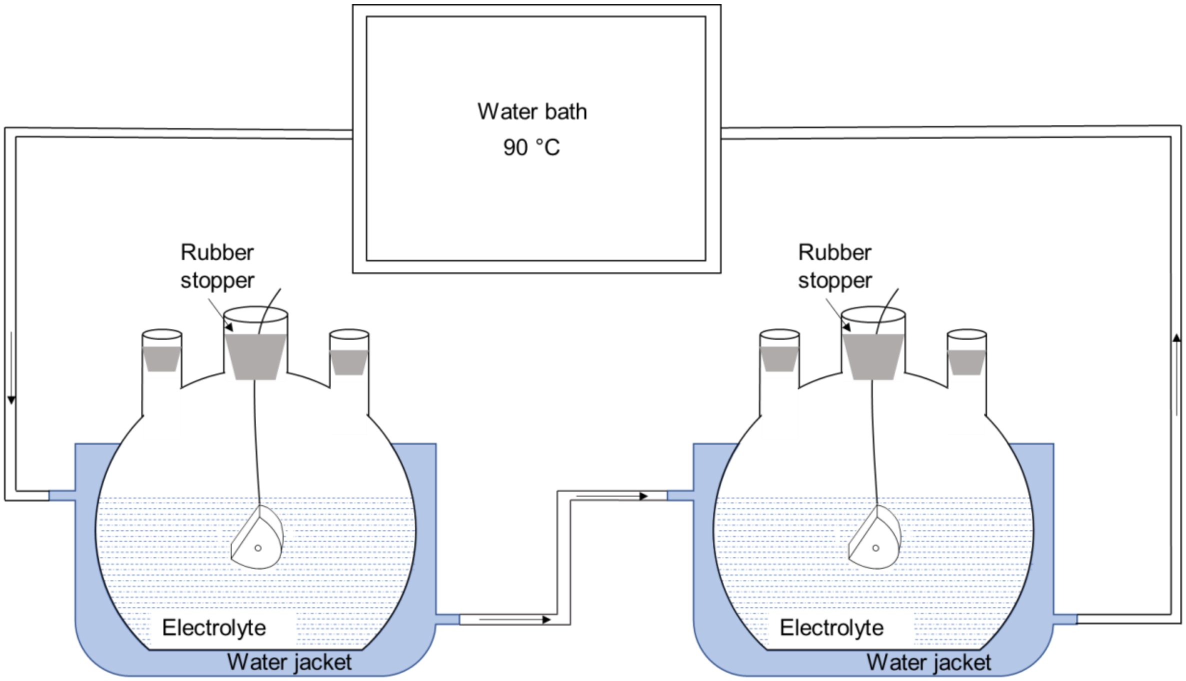

Figure 3.5. Schematic of immersion corrosion experimental setup.

The samples were prepared in the form of a truncated cylinder with a 1.55 mm diameter hole for mounting. The dimensions are shown in Figure 3.6. The edge area to total area ratio was maintained under 30 %. The samples were then grounded using SiC abrasive down to 600 grits. The tests were conducted in 4.46 wt. % KCl solution at 90 °C, which is a typical downhole environment. The ratio of test solution volume to specimen surface area was kept constant at 0.30 mL/mm^2 to avoid any appreciable changes that could cause further corrosion. Since the alloys are dissolvable, the tests were conducted for 1 hour immersion time. The mass of the specimens was measured before the test and after cleaning the corroded specimen using an analytical balance (Denver Instruments P-225D) with an accuracy of 0.00001 g. The corrosion products were cleaned using mechanical methods. The loosely attached corroded layer, if any, was scrubbed off the specimens before placing them in flasks filled with ethanol for ultrasonic cleaning. The samples were then scrubbed with Q-tips and an abrasive to remove the remaining corrosion products with minimum removal of sound metal. The corrosion rates (CR) of the specimens were calculated using the formula [102]

$$CR\ (g/m^2\ d)\ = K\frac{W}{A\,T\,D},$$

(3. 7)

where W is the mass loss in g, A is the surface area in m^2, T is the immersion time in days, D is the density of the specimen in g/m^3, and K is a constant for unit conversion. The value of K is 10,000 D to calculate the CR in the units mentioned in the equation above.

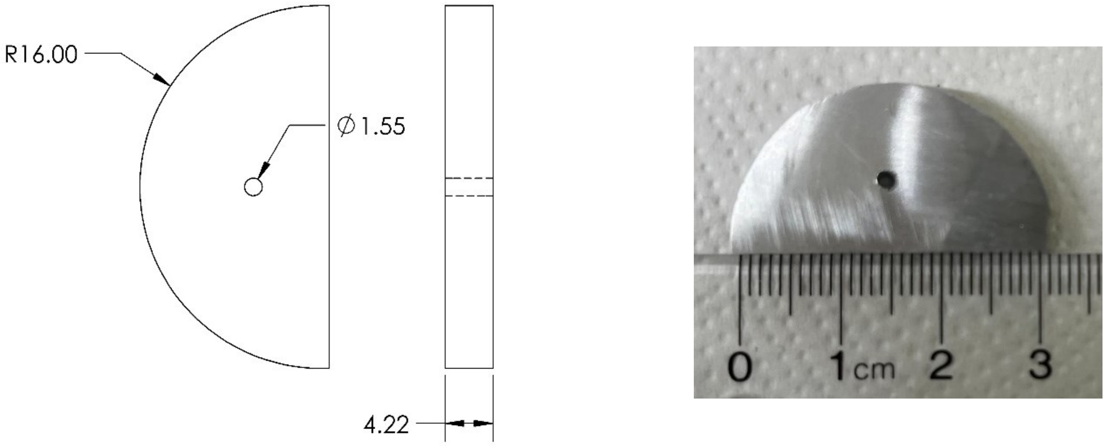

Figure 3.6. Dimensions of immersion samples.

3.6 Mechanical testing

Two methods were adopted to examine the mechanical performance of the DAs: micro-hardness testing and tensile testing. All the alloys were tested in as-cast condition at room temperature.

Tensile test specimens were machined to make sub-size rectangular samples as per ASTM B557M with a 6 mm width and a gauge length of 25 mm. The dimensions of the specimens are provided in Figure 3.7. Tensile testing was performed using 10,000 N Instron universal testing machine (UTS) at a pulling rate of 0.48 mm/min.

Vickers micro-hardness measurements were performed with Wilson VH3100 Hardness Tester. At least seven arbitrary indentations were taken. The load and dwell time used were 0.2 Kg and 10 seconds, respectively.

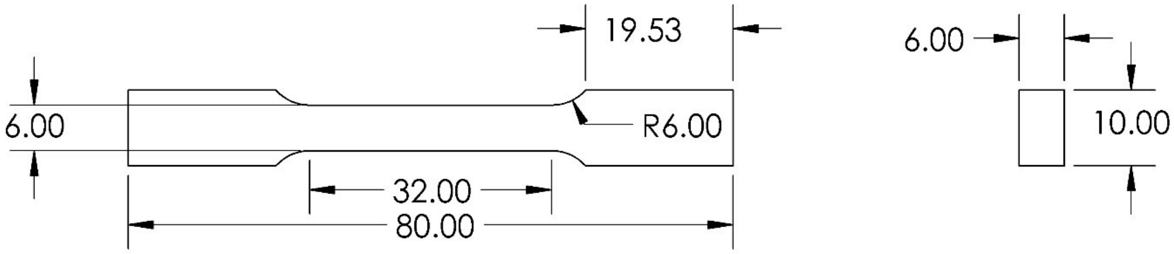

Figure 3.7. Tensile specimen dimensions as per ASTM B557M standards.

Chapter 4. Results and Discussion

Results and discussion of experiments and simulations performed in this study will be presented in this Chapter. Firstly, the effects of the associate cation type (K^+ vs. Na^+) on the corrosion of selected alloys were investigated by comparing the electrochemical values obtained under the same Cl^- molar concentration of KCl vs. NaCl solutions. The second part focused on predicting the phases in the Al-based DAs understudy. Based on the simulation results, the most promising DAs that are anticipated to yield a high corrosion rate and good mechanical strength were selected and cast. The microstructure characterization of the selected DAs will be analyzed, discussed, and compared to the simulation results. Subsequently, the corrosion and mechanical performance of the as-cast DAs will be evaluated and compared to commercial DA samples. A summary of the effects of the alloying elements will subsequently be discussed in the end.

4.1 The effect of associate cations (K+ vs. Na+) on the corrosion of selected alloys

As mentioned in the introduction chapter, the main chemistry in downhole environments is KCl while the abundant EC data of AAs is in NaCl electrolytes [10–12]. The corrosivity of these two electrolytes is believed to be mainly due to the anion Cl^-. Thus, to investigate the cation effects, EC experiments were performed at the same Cl^- concentration (0.59 M). Equilibrium OCP values of mechanically polished AA 2024, AA 6061, AA 7075, and Al-based DA electrodes in 0.59 M NaCl and 0.59 M KCl respectively reveal insignificant variance upon changing cation type for each alloy, as shown in Table 4.1. The highest relative difference of OCP obtained in KCl and NaCl electrolyte at the same Cl^- concentration was reported for AA 2024 with a value of 3.78% (*i.e.*, accepted value given a tolerance of 5%).

Table 4.1. OCP values of selected alloys in 0.59 M NaCl vs. KCl electrolytes at room temperature.

Alloy	Cation	OCP (mV vs Ag/AgCl)	Relative difference (%)
AA 2024	K+	-576	3.78
	Na+	-555	
AA 6061	K+	-710	0.70
	Na+	-705	
AA 7075	K+	-781	1.64
	Na+	-768	
Al-based DA	K+	-1,209	0.90
	Na+	-1,220	

Figure 4.1 presents a scatter plot of the corrosion potentials (E_{Corr}) and the corrosion current densities (i_{Corr}) obtained in 0.59 M NaCl and 0.59 M KCl electrolytes, respectively. The scatter plots allow for a direct comparison of E_{Corr} and i_{Corr} values for a given alloy in NaCl and KCl electrolytes. Hypothetically, all data points should lay on the regressed diagonal line to show a perfect match of the responses. As shown, the data points of E_{Corr} and i_{Corr} lay close to the diagonal line indicating a strong similarity in the responses, except for the corrosion current density of the Al-based DA. Even though the i_{Corr} values for the Al-based DA obtained in both electrolytes do not match perfectly, the relative difference is only 3.32%. Therefore, the drawn conclusion of the insignificant effects of cations on corrosion holds. The Al-based DA is sensitive to the environment since it was made to dissolve rapidly, thus small experimental errors could cause intensified effects on i_{Corr}.

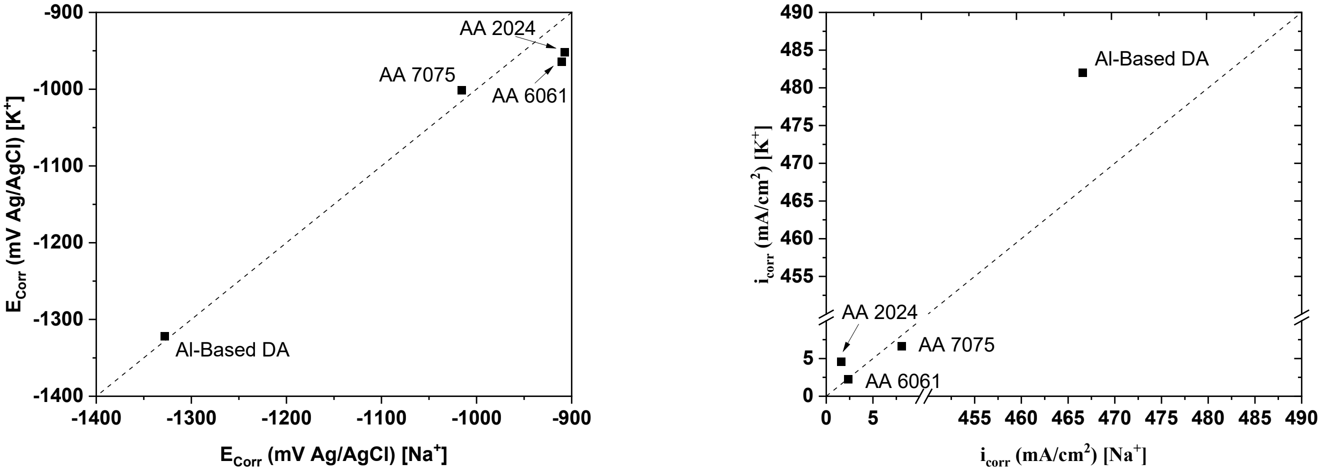

(a)

(b)

Figure 4.1. Scatter plots presenting the deviation of EC results obtained in 0.59 M KCl compared to 0.59 M NaCl for (a) corrosion potentials, E_{Corr}, and (b) corrosion densities, i_{Corr}.

Analysis of variance was conducted to compare the variance across the mean between the responses using MiniTab statistical software (version 20.3). The results assure the insignificance effect of changing cation type (Na$^+$ vs K$^+$), where the P-Values (0.981 and 0.889 for i_{Corr} and E_{Corr}, respectively) are greater than the level of significance ($\alpha = 0.05$). Thus, the null hypothesis of equal means $H_o: \mu_1 = \mu_2$ is not rejected. This can be explained by the similar ionic concentration of Cl$^-$ in both electrolytes.

The selected cations' impact on corrosion has also been reported in other studies [103, 104], where Na$^+$ and K$^+$ cations were reported to have relatively small effects on corrosion. Therefore, it is reasonable to conclude that metals behave the same in NaCl and KCl solutions of similar milliequivalents. In a word, to maximize the available EC data of AAs, the corrosion data of AAs in NaCl electrolytes can be considered at the review stage.

4.2 Prediction of intermetallic phases formed during solidification

As previously concluded in Chapter 3, the Taguchi method (L27) was implemented with 6 design factors at 3 levels. Table 3.2 summarizes the values for each respective design factor at each level, and Tables 3.3 and 3.4 list the chemical compositions of the designed alloys considered for phase simulation. Unfortunately, our current attempt failed to simulate the solidification process for DAs 16, 17, 19, and 26; further investigation is part of the ongoing research. Among all the other 23 DAs, Figures 4.2 and 4.3 (a-c) present the solidification paths of DAs 13, 18, 25, and 27; the individual SG solidification curves of the rest 19 alloys are included in Appendix A. The solidification paths for all the DAs were produced using TCAL7 (v.7.1) database through ThermoCalc software (2021b).

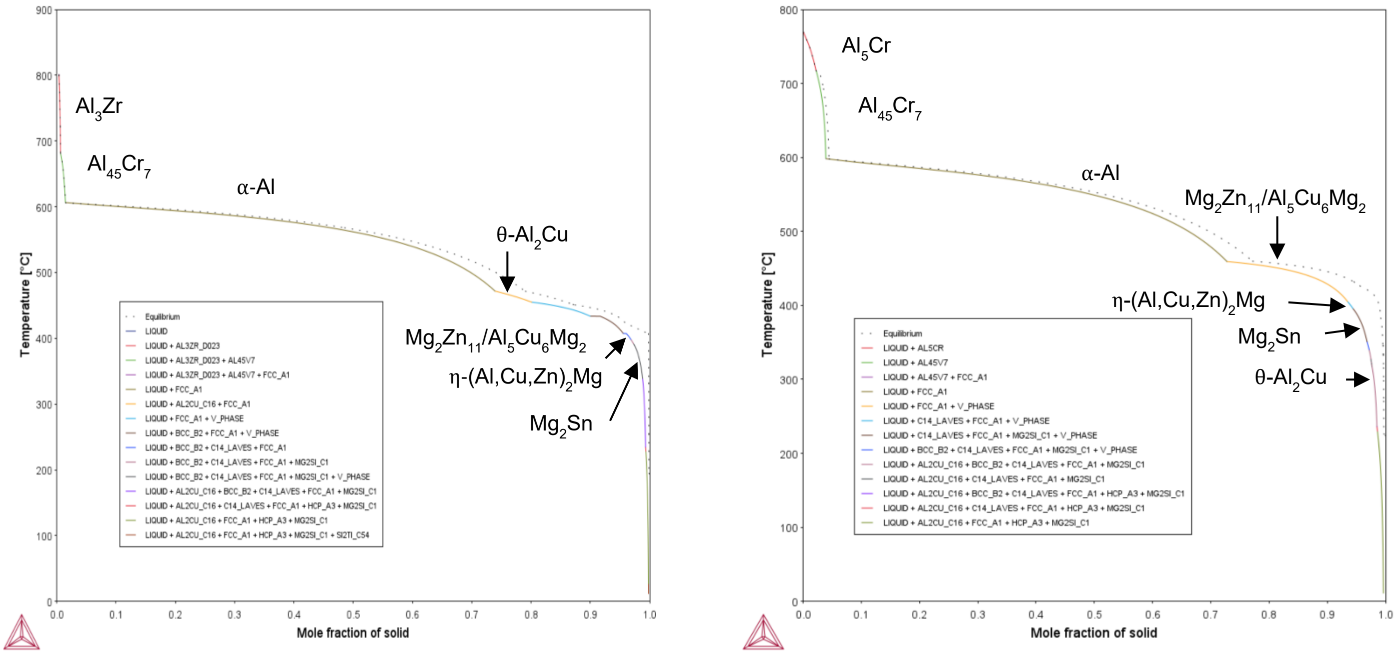

(a) (b)

Figure 4.2. SG solidification diagram for (a) DA13 and (b) DA18 (Thermo-Calc 2021b).

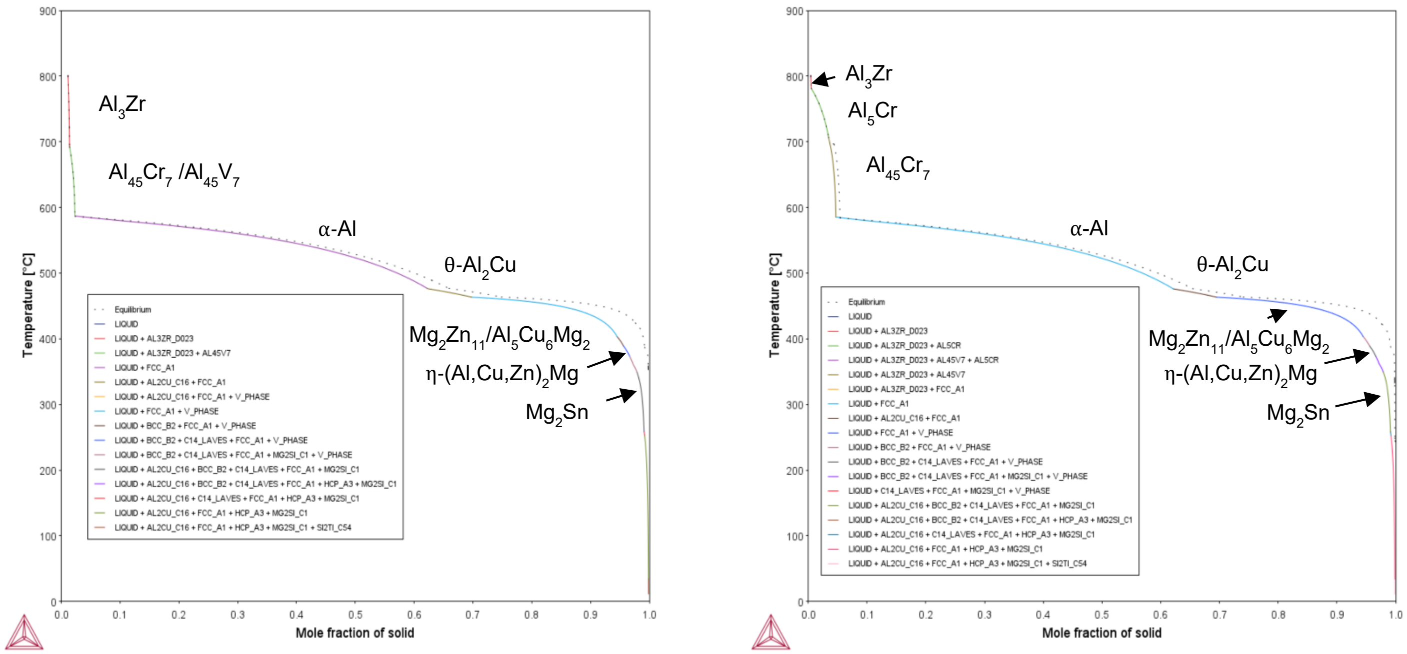

(c) (d)

Figure 4.3. Continued SG solidification diagram for (c) DA25 and (d) DA27 (Thermo-Calc 2021b).

Figure 4.4 shows the compositions of the main phases with respect to the 27 designed DAs predicted by the SG model. The primary phase in all the DAs is the α-Al. The SG model predicts secondary phases similar to those found in the 7xxx series of AAs, such as η−$MgZn_2$, S-Al_2CuMg, and θ−Al_2Cu. In addition, the Z phase (*i.e.*, Mg_2Zn_{11} or $Al_5Cu_6Mg_2$ [105]), Mg_2Sn, and BCC phase (*i.e.*, dispersed Ag) are also present. The fractions of the predicted phases vary depending on the initial alloys' compositions. It is reported that mechanical properties including strength, toughness, and SCC resistance are largely influenced by η, S, and θ-phases [106], while Mg_2Sn and BCC Ag have a nobler corrosion potential compared to pure Al [56]. In this work, more interest and attention are paid to the η and Z phases because they will not only lead to high corrosion activity of AAs but also contribute to mechanical properties enhancement [106].

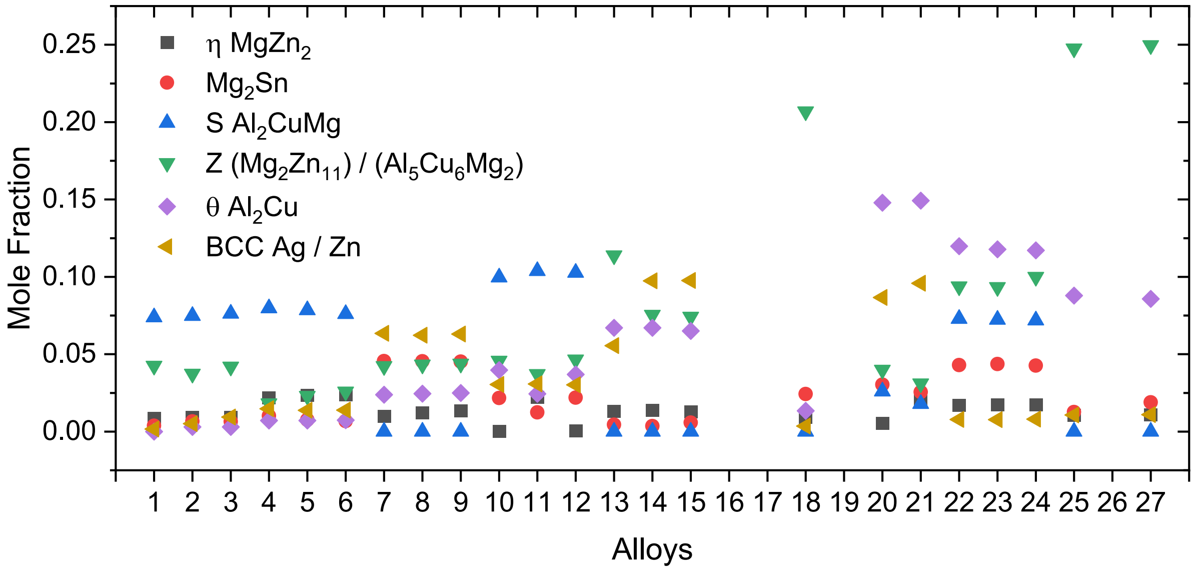

Figure 4.4. Mole fractions of phases in each alloy are predicted using TCAL7 database (Thermo-Calc 2021b).

While the mole fraction of η phase is relatively less than the Z phase, its fraction is high in DAs 4-5, 11, and 21-24. The Z phase fractions, on the other hand, are relatively high in DAs 13, 18, 25, and 27. Similarly, the θ-Al_2Cu phase mole fraction is at its highest in DAs 20-24, which should be excluded from the study as θ phase tends to negatively affect the dissolution rates of Al-based DAs by not only decreasing the contact area of GIS phases with Al matrix but also changing the chemistries at grain boundaries [60, 107]. Despite the implications the θ phase has on the dissolvability, its presence in AAs enhances the mechanical properties [108]. Examining DAs 13, 25, and 27, the fractions of θ and η phases are moderate relative to the other alloys while the Z phase is at its highest. In addition, DA 18 has a high amount of Z phase, a moderate and a low content of η and θ phases, respectively. It is suspected that a critical conclusion will be drawn on the influence of θ phase on corrosion and mechanical properties of AAs by comparing DA 18 with

DAs 25 and 27. The presence of coarse intermetallic phases in grain boundaries in as-cast alloys could potentially reduce the ductility. Embrittlement in AA 7075 due to coarse intermetallic phases has been reported in another study [106], which can be treated by homogenization. In addition, another concern is the liquid embrittlement caused by the presence of low melting point intermetallics.

Overall, it is expected that the alloys (DAs 13, 18, 25, and 27) will exhibit the desired corrosion rates and good mechanical performance that suits the application in downhole environments. The selection was based on the prediction results which revealed the phase fraction of Z phase, θ-Al_2Cu, and η and S phase, which are commonly found in AA 7xxx series. The next sections will discuss in detail the microstructure analysis as well as the DAs corrosion and mechanical performance.

4.3 Microstructure analysis of as-cast alloys

Four DAs out of the 27 alloys, DAs 13, 18, 25, and 27, are selected for casting and further investigation. This section presents and discusses the morphology of the as-cast DAs through SEM micrographs as well as the phase identification results from EDS and XRD.

4.3.1 X-ray diffraction analysis

After casting, XRD analyses were firstly carried out, and the results are shown in Figure 4.5. As shown, the main phases for all four alloys identified by XRD peaks are α-Al, η-$MgZn_2$, Mg_2Sn, and θ-Al_2Cu. The primary phase in all alloys is the α-Al matrix. According to the binary phase diagrams [69, 109] of Al-Ga, Al-Ag, Al-Mg, and Al-Zn, it is expected to see some of these elements in the α-Al matrix. In terms of secondary phases, all alloys contained η-$MgZn_2$ and Mg_2Sn phases. The Mg_2Sn XRD traces intensify for DA18 indicating the presence of the phase in higher amounts. In addition, the peaks of θ-Al_2Cu phase were only observed for DA25 and DA27 owing to the higher Cu:Mg ratio of these alloys. However, low melting point intermetallic phases such as In_3Sn and $InSn_4$ were not found in the alloys as well as Cr, Zr, and V-containing phases. Their absence in XRD patterns could be attributed to their low content in the experimental alloys. EDS analysis will be carried out to confirm XRD findings as well as to investigate the existence of the phase with low content.

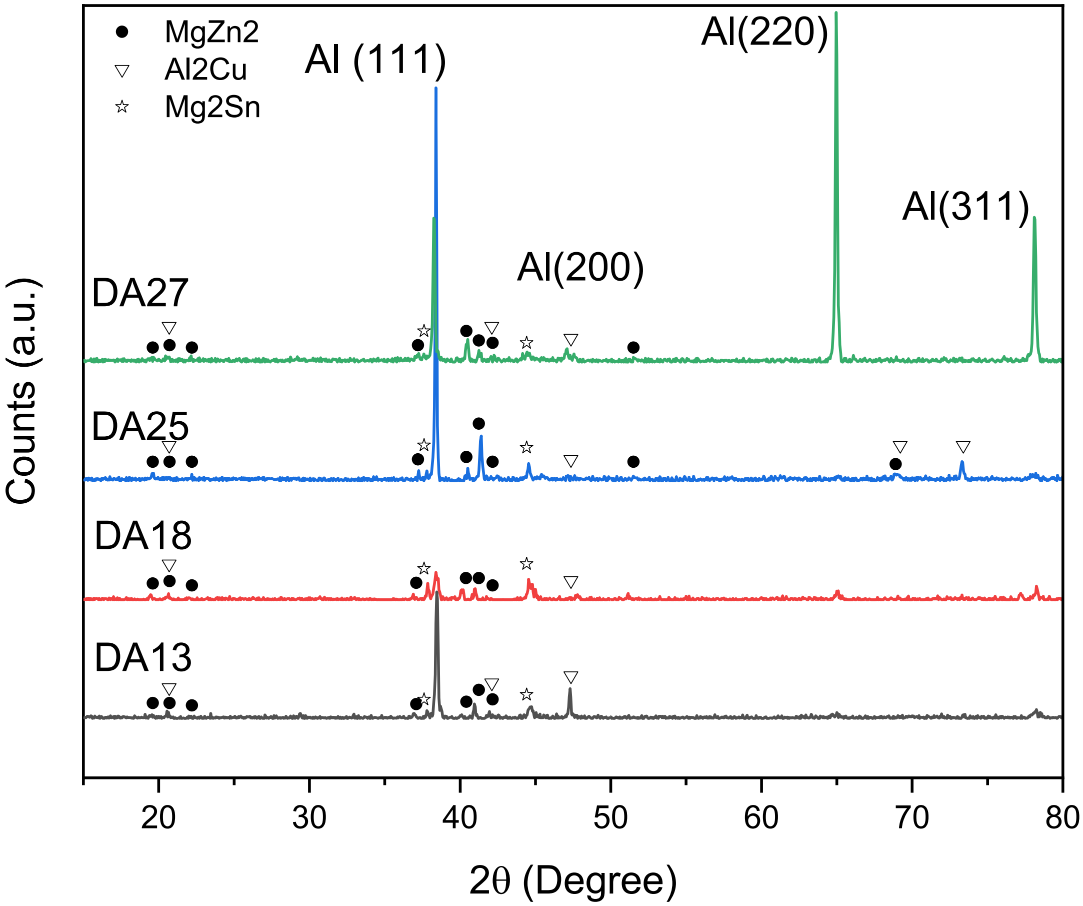

Figure 4.5. XRD patterns for the as-cast DAs.

4.3.2 SEM microstructures

The SEM back-scattered electron (BSE) images of the as-cast DA structures are shown in Figure 4.6 (a-d). The images reveal a dendritic microstructure of α-Al solid solution surrounded by segregated secondary phases. Intermetallic phases of different contrast are randomly distributed at grain boundaries. The measured grain sizes for the DAs using MLI are shown in Figure 4.7. The values range from 62.7 to 71.7 μm. The standard deviations of the MLI values are indicated by the error bars in the Figure. The grain sizes for DA25 and DA27 are similar having values of 62.7 and 63.4 μm, respectively. DA18 has the largest grain size compared to the other DAs with MLI value of 71.7 μm. The volume fractions of the dominant α-Al phase in all the DAs are measured using image analysis and listed in Table 4.2 The BSE images are utilized to determine phase fractions. The maximum relative difference between the experimental DAs and the simulation results is 2.34 % for DA25. More SEM images are provided in Appendix A.

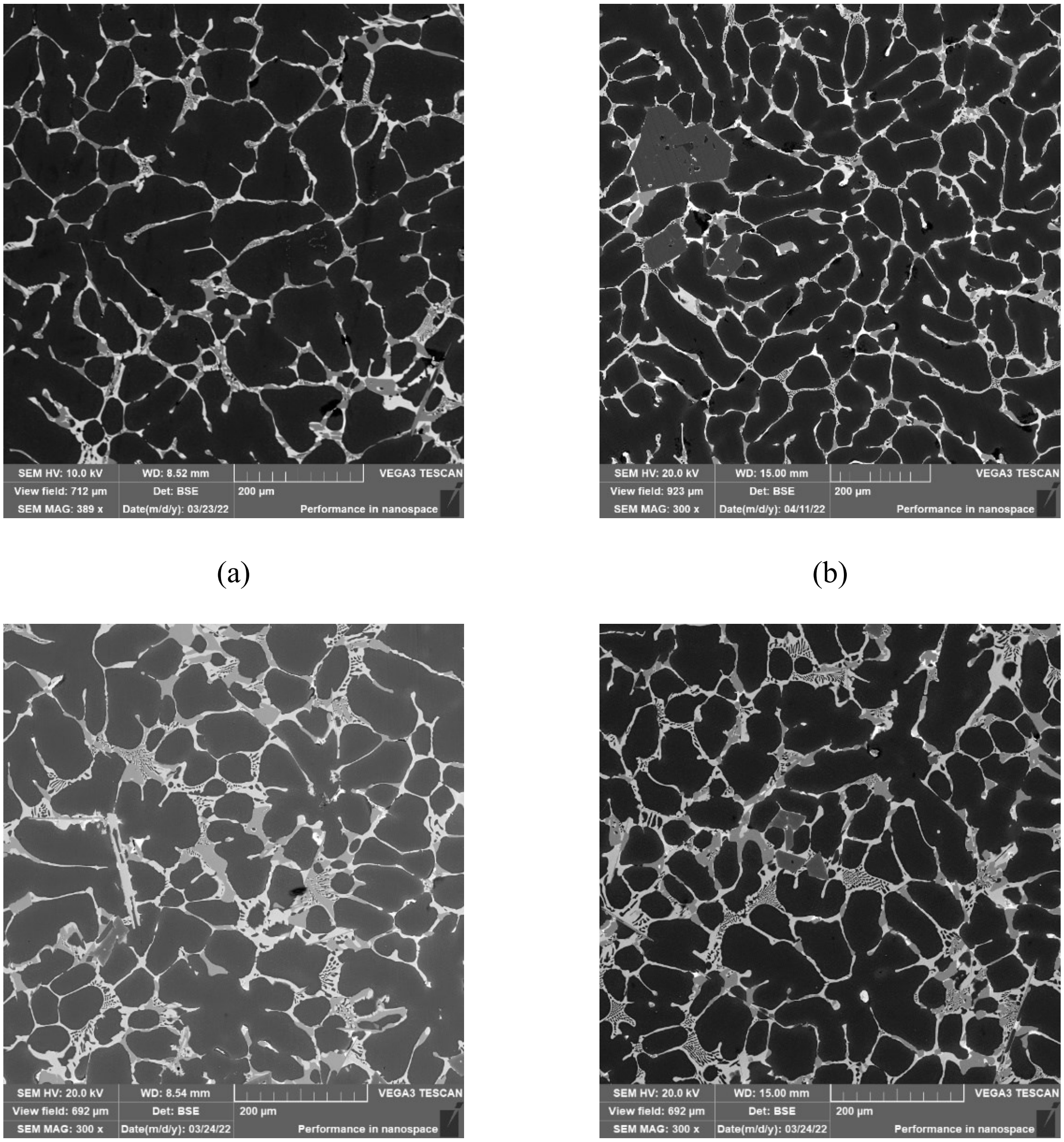

(a) (b)

(c) (d)

Figure 4.6. SEM BSE micrographs of the studied DAs. (a) DA13, (b) DA18, (c) DA25, and (d) DA27.

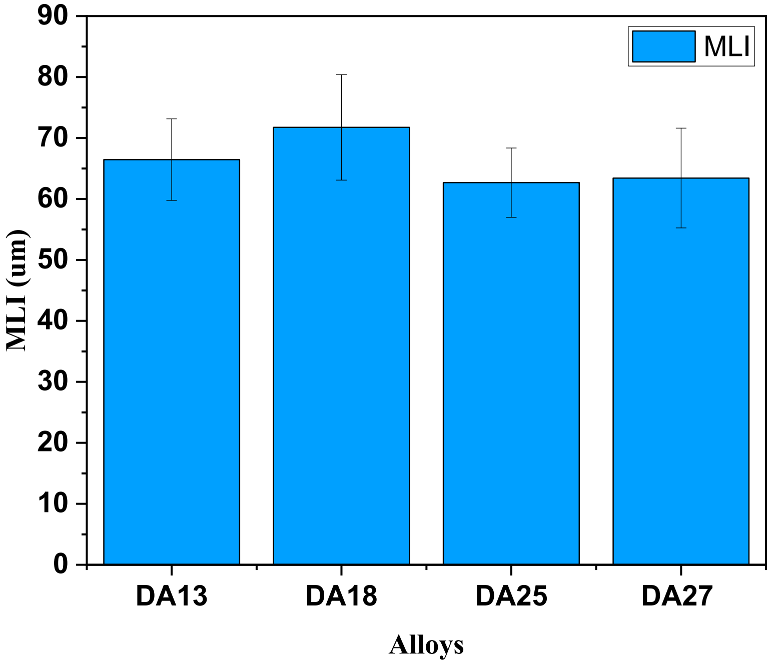

Figure 4.7. Grain size distribution for the studied DAs. (a) DA13, (b) DA18, (c) DA25, and (d) DA27.

Table 4.2. Comparison of phase fractions of α-Al phase in the selected DAs obtained from experiments and phase prediction.

Alloys	Amount of Al phase (vol. %)	
	Image analysis	SG model
DA13	84.55 ± 1.24	84.63
DA18	80.37 ± 0.21	82.00
DA25	76.46 ± 0.90	78.29
DA27	75.78 ± 0.65	75.82

EDS analysis revealed the compositions of Al grains and intermetallic phases, and the results are listed in Tables 4.3 and 4.4. Al grains of all the DAs contain small amounts of Zn, Mg, Cu, Ag, and Ga owing to their solubilities based on their respective binary phase diagrams, as was also reported in other studies [53, 110]. The compositions of light grey contrast (marked A in Figures 4.8(a) and (b)) of the eutectic-like network were revealed to be the η-$MgZn_2$ phase. The compositional results of this dominant second phase show that Cu, Ag, and Ga dissolved in the η phase substitute for Zn in the phase structure [111–113]. That is, (Cu + Zn + Ag + Ga) at. % accounts for the Zn at. % in the $MgZn_2$ phase. The association of Cu, Ag, and Ga in η-$MgZn_2$ phase is further examined in Figure 4.9. The line-scan clearly shows the depletion of Al in η phase, and the Al concentration drops in the grain boundary. EDS maps in Figure 4.10 (as well as in Appendix A) also confirm the absence of Al in η phase. Besides, the XRD peaks of a T phase were not found excluding the possibility of this phase being a ternary T phase in the constituent Al-Zn-Mg, which was reported to be a divorced phase in other studies [112, 114].

Table 4.3. Chemical compositions (at. %) of formed phases present in as-cast DAs.

Alloy	Phases	Al	Zn	Cu	Mg	Ag	Ga	In	Sn	Si	Ti	Fe	Cr	Zr	V
DA13	α-Al	94.73	2.59	0.96	0.96	0.41	0.17						0.18		
	θ-Al_2Cu	68.43	1.00	30.58											
	Mg_2Sn	6.00	1.11	0.56	61.15				28.00	3.18					
	In_3Sn	12.40	2.66	1.62			1.45	77.30	4.57						
	η−$MgZn_2$	19.35	21.55	9.21	32.94	15.48	1.47								
	Al_7Cu_2Fe	54.95	9.97	14.77	9.13	4.55	1.20					5.43			
	Al-In	49.05	2.19	0.64			1.09	46.02	1.01						
DA18	α-Al	94.33	2.89	1.05	0.92	0.17	0.47						0.17		
	θ-Al_2Cu	67.25	1.46	31.29											
	Mg_2Sn		1.24	0.58	64.59				31.41	2.18					
	In_3Sn	19.60	11.33	5.03	2.87	1.35	2.11	52.81	4.91						
	η−$MgZn_2$	21.33	23.12	17.73	33.50	2.70	1.62								
	Al_7Cu_2Fe	83.66	2.08	1.06							0.31	0.48	12.40		
	Al-In	41.25	2.78	6.94			0.82	43.55	4.66						

Table 4.4. Continued - chemical compositions (at. %) of formed phases present in as-cast DAs.

Alloy	Phases	Al	Zn	Cu	Mg	Ag	Ga	In	Sn	Si	Ti	Fe	Cr	Zr	V
DA25	α-Al	94.08	3.07	0.91	1.38	0.18	0.25						0.15		
	θ-Al_2Cu	67.11	1.29	31.60											
	Mg_2Sn		1.17	0.67	64.59				29.29	4.28					
	η−$MgZn_2$	21.88	23.86	15.84	32.66	4.48	1.28								
	Al-In	43.68	5.80	2.25			1.28	46.41				0.58			
	$Al_{45}V_7$	77.34	3.12	0.83	9.59	0.43					0.16		1.54		6.99
	Al_3Zr	74.32	1.28	0.48							0.46			23.47	
	Al_7Cu_2Fe	67.05	6.37	18.58		0.37	0.36					7.27			
DA27	α-Al	93.77	3.31	0.89	1.56	0.16	0.32								
	θ-Al_2Cu	67.28	1.14	31.58											
	Mg_2Sn		1.00	0.87	64.70				25.02	8.40					
	η−$MgZn_2$	20.54	23.88	16.73	33.53	4.12	1.20								
	$Al_{45}Cr_7$	72.95	4.57	1.83	11.01	0.75					0.41		8.34		0.13

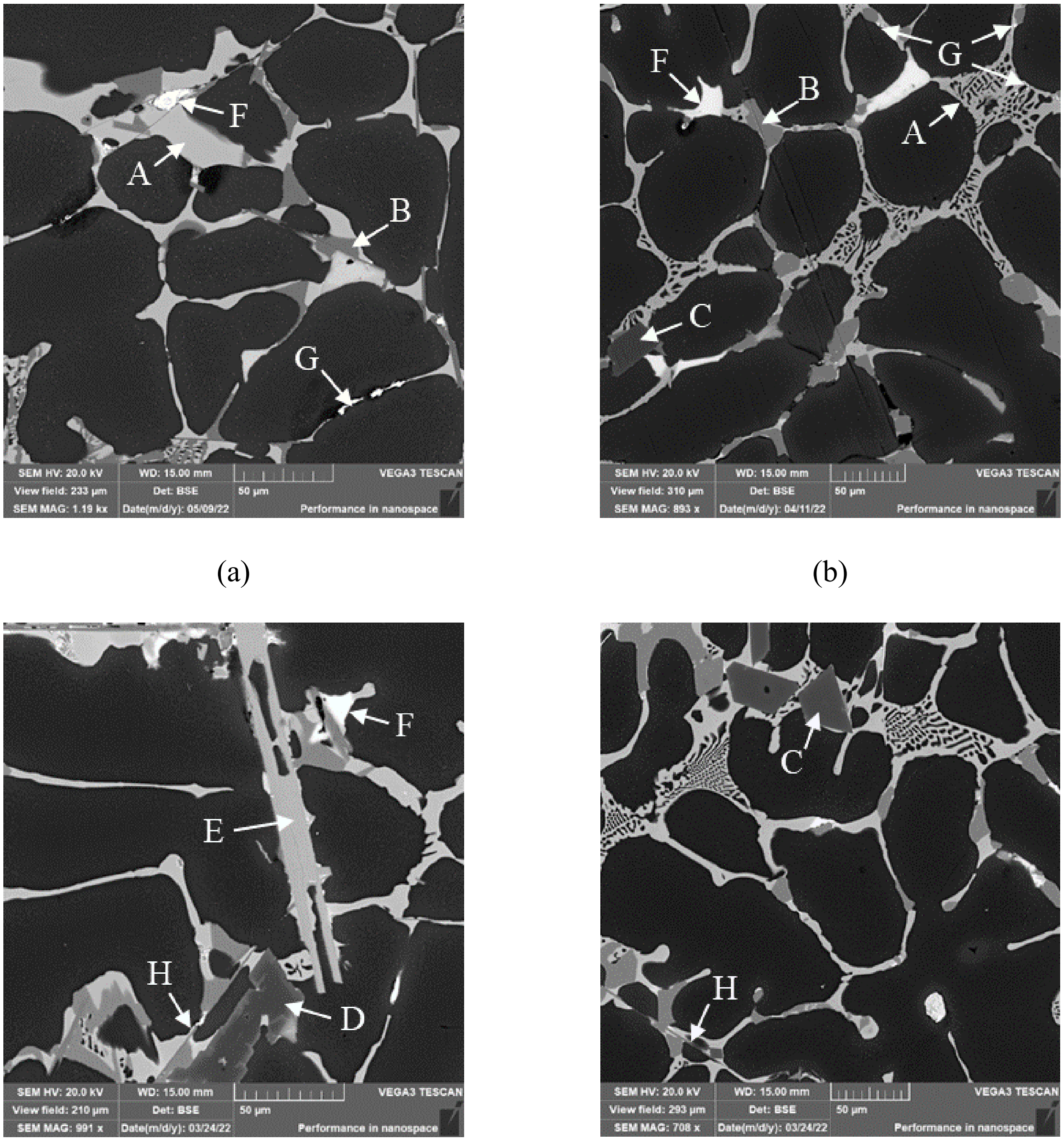

(a) (b)

(c) (d)

Figure 4.8. Low magnification of as-cast microstructure of (a) DA13, (b) DA18, (c) DA25, (d) DA27.

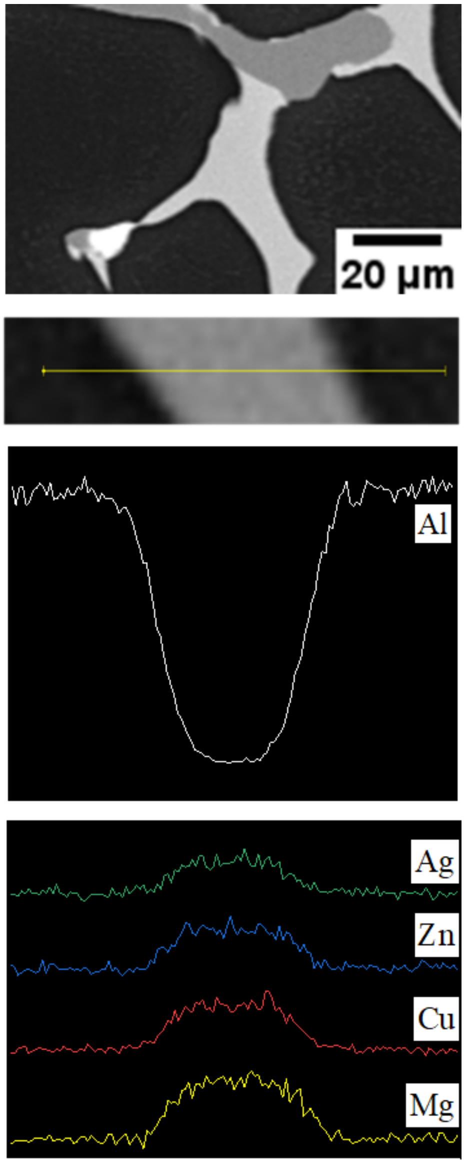

Figure 4.9. BSE image and line-scan traces of as-cast DA13 showing the association of Cu, Mg, Ag, and Zn in η-$MgZn_2$.

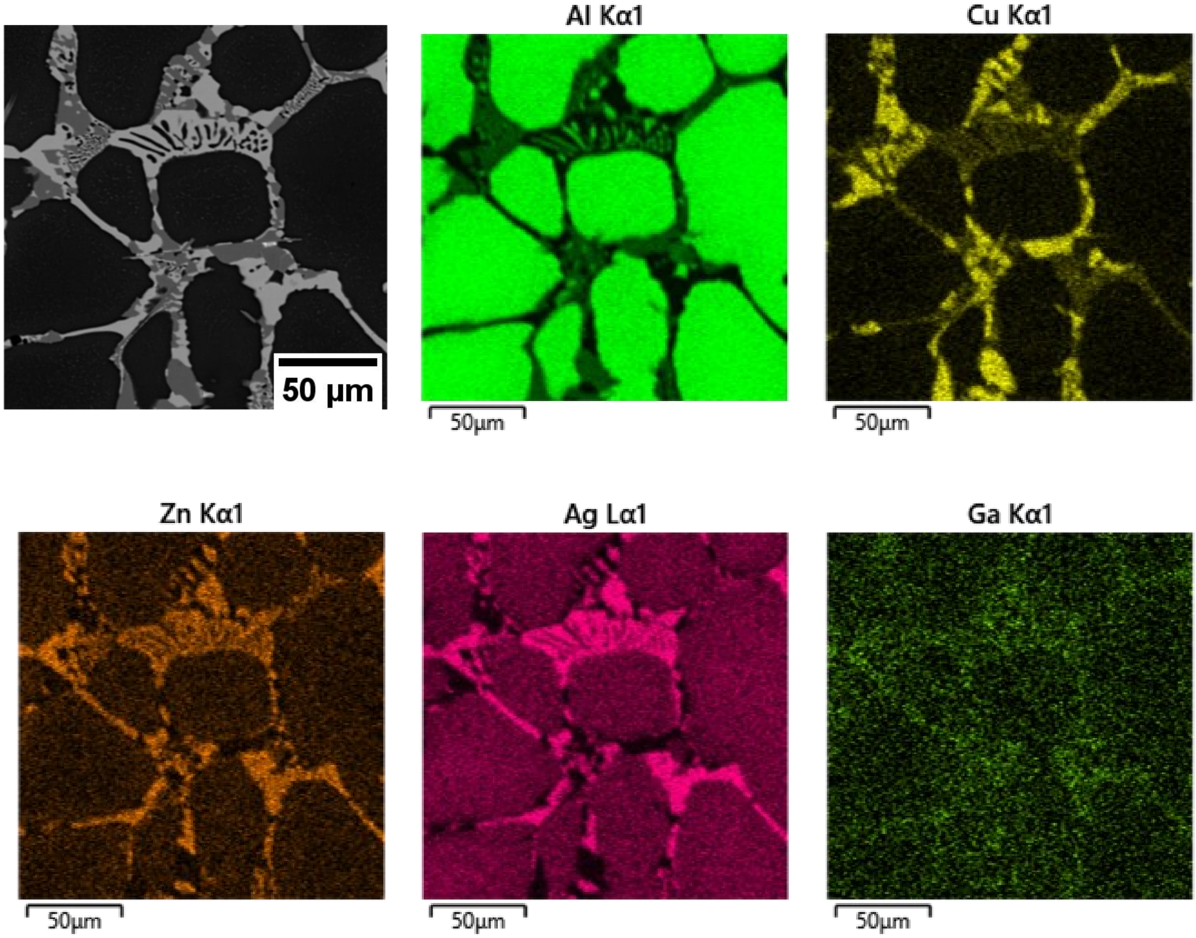

Figure 4.10. EDS maps of as-cast DA13.

Some other phases were mostly found inlaid in η phase. Similar findings were reported by Yanxia Li et al (2005) [114]. The compositions of the grey intermetallic phases distributed randomly in grain boundaries (labeled B in Figure 4.8(a) and (b)) are close to θ-Al_2Cu, which agrees with similar findings [60, 106, 113]. The darker grey contrasts (labeled C in Figure 4.8(b) and (d)) were identified as $Al_{45}Cr_7$. The rod-like V-rich and Zr-rich intermetallic phases (labeled D and E, respectively, in Figure 4.8(c) were only observed in DA25. This could be explained by their small phase fraction. Based on their stoichiometry, these phases can be described as $Al_{45}V_7$ and Al_3Zr, respectively. Furthermore, the bright contrast in all DAs corresponds to the low melting intermetallic phases: Mg_2Sn and In-containing phases (labeled F and G, respectively, in Figures 4.8(a-c)). While XRD traces show Mg_2Sn peaks, it fails to detect the In-containing phases' spectrums due to their small fraction. EDS results reveal that two types of In-containing phases were formed out of which one was associated with Al, and the other was close in the stichometry of In_3Sn phase. However, In_3Sn phase was only observed in DA13 and DA18. The formation of Al-In phase in Al-Cu-Mg-Sn-Ga-In alloys was reported in the literature [107]. Similarly, the needle-like Fe-rich phase (labeled H in Figure 4.8(c) and (d)) was only identified by EDS, and its stichometry was found to be close to Al_7Cu_2Fe. The formation of Fe-rich phase, commonly found in 7xxx series alloys, is consistent with the present literature [113, 115, 116].

4.3.3 Solution heat treatment

A segment of φ 33 × 5 mm cross-sectional samples were machined from the as-cast ingots for solution heat treatment investigations. The objective of heat treating is to homogenize the as-cast alloys and improve their mechanical properties. The homogenization heat treatment was carried out at 500 °C for 1 and 6 hours, respectively, then quenched in water.

Most AAs are homogenized after casting to obtain a uniform microstructure and remove the dendritic segregation as well as enable the dissolution of coarse phases back into the matrix [117–119]. Homogenization heat treatment attempts were also performed in this study to improve the performance of the DAs. At first, homogenization heat treating was performed at 500 °C for 6 hours referring to a previous study on Al-Mg-Ga-In-Sn alloy [23]. However, since the alloys under study contain low intermetallic phases and were meant to be dissolvable, heat-treating the alloys at elevated temperatures affected the alloys inversely. Figure 4.11(a-d) shows the state of the samples after heat treatment at 500 °C for 6 hours. As shown, a thick oxide layer was formed on the surface of all DAs and propagated into the center of the samples, as clearly seen in Figures 4.11(c) and (d). It is worth mentioning that DA25 and DA27 samples were easy to break by hand. Similar results were obtained even after reducing the time of treatment as shown in Figure 4.12 (a-d) illustrates the states of the DAs after homogenization at 500 °C for 1 hour.

Visiting the solidification curves in Figure 4.2 and Figure 4.3 (a-c) reveals the presence of a liquid phase at temperatures approximately above 200 °C for all the DAs as the mole fraction of the solid phase is still less than 1.0. Therefore, it is concluded that it is not practical to homogenize the DAs at elevated temperatures (as is the case for Al-Zn-Mg-Cu alloys), and further studies will be performed on the as-cast DAs.

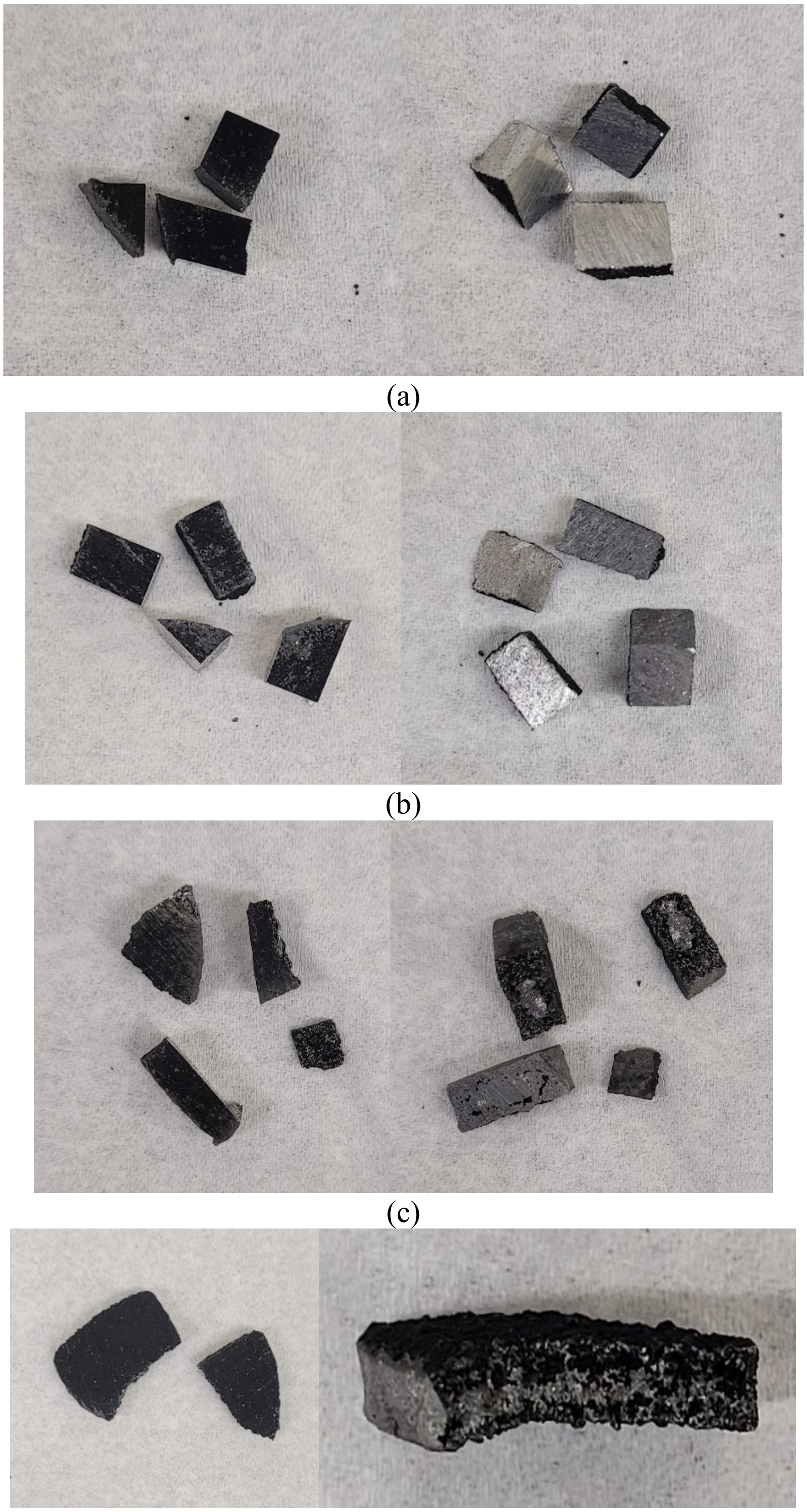

(a)

(b)

(c)

(d)

Figure 4.11. Presentation of samples state after solution heat treating at 500 °C for 6 hours (a) DA13, (b) DA18, (c) DA25, and (d) DA27.

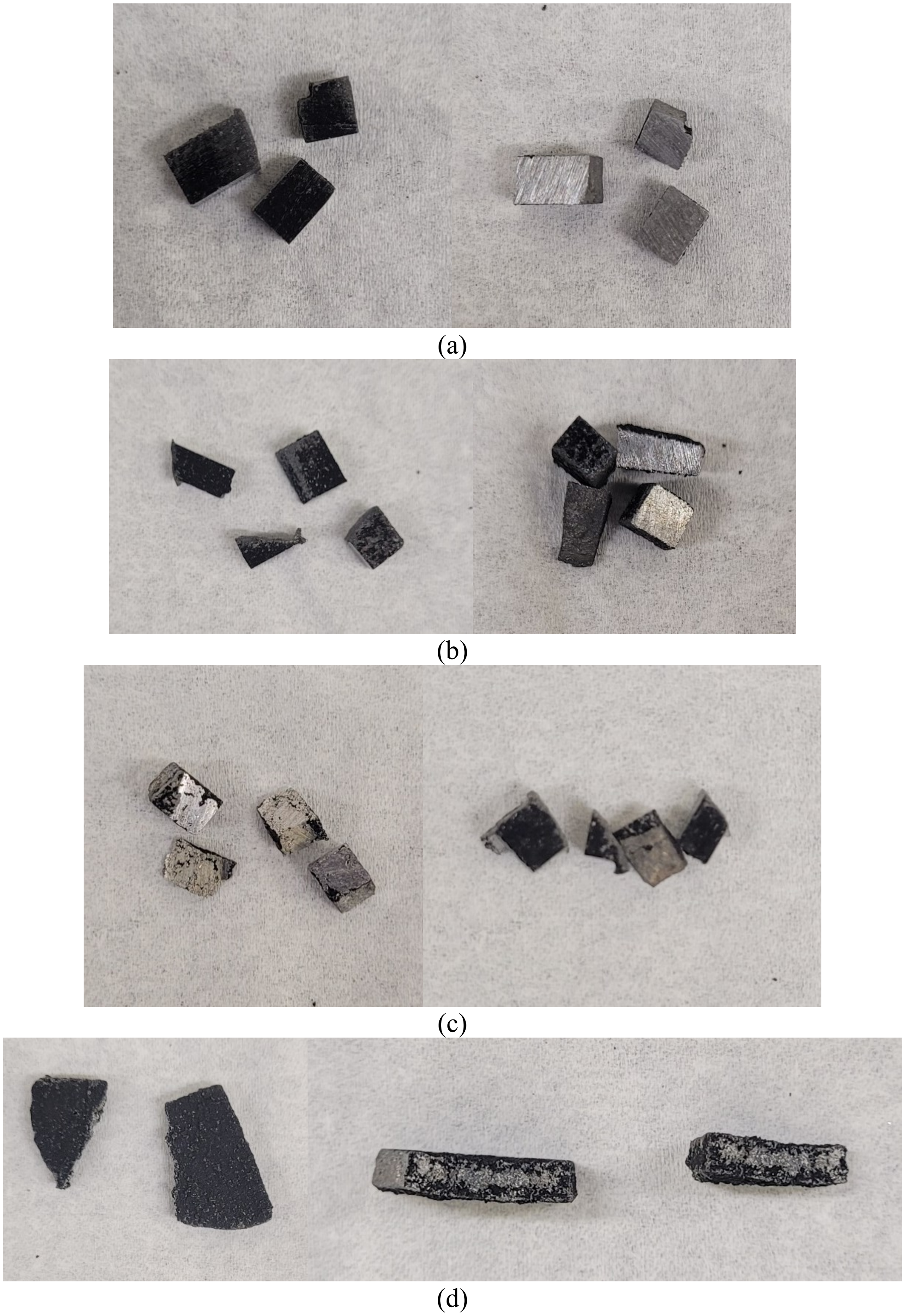
(a)

(b)

(c)

(d)

Figure 4.12. Presentation of samples state after solution heat treating at 500 °C for 1 hour (a) DA13, (b) DA18, (c) DA25, and (d) DA27.

4.4 Immersion corrosion experiments

Initially, attempts to perform OCP and LPR tests were carried out on the four DAs at 90 °C. Figure 4.13 (a) and (b) show the OCP curves for all the DAs. Interestingly, DA18 and DA25 dissolved completely in the solution. The time at which the distortion on the surface occurred can be traced by analyzing the OCP curve in Figure 4.13(a). As marked in Figure 4.13(a), the samples degraded intensively and distortions occurred after 66.7 and 94.2 minutes for DA18 and DA25, respectively. The state of the samples as well as the corrosion products are also shown in Figures 4.14(a) and (b). Examining the intensity of corrosion, DA18 seemed to have higher corrosion rates compared to DA25. On the other hand, the OCP curves for DA13 and DA27 did not indicate any distortions, and tests were performed normally. This in turn indicates the low corrosion rates compared to DA18 and DA25. In addition, the OCP curve in Figure 4.13(b) reveals that the equilibrium corrosion potential was not reached for both DA13 and DA27. The corrosion potential increased steadily with time for the 6 hours of testing. It was concluded that the determination of corrosion rates from EC experiments was not appropriate. Therefore, immersion corrosion tests were conducted to measure real-time corrosion rates for all the DAs.

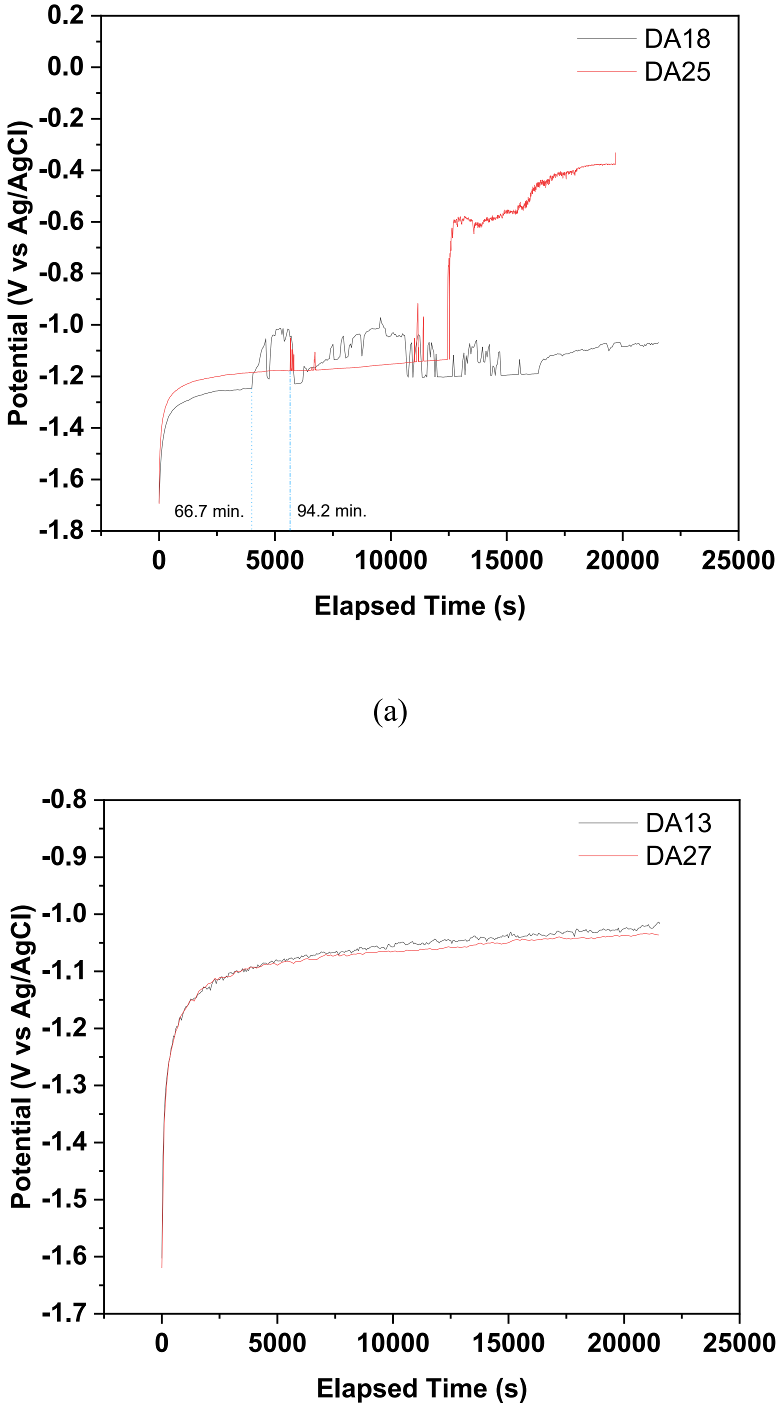

(a)

(b)

Figure 4.13. OCP curves at 90 °C in 0.59 M KCl solution for (a) DA18 and DA25, and (b) DA13 and DA27.

(a) (b)

Figure 4.14. Corroded samples in 0.59 M KCl at 90 °C: (a) Complete dissolution of DA18 (sample dropped off the mold) and (b) Sever corrosion of DA25 sample showing part of the samples dropped off the surface.

The degradation of the DAs was further investigated via immersion corrosion tests in 0.59 M KCl solutions. The corrosion tests were performed at 90 °C and the corrosion rates are presented in Figure 4.15 for the as-cast and reference DAs. As previously discussed, the activation of designed DAs' corrosion is largely dependent on the content of GIS. DA18 with 3 wt. % GIS content shows the highest corrosion rate of 177.76 mg/cm^2 h. For all the other alloys, when GIS was held constant at 1.5 wt. %, the corrosion rates significantly dropped to 0.65, 3.97, and 4.93 mg/cm^2 h for DA13, DA25, and DA27, respectively. The trend can be explained by the effective reaction sites. The higher corrosion rates were observed owing to the disruption of the Al oxide layer caused by the liquid phases. The presence of the low melting point phases increased the reaction sites of Al and water [16, 23, 54, 72]. It is also shown in Figure 4.15 that DA18 outperforms the reference Mg-based and Al-based DAs by 115.56 and 142.97 mg/cm^2 h, respectively. However, this comes at a cost of the mechanical properties as will be discussed in the next section.

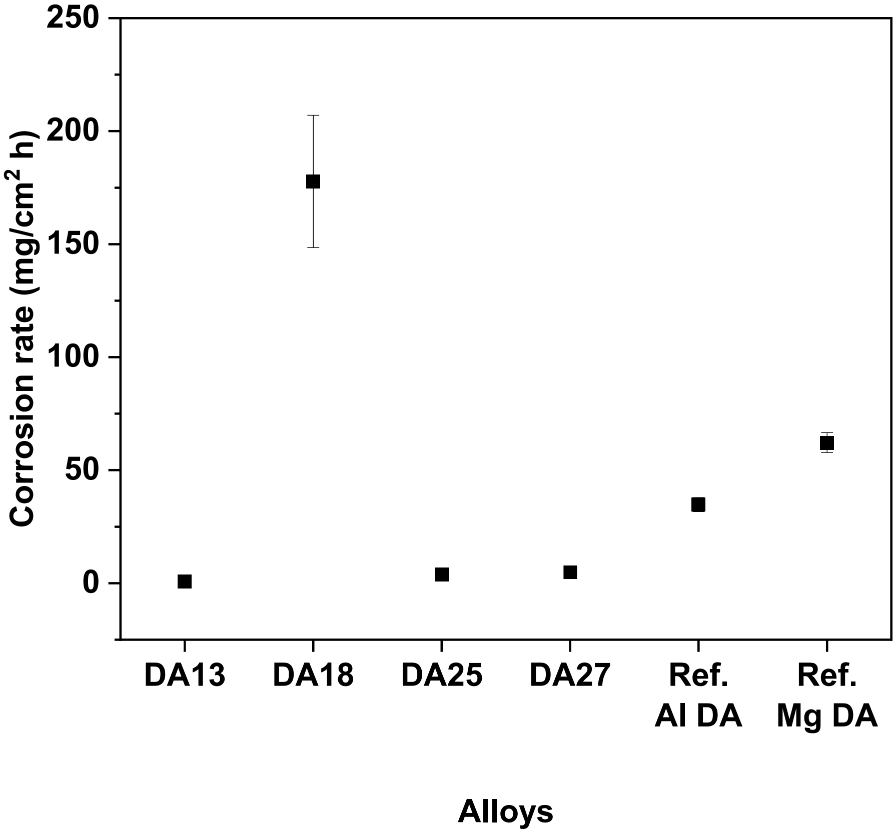

Figure 4.15. Immersion corrosion rates of the as-cast DAs and reference Al-based and Mg-based DAs.

The mechanism by which the high corrosion rate is achieved relates to the presence of the low melting intermetallic phase in the alloy. Woodall proposed that Al reacted with water through a liquid GIS phase acting as an inert [40, 52]. At first, the Al particles in the liquid phase react with water inducing a concentration gradient and a driving force for other Al particles to diffuse into the reaction sites. Similar results were obtained in Al-Cu-Mg-Ga-Sn-In alloys, where the inert phase was the Al-In eutectic [107]. The Al oxide layer is weakened by the presence of Cl^- which causes pitting, and also by the presence of GIS phases which act as gateways for Al hydrolysis reactions. It was suggested that the hydrolysis reaction of Al occurs on the same basis. The DAs understudy contain, in varying amounts, In-containing phases besides the Mg_2Sn phase that acts as a cathode to the Al matrix. Figure 4.16 shows the EDS maps showing the distribution of Ga, In, and Sn elements. The phase fractions and distribution of In-containing phases appear to be high for DA18 explaining its fast dissolvability. Besides, the presence of Ga in the Al matrix disturbs the oxide layer and gives a gateway for a continuous hydrolysis reaction of metal [120, 121].

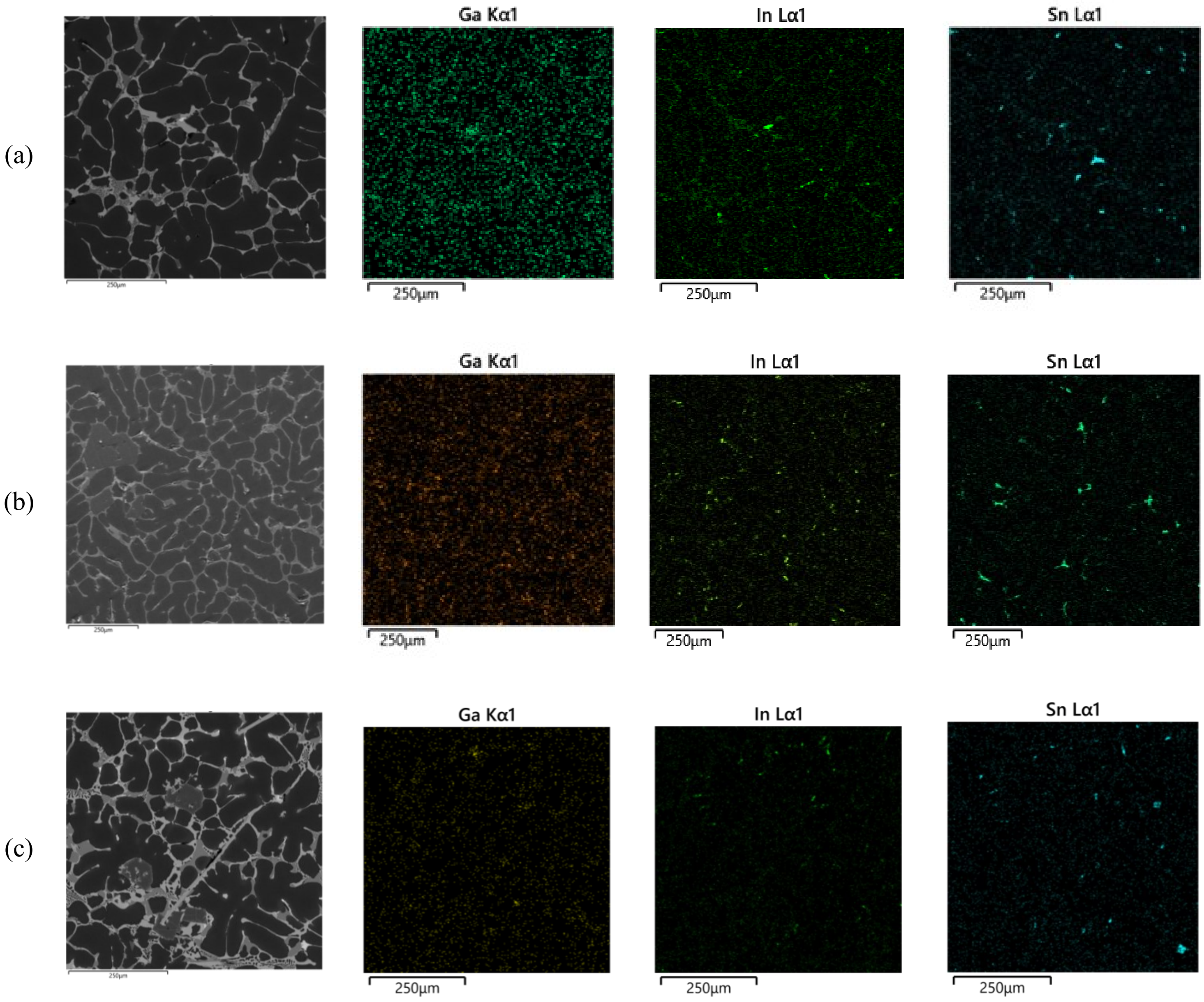

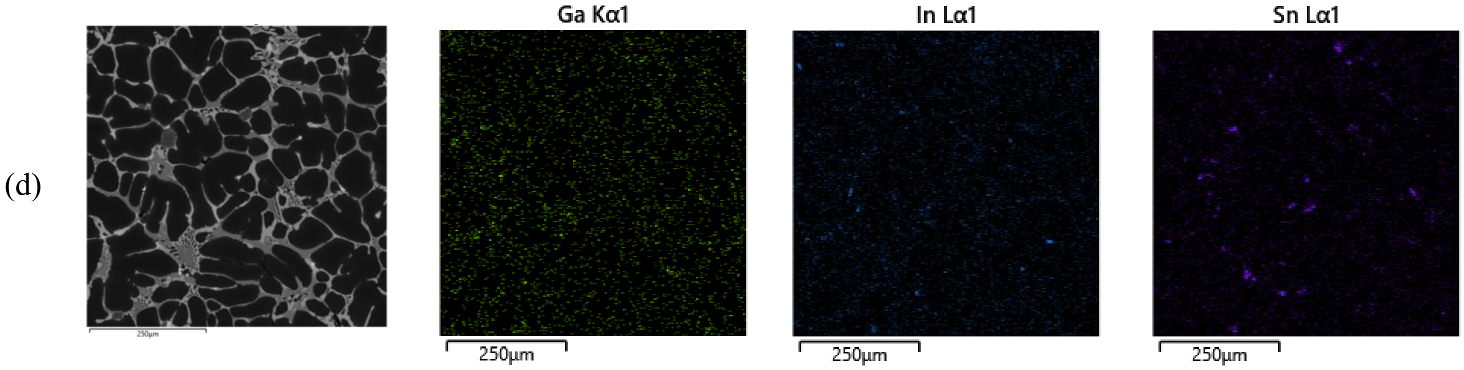

Figure 4.16. EDS maps showing the distribution of the low melting point elements (GIS) (a) DA13, (b) DA18, (c) DA25, and (d) DA27.

Figure 4.17 and 4.18 show the SEM images of the as-cast DA13 and DA18 after immersion in KCl solutions at 90 °C. Figure 4.17(a) and (b) show the surface of DA13 and DA18, respectively, after 20 seconds of immersion. Figure 4.18(a) and (b) present the surface state after immersion for 60 seconds for both DAs, in the same order as above. It was observed that two corrosion mechanisms occur simultaneously. The corrosion was initiated at the junction of Al with the second phase (η-$MgZn_2$, labeled C in Figure 4.17). Comparing DA13 with DA18 after 60 seconds of immersion, the localized IGC seemed more severe in DA18 than in DA13. This could be explained by the higher content of Ag in the DA13 in grains and grain boundaries as seen in Table 4.3. The content of Ag in the solid solution alters the potential difference between the η phase and Al matrix. In addition, Ag content in the η phase makes it more resistant to localized corrosion. Similar findings were reported by Wang et al (2020) for the influence of Ag on pitting corrosion of the θ-Al_2Cu phase [122]. Furthermore, significant uniform corrosion attacks were also observed adjacent to the In-containing phase (labeled A in Figure 4.17). As GIS content is higher in DA18, larger corrosion areas were observed compared to DA13.

Besides localized corrosion, another key factor for the fast dissolution of DA18 is the presence of Ga in the solid solution of the Al matrix. For DA13, corrosion pits were observed after 60 seconds' immersion owing to the Al oxide dissolution caused by Cl^- penetration. Those pits were not observed in Figure 4.17(a). Unlike DA13, corrosion pits on DA18 were pronounced in the Al matrix (*i.e.*, on areas not adjacent to the second phases) even after 20 seconds of immersion. Ga acts as an inert phase to facilitate the reaction of Al with water and disturbs the Al oxide film [31, 121]. Therefore, Ga content is crucial for the dissolvability of Al.

DA18 has less content of Ag compared to the other DAs, therefore the influence Ag has on localized corrosion is expected to be minimized as well (i.e., Ag present in the matrix will not adjust its activity relative to the grain boundaries since the alloy has only 0.7 wt.% Ag). Further, DA18 has double the GIS compositions (3 wt.% for DA18) compared to the other alloys. Considering the corrosion mechanism, it is evident that the dissolvability of DA18 is resulting from the combined effects of localized corrosion and Al oxide depassivation. Yet, the fast dissolution trades off with the mechanical properties which will be discussed next.

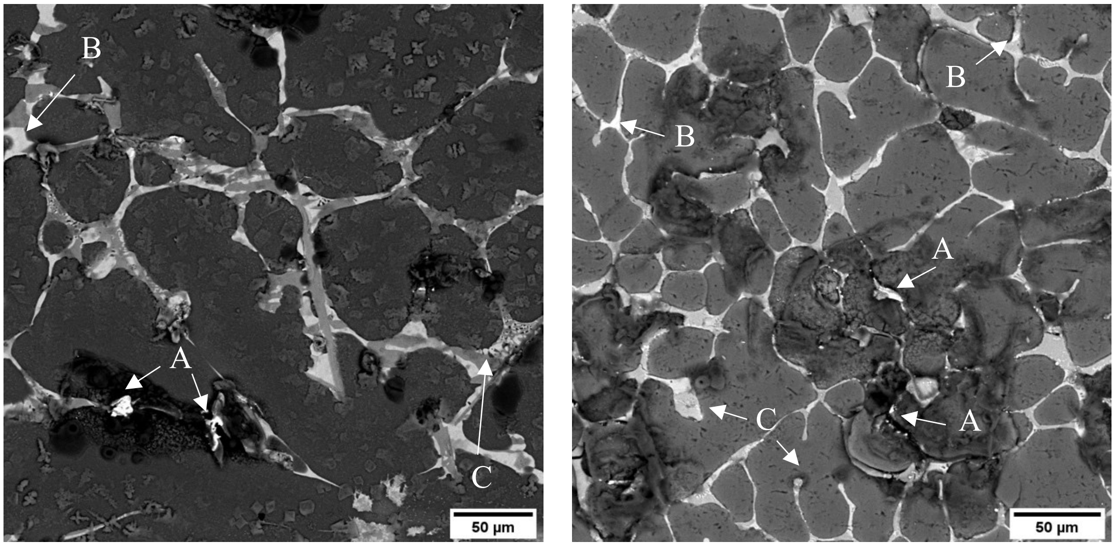

(a) (b)

Figure 4.17 SEM images of as-cast DAs in 0.59 M KCl at 90°C after 20 seconds. (a) DA13 and (b) DA18.

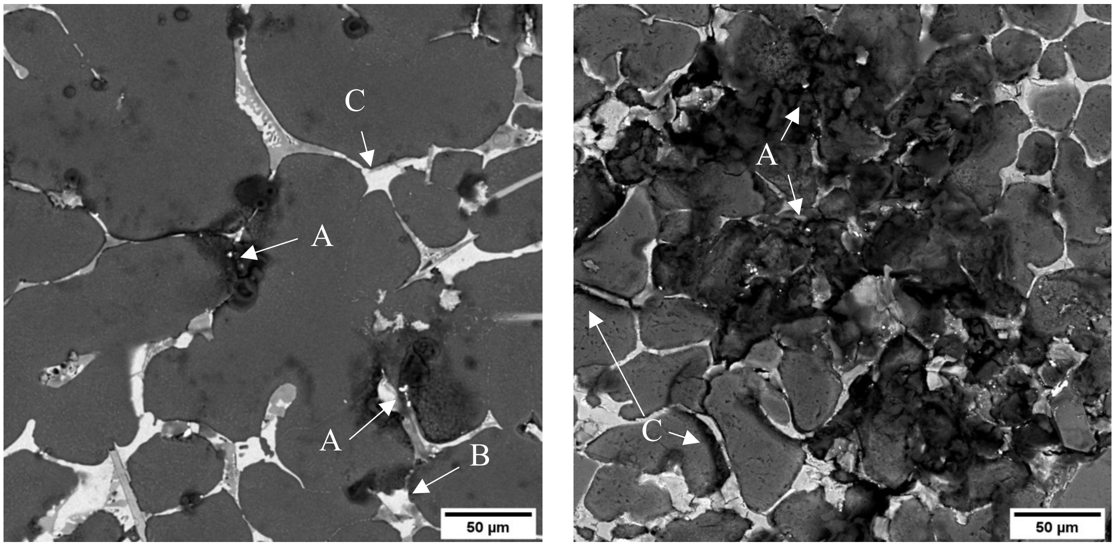

(a) (b)

Figure 4.18. SEM images of as-cast DAs in 0.59 M KCl at 90°C after 60 seconds. (a) DA13 and (b) DA18

4.5 Mechanical properties

Figure 4.19 displays the mechanical properties of the as-cast alloys at room temperature. The highest hardness among all the DAs is 130 HV for DA25, followed by DA27, DA18, and DA13 at values of 122, 113, and 110 HV, respectively. The presence of the low intermetallic phases significantly affects the mechanical properties of the DAs. When the GIS content is high (3 wt. %), the hardness dropped for DA18. Even though DA13, DA25, and DA27 have the same GIS content (1.5 wt. %), the hardness of DA13 was relatively less. Since DA25 and DA27 have more Cr and Zr in their chemistry, the higher hardness could be explained by the dissolution of finely dispersed Al_3Zr and Cr-rich precipitates in the Al matrix causing pinning and hindering effects [123, 124].

As shown in Figure 4.19(b), all DAs exhibited low ductility due to the coarse intermetallic phases present. Interestingly, DA13 exhibits the highest UTS of 74.24 MPa compared to the other DAs. DA18 and DA27 have comparable UTS of 46.27 and 47.34 MPa, respectively, while the UTS of DA25 lay in between with a value of 61.26 MPa. In terms of elongation, all DAs showed low elongation with values ranging from 0.019 % for D18 at the lower end, and 0.053 % for DA27 at the higher end. This behavior can be explained by Cr- and Zr-bearing intermetallic phases present in the DAs. Upon examining the microstructure of the DAs (Figure 4.8), the coarse intermetallic phases such as Al_3Zr and/or $Al_{45}Cr_7$ appeared in all the DAs, except for DA13. The presence of such coarse phases affects the strength of the alloys in two ways: (1) Cr and Zr are consumed to form their respective phases, thus, reducing their content in the Al matrix, and (2) coarse intermetallic phases are initiators for crack and crack propagation when the alloys are under external stress. Further addition of Cr and Zr introduces more coarse intermetallic phases in the DAs, which causes high-stress concentration around them. Therefore, upon applying external stress, cracks initiate around the coarse particles and propagate [123].

It was also observed that the hardness of DA13 was not in agreement with the alloy’s UTS. The alloy exhibited the highest UTS while the hardness was at its lowest relative to the other DAs. This could be explained by the other alloying elements' effects, which will be discussed in the next section.

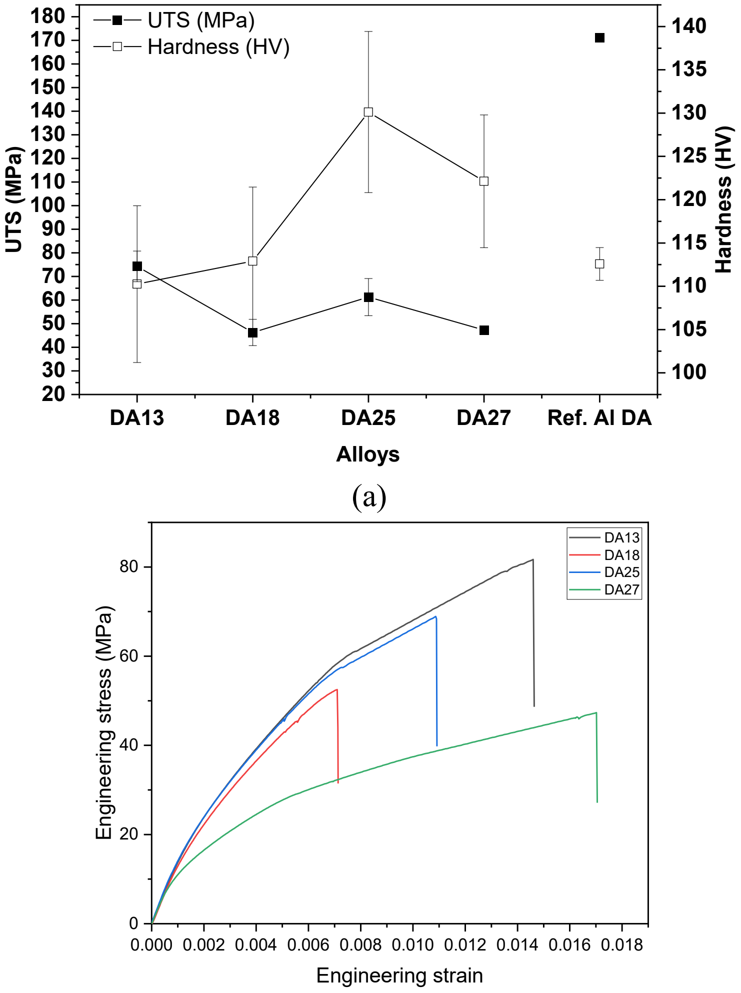

(a)

(b)

Figure 4.19. (a) Mechanical properties of as-cast DAs at room temperature, and (b) engineering stress-strain curves.

In addition, since the DAs understudy are not heat treatable at elevated temperatures, a preliminary study was carried out to further investigate the possibility of increasing the hardness of the alloy. Different heat treatments were performed to increase the hardness of the alloys. Heat treatment schedules are listed in Table 4.5. An electrical resistance furnace (Sentry Xpress 4.0, Orton) was used with a heating rate of 5 °C/min.

Table 4.5. Solution heat treatment procedures for the DAs. The water temperature used for quenching is 25 °C.

	Step 1	Step 2	Step 3	Step 4
As cast	-	-	-	-
T1	180 °C for 24 h	Quench in water	-	-
T2	70 °C for 12 h	135 °C for 8 h	Quench in water	-
T3	180 °C for 24 h	70 °C for 12 h	135 °C for 8 h	Quench in water

Figure 4.20 shows the hardness of the three different heat treatments. According to the SG solidification paths of the DAs in Figures 4.2 and 4.3, the hardness of the alloys was tested after heat treating the alloys at 180 °C for 24 hours to minimize the formation of the liquid phase. As shown in Figure 4.20, the hardness of the DAs dropped by 6, 10, 27, and 16 for DA13, DA18, DA25, and DA27, respectively. Performing two-step aging treatment (T2), however, appeared to work and increased the hardness of all the DAs, except DA25. A slight increase in hardness was also observed when performing the two-step aging treatment after heat treating the alloys for 24 hours at 180 °C. However, the hardness only increased after T2 heat treatment. Previous studies also confirmed the improvement of mechanical properties upon two-step aging treatment for Al-Zn-Mg-Cu alloys [125–127]

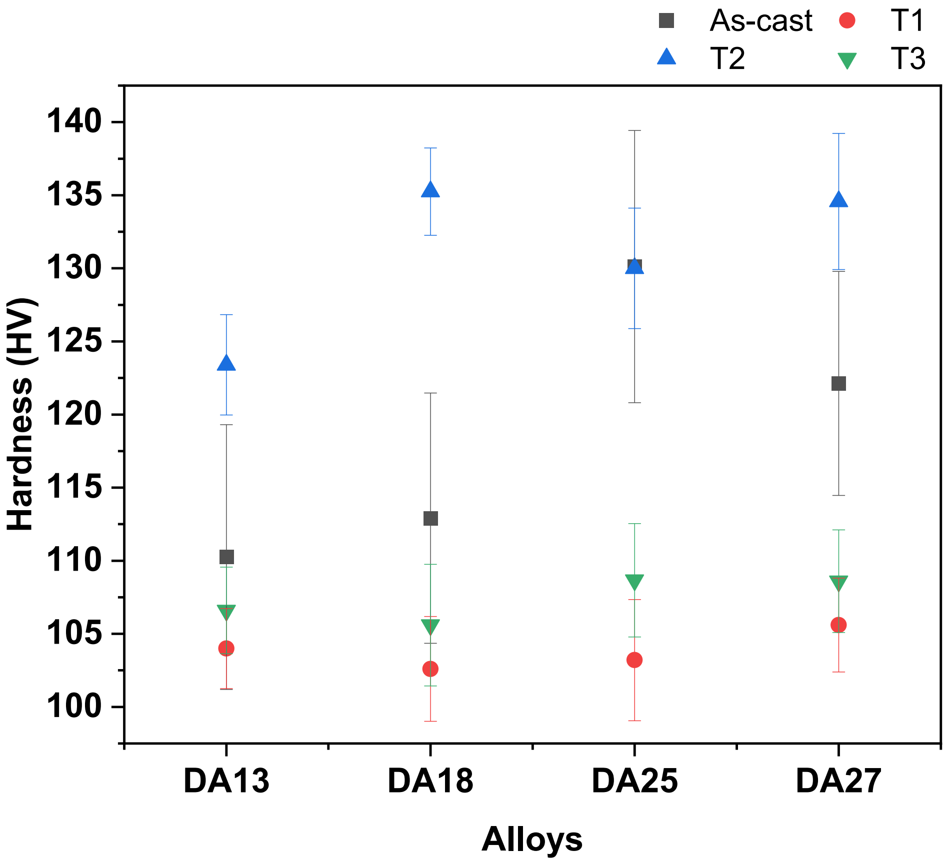

Figure 4.20. Microhardness of DAs 13, 18, 25, and 27 at different heat-treating conditions.

While studying the fracture morphologies of the DAs was not the focus of the present work, consideration is given to relating the causes of the low strength and elongation. Figure 4.21 shows the tensile fracture surface of samples at room temperature. Some pores were found on the surface and no dimples were found. All the as-cast DAs showed the characteristic of inter-granular brittle fracture. In Figures 4.21 (b) and (c), all the DAs show cleavage facets, and several microcracks were found as well as seen in DA25 and DA27. As previously discussed, the as-cast DAs consist of a solid solution of α-Al phase as a matrix and other phases at the grain boundaries such as θ-Al_2Cu, η-$MgZn_2$, and Mg_2Sn. The intermetallic phases present in grain boundaries act as crack initiators and cause fracture by cleavage. Similar effects are caused by the presence of impurities such as the needle-like shape Al_7Cu_2Fe phase.

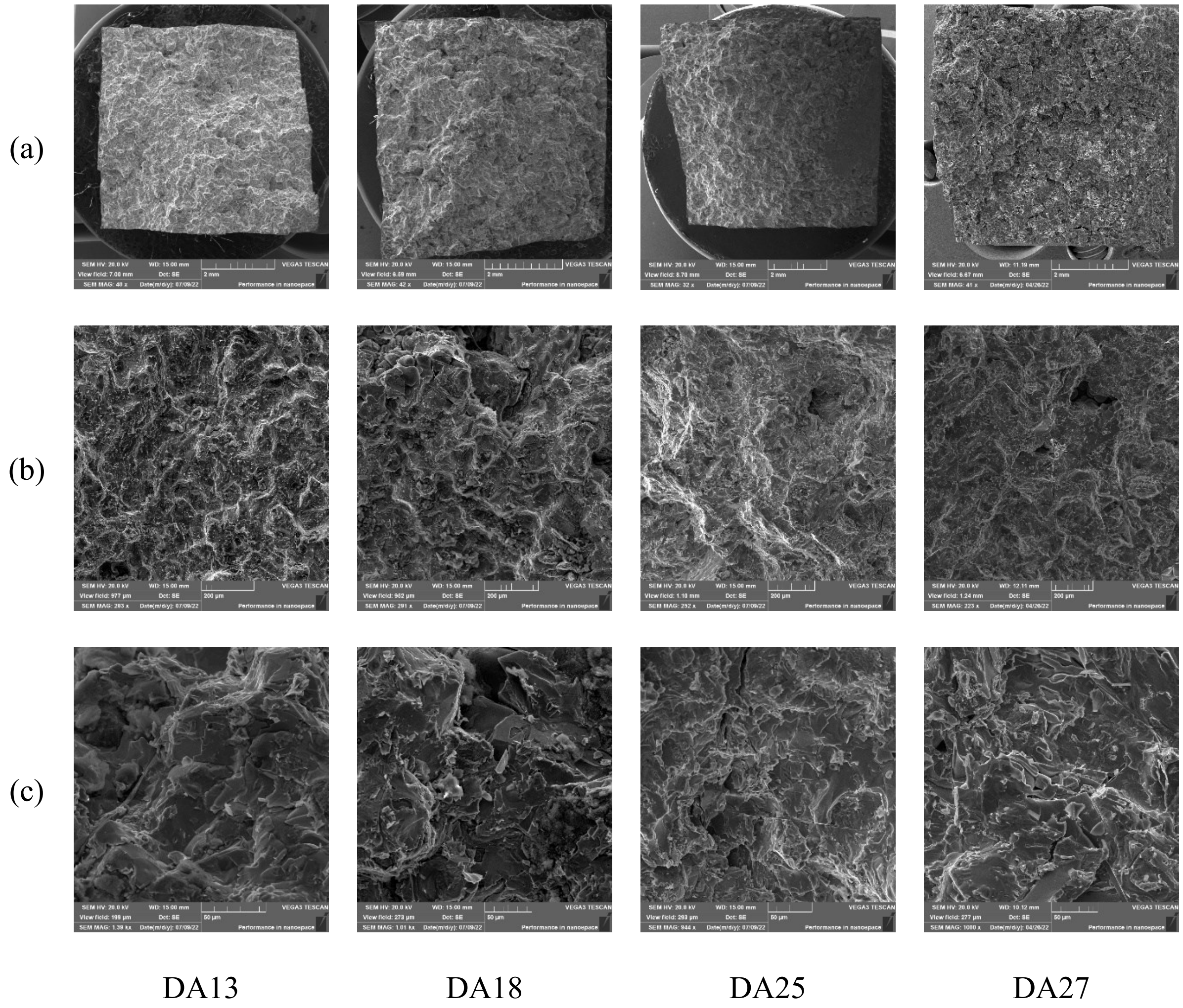

Figure 4.21. Tensile fracture morphologies of the as-cast DAs.

4.6 Summary of the influence of alloying elements on DA performance

Constructing comparisons based on the ratios of Cu:Mg and Zn:Cu, GIS, and Cr + Zr give an insight into the effect of alloying elements on the corrosion and mechanical performance of the alloys. Figure 4.21 visualizes the influence of these alloying elements by comparing the DAs with similar compositions (*i.e.*, DA25 vs. DA27, DA13 vs. DA25, and DA13 vs. DA18).

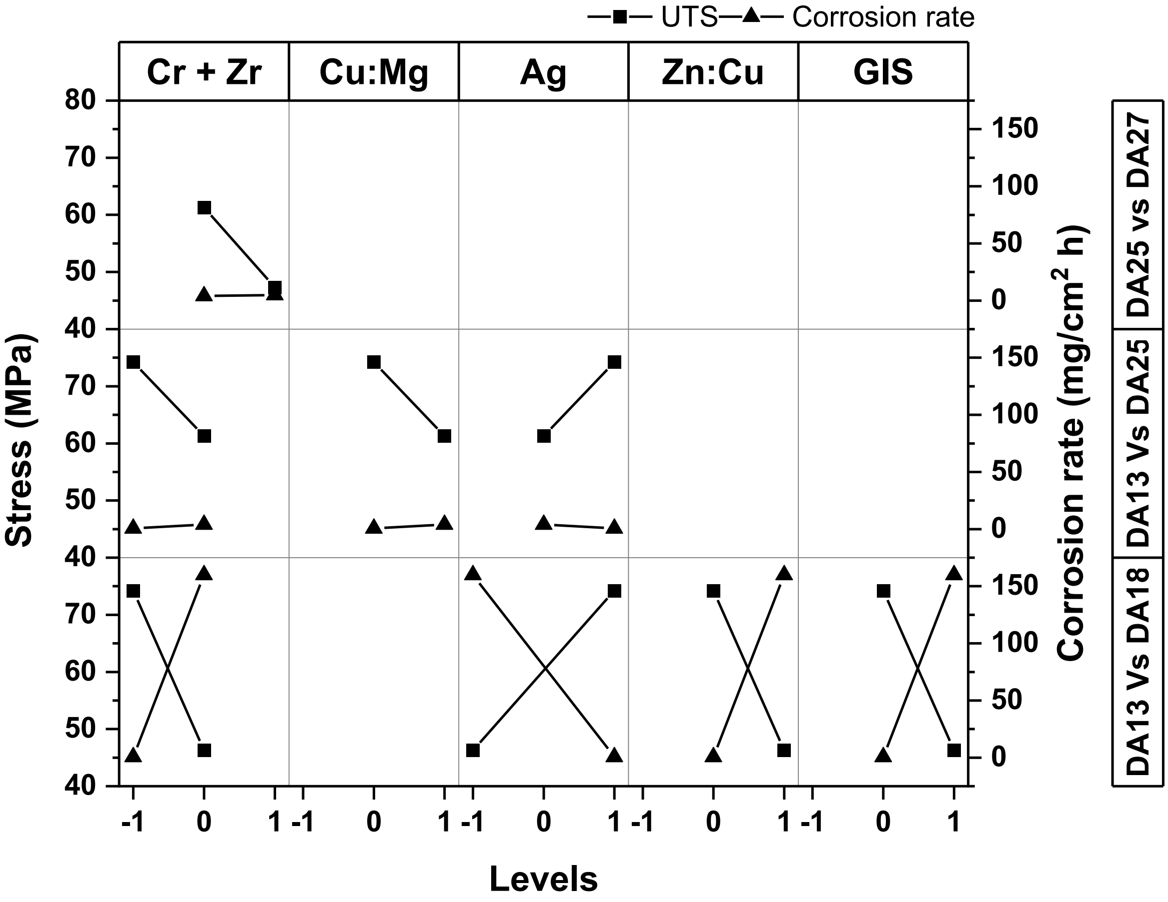

Figure 4.22. Interaction plot of alloying elements and their influence on UTS and corrosion rate.

The combined effect of Cr and Zr can be extracted from the comparison between DA25 and DA27. Both alloys have the same contents of alloying elements except for Cr and Zr. While the corrosion rate difference remains insignificant moving to the higher end of Cr and Zr content, higher strength was observed at the lower end of the combined Cr and Zr content owing to the movement of the dislocations around the coarse particles rather than through them [128]. A similar result can be obtained when examining Cr and Zr content between DA13 and DA25.

Comparison of DA13 with DA25, at constant Zn:Cu ratio and GIS content, provides an insight into the impact of Cu:Mg ratio and Ag on the DAs. In terms of corrosion rates, a slight increase occurred moving to the higher level of Cu:Mg ratio and lower level of Ag content. For mechanical strength, it was observed that setting Cu:Mg ratio at the lower end and Ag content at the higher end provided higher strength. In addition, the less Cr and Zr content contributes the higher strength of the DAs, which confirms the conclusion made in comparing DA25 and DA27. Details on how Cr and Zr affect the strength were discussed in section 4.4. Besides, the higher ratio of Cu:Mg promotes the formation of θ-Al_2Cu [112, 129]. Sufficient coarsening of θ particles reduces the mechanical properties of the alloys as is the case for Cr and Zr intermetallic phases [108]. The ongoing comparison, however, provides a vague conclusion on the effect of Ag on the mechanical properties as Ag tends to dissolve in the Al matrix and η-$MgZn_2$ phase.

Significant corrosion rate changes can be seen when comparing DA13 with DA18. As previously discussed in section 4.3, the fast dissolution is mainly attained through the GIS content in the DAs. However, a trade-off exists between dissolvability and mechanical strength. The trade-off sources from Al grains softening due to the diffusion of liquid metals (*i.e.*, Ga, In, and Sn), which is the key for Al corrosion activation. Embrittlement takes place owing to the limited solubility of a liquid phase in a solid metal, which is the case for In and Sn dissolution in Al [54]. This explains the lowest mechanical behavior of DA18 comprising GIS content at the higher level of 3 wt. % and all the DAs' brittle behavior compared to Al-Zn-Mg-Cu high strength alloys in general.

In summary, high dissolution rates of Al-based DAs are significantly associated with the presence and composition of the GIS elements. Higher content of GIS results in the highest corrosion rates in the ongoing study. However, fast dissolution comes at a cost of weakening the DAs mechanical properties. Therefore, there should be an optimum composition where a satisfactory performance of the DAs is met. The current results suggest that decreasing the Cr, Zr, Cu:Mg ratio and GIS content would yield favorable results in terms of mechanical properties. Fortunately, the decrease in GIS content should not affect the dissolution rate significantly. Moreover, the performance of the designed DA should at least match the current commercial DAs. Therefore, there exists a potential to enhance the mechanical properties of DA18 to meet the application requirements as its dissolution rate is 5.11 times the commercial Al-based DA considered in this study.

Chapter 5. Conclusions and future work

The presented thesis explored different compositional possibilities of alloying elements to synthesize an Al-based DA with favorable characteristics that meet the application needs. The alloying elements were added to Al-Zn-Cu-Mg alloys and included Ga, In, Sn, and Ag as corrosion boosters as well as Cr and Zr for mechanical properties enhancement. The following section will spot the light on concluding remarks on the results obtained in this study. The future work is then presented to highlight possible directions and challenges for further investigations.

5.1 Conclusions

Four main objectives were covered in the work. Firstly, a literature review was conducted to summarize the influence of different alloying elements on AAs followed by alloying elements selection. The selection of the alloying elements mandated the investigation of cation-type effects on selected AAs. After the compositions of potential Al-based DAs were selected, prediction of intermetallic phases was carried out using the SG model. Based on the simulation results, the final objective was performed, and it included the casting and evaluation of the corrosion and mechanical behavior of the most promising four DAs. The conclusions of each of these objectives will be touched on individually in the following sub-sections.

5.1.1 Literature review and selection of the alloying elements

In order to develop a novel Al-based DA with fast dissolvability and improved mechanical properties, a preliminary investigation was conducted on reviewing the influence of alloying elements on AAs behavior. It was found that the abundant EC data on the literature on AAs were in NaCl solution while the main chemistry in downhole environments is in KCl. EC analysis was performed to study the effect of associated cation type on the corrosion of selected AAs. In summary, the following conclusions are drawn:

- Effects of various alloying elements: (i) Ga, In, and Sn significantly influence the hydrolysis reaction of Al owing to the formation of low melting point intermetallic phases which weaken the Al_2O_3 layer. The phases act as inert by the diffusion of Al atoms into the reaction sites, which results in the continuity of the reaction; (ii) Mg, Cu, and Zn addition to Al-Ga-In-Sn alloys modifies the chemistries of the grain boundaries (including GIS composition) and the formed intermetallic phases such as Al_2Cu. This modification alters the GIS compositions at grain boundaries as well as reduces the Al/GIS contact area which is found to hinder the dissolution process; (iii) Ag addition, in small quantities, enhances the mechanical properties of AAs via the reduction of PFZs. In addition, since Ag is nobler than Al, it would create localized galvanic corrosion cells that would improve the dissolution process; (iv) Cr, Zr, and Er addition further improve the mechanical properties of AAs as they refine AAs microstructure.
- Influence of associated cation type: it was experimentally shown that the cation type (Na^+ vs K^+) had insignificant effects on the corrosion of selected AAs. The EC tests were performed with solutions of similar Cl^- concentration. It is, therefore, possible to expand the corrosion database by adopting published results in NaCl solution from the literature.
- Alloying elements selection: based on the conclusions drawn above, the chemistries of potential Al-based DAs were determined with a group of targeted alloying elements. The base AA considered is Al-Zn-Mg-Cu (i.e., 7xxx series alloys of high mechanical strength), and the selected alloying elements are Ga, In, Sn, Ag, Cr, and Zr.

5.1.2 Prediction of intermetallic phases

Prediction of intermetallic phases: SG model was used to investigate the formed phases during solidification through ThermoCalc software. Knowing the intermetallic phases gave an insight into the performance of its relative alloys based on literature findings. The selection was based on the abundance of those phases in the alloys. In particular, the results revealed the formation of η-$MgZn_2$, S-Al_2CuMg, and θ-Al_2Cu phases which are common in high mechanical strength 7xxx series AAs. The model also predicted the formation of Mg_2Zn_{11} and Mg_2Sn phases, which are electrochemically active. In addition, Al_3Zr, $Al_{45}Cr_7$, and Al_5Cr phases were also predicted. Those phases enhance the mechanical strength of the alloys if present in proper size and concentration. Considering the effects of these phases in terms of dissolvability and mechanical properties, DAs 13, 18, 25, and 27 are anticipated to be the best candidate alloys for application in hydraulic fracturing.

5.1.3 Casting and performance evaluation of the selected DAs

The four selected DAs were cast using traditional melting and casting techniques to evaluate the corrosion behavior and the mechanical strength of the as-cast alloys. The main findings are summarized below:

- Microstructure analyses were investigated using XRD and SEM/EDS. The DAs consisted mainly of four phases: α-Al, η-$MgZn_2$, Mg_2Sn, and θ-Al_2Cu. While Cu, Zn, Mg, Ag, and Cr partially existed in Al grains, Ga was mainly found distributed in Al grains. Two types of In-containing phases were also found in the microstructure out of which one is associated with Sn having composition close to In_3Sn phase. The other In-containing phase was mainly associated with Al. The grain size of the four DAs was comparable. In addition, a small deviation in the phase fraction of α-Al in the experiment alloys was observed compared to the phase fraction calculated in the SG model.

- The corrosion performance was studied using immersion tests and SEM imaging. DA18 gave the highest degradation rate of 177.76 mg/cm^2 h in 0.59 M KCl solution, which outperforms the reference Al-based and Mg-based DAs. The corrosion rate of DA18 is 5.11 times the corrosion rate of the reference Al-based DA and 2.86 times the corrosion rate of the reference Mg-based DA. SEM imaging revealed that the In-containing phases were mainly the source of Al degradation. In addition, localized corrosion was also observed in terms of IGC and pitting.
- The addition of GIS decreased the mechanical properties compared to Al-Zn-Mg-Cu alloys reported in the literature. The maximum hardness reported was 130 HV for DA25 followed by DA27, DA18, and DA13 at values of 122, 113, and 110 HV, respectively. All DAs exhibited brittle behavior. As the GIS content of DA18 is the highest, its UTS and elongation were the lowest at 46.27 MPa and 0.019%.
- In terms of the influence of the alloying elements, the coarse Cr- and Zr-bearing intermetallic phases acted as crack initiators under external stress. In addition, the formation of such coarse phases tended to reduce the amount of Cr and Zr in the Al grains preventing strengthening effects. Similarly, the formation of coarse θ-Al_2Cu was associated with high Cu:Mg ratios (as is the case for DA25 and DA27), which again caused the embrittlement of the DAs. In addition, Ag addition tended to stabilize the IGC cells as it dissolved in the Al matrix as well as the η-$MgZn_2$ phase. In turn, it reduced the potential difference gap between the Al grains and the secondary η phase.

It is believed there exists an optimized composition of Al-based DA which would yield fast degradation in downhole environments while having sufficient mechanical strength for the application. The presented study provided a detailed analysis of which alloying elements should be considered in the Al-based DAs as well as their compositions. Since DA18 has a significantly fast corrosion rate, it is practical to increase its strength by adjusting its chemistry. Further research will be conducted to further enhance the selected DA.

5.2 Future work

The future directions for the design of an Al-based DA could take different adaptations including the choice of a different AA base. Yet, the present study provided fruitful outcomes and should further be explored. Below are a few proposals to be tested:

1. To enhance the mechanical properties, the coarse intermetallic phases should be eliminated. Based on the results discussed in Chapter 4, the Cr and Zr content as well as the Cu:Mg ratio should be decreased. While the former will prevent the formation of coarse Al_3Zr and $Al_{45}Cr_7$ at the grain boundaries, the latter will maintain θ-Al_2Cu at its minimum. In addition, it is possible to decrease the GIS content to values between 1.5 wt. % and 3 wt. %. This may reduce the dissolution of the DA yet will guarantee the increase in mechanical strength. Further discussion is provided in Appendix B.
2. Decreasing the grain size could potentially increase the corrosion rate. The smaller the grains the greater the contact area with intermetallic phases form at the grain boundaries. The modification of the microstructure could be achieved by quenching the ingots at higher temperatures. It should also be noted that heat-treating might not be practical as there exist

low intermetallic phases in the DA. A preliminary study was performed to decrease the grain size of DA18. More details can be found in Appendix B.

3. Although changing the base AA is out of the scope of the study, it is still an option. Among all the alloys, a quaternary AlCuMgSi alloy is a potential candidate as it has an outstanding mechanical property. However, introducing GIS into the alloy might change the microstructure significantly as Mg tends to form intermetallic phases with Ga and Sn. Simulation analysis would be useful prior to conducting any experimental studies.

The development of a DA that meets the downhole applications is attainable. The economic and environmental benefits it adds to hydraulic fracturing make it an interesting research field. As it is a new approach, many aspects of this technology are still being discovered. With a little more investment, it has the potential to replace the current non-dissolvable downhole tools.

References

1. Xu DJ, Liao RQ, Li ZW, et al (2015) Research on Productivity for Multi-stage Fracturing of Horizonal Wells. Chem Eng Trans 46:1189–1194. https://doi.org/10.3303/CET1546199
2. Walton Z, Fripp M, Porter J, Vargus G (2019) Evolution of Frac Plug Technologies – Cast Iron to Composites to Dissolvable. In: SPE Middle East Oil and Gas Show and Conference, MEOS, Proceedings. OnePetro
3. Canada Chevron Hydraulic Fracturing. https://canada.chevron.com/environment/hydraulic-fracturing. Accessed 14 Jan 2022
4. Energy Board - NEB N (2013) Canada's Energy Future 2013 - Energy Supply and Demand Projections to 2035 - An Energy Market Assessment - November 2013
5. Garcilazo Meza G, Bautista Alarcon X, Loundy R (2020) A Detailed Evaluation of Coiled Tubing Drillouts of Composites and Dissolvable Plugs In Permian Basin and Eagle Ford Fields. In: Society of Petroleum Engineers - SPE/ICoTA Well Intervention Conference and Exhibition 2020, CTWI 2020. OnePetro
6. Li M, Chen L, Wei R, et al (2018) The application of fully dissolvable frac plug technique in Weiyuan gasfield. In: Society of Petroleum Engineers - SPE Kingdom of Saudi Arabia Annual Technical Symposium and Exhibition 2018, SATS 2018. Society of Petroleum Engineers
7. Salinas BJ, Xu Z, Agrawal G, Richard B (2012) Controlled Electrolytic Metallics-An Interventionless Nanostructured Platform. SPE Int. Oilf. Nanotechnol. Conf. Exhib. SPE-153428-MS
8. Nine Energy Service (2020) MAGNUM FASTBALL ™ DM
9. ASM International (2018) Terves to expand magnesium foundry for manufacturing dissolvable metal tools - ASM International. https://www.asminternational.org/home/-/journal_content/56/10180/35028237/NEWS. Accessed 14 Aug 2021
10. Liu J, Shao Z, Zhang X (2019) Development of a High-Strength Soluble Aluminum Alloy and Its Application in Oil Pressure Cracking. Chem Technol Fuels Oils 54:818–823. https://doi.org/10.1007/s10553-019-00992-z
11. Norman T, Walton Z, Fripp M (2018) Full dissolvable frac plug for high-temperature wellbores. In: Proceedings of the Annual Offshore Technology Conference. Offshore Technology Conference, pp 312–321
12. Fripp M, Walton Z, Norman T (2017) Fully dissolvable fracturing plug for low-temperature wellbores. In: Proceedings - SPE Annual Technical Conference and Exhibition. Society of Petroleum Engineers (SPE)
13. Fripp M, Walton Z (2016) Degradable metal for use in a fully dissolvable frac plug. In: Proceedings of the Annual Offshore Technology Conference. Offshore Technology Conference, pp 3467–3475

14. Megson THG (2019) Introduction. In: Structural and Stress Analysis, Fourth Edi. Butterworth-Heinemann, Amsterdam, pp 1–16

15. Hirsch J (2011) Aluminium sheet fabrication and processing. In: Roger Lumley (ed) Fundamentals of Aluminium Metallurgy: Production, Processing and Applications. Woodhead Publishing, Oxford, UK, pp 719–746

16. Wang W, Zhao XM, Chen DM, Yang K (2012) Insight into the reactivity of Al-Ga-In-Sn alloy with water. Int J Hydrogen Energy 37:2187–2194. https://doi.org/10.1016/j.ijhydene.2011.10.058

17. Flamini DO, Saidman SB (2012) Electrochemical behaviour of Al-Zn-Ga and Al-In-Ga alloys in chloride media. Mater Chem Phys 136:103–111. https://doi.org/10.1016/j.matchemphys.2012.06.036

18. Saidman SB, Garcia SG, Bessone JB (1995) Electrochemical behaviour of Al-ln alloys in chloride solutions. J Appl Electrochem 25:252–258

19. Lin JC, Shih HC (1987) Improvement of the Current Efficiency of an Al-Zn-In Anode by Heat-Treatment. J Electrochem Soc 134:817–823. https://doi.org/10.1149/1.2100578/XML

20. Chen X, Xia Y, Liu Z, Gao Z (2021) Effect of Mercury(II) Ions on the Corrosion Resistance of Aluminium Alloy Coatings in 3.5% wt. NaCl solution. Int J Electrochem Sci 16:211042. https://doi.org/10.20964/2021.10.46

21. Keir DS, Pryor MJ, Sperry PR (1967) Galvanic Corrosion Characteristics of Aluminum Alloyed with Group IV Metals. J Electrochem Soc 114:777. https://doi.org/10.1149/1.2426735/XML

22. Osório WR, Freitas ES, Garcia A (2013) EIS parameters and cell spacings of an Al–Bi alloy in NaCl solution. Electrochim Acta 108:781–787. https://doi.org/10.1016/J.ELECTACTA.2013.07.036

23. Yang B, Zhu J, Jiang T, et al (2017) Effect of heat treatment on AlMgGaInSn alloy for hydrogen generation through hydrolysis reaction. Int J Hydrogen Energy 42:24393–24403. https://doi.org/10.1016/J.IJHYDENE.2017.07.091

24. Bennett JE, Pinnel MR (1973) Reactions between mercury-wetted aluminium and liquid water. J Mater Sci 1973 88 8:1189–1193. https://doi.org/10.1007/BF00632772

25. Smith IE (1972) HYDROGEN GENERATION BY MEANS OF THE ALUMINUM/WATER REACTION. J Hydronautics 6:106–109. https://doi.org/10.2514/3.48127

26. Deng ZY, Tang Y Bin, Zhu LL, et al (2010) Effect of different modification agents on hydrogen-generation by the reaction of Al with water. Int J Hydrogen Energy 35:9561–9568. https://doi.org/10.1016/J.IJHYDENE.2010.07.027

27. Chen X, Zhao Z, Hao M, Wang D (2013) Research of hydrogen generation by the reaction of Al-based materials with water. J Power Sources 222:188–195. https://doi.org/10.1016/J.JPOWSOUR.2012.08.078

28. Fan MQ, Xu F, Sun LX (2007) Studies on hydrogen generation characteristics of hydrolysis of the ball milling Al-based materials in pure water. Int J Hydrogen Energy 32:2809–2815. https://doi.org/10.1016/J.IJHYDENE.2006.12.020

29. Yuan B, Tan S, Liu J (2016) Dynamic hydrogen generation phenomenon of aluminum fed liquid phase Ga–In alloy inside NaOH electrolyte. Int J Hydrogen Energy 41:1453–1459. https://doi.org/10.1016/J.IJHYDENE.2015.10.044

30. Flamini DO, Saidman SB, Bessone JB (2007) Electrodeposition of gallium and zinc onto aluminium. Influence of the electrodeposited metals on the activation process. Thin Solid Films 515:7880–7885. https://doi.org/10.1016/j.tsf.2007.04.016

31. Srinivas M, Adapaka SK, Neelakantan L (2016) Solubility effects of Sn and Ga on the microstructure and corrosion behavior of Al-Mg-Sn-Ga alloy anodes. J Alloys Compd 683:647–653. https://doi.org/10.1016/J.JALLCOM.2016.05.090

32. Soler L, Candela AM, Macanás J, et al (2009) In situ generation of hydrogen from water by aluminum corrosion in solutions of sodium aluminate. J Power Sources 192:21–26. https://doi.org/10.1016/J.JPOWSOUR.2008.11.009

33. Skrovan J, Alfantazi A, Troczynski T (2011) Hydrogen Generation by Accelerating Aluminum Corrosion in Water with Alumina. Int J Mater Metall Eng 5:565–570. https://doi.org/10.5281/ZENODO.1061180

34. Foley RT (1986) Localized Corrosion of Aluminum Alloys—A Review. Corrosion 42:277–288. https://doi.org/10.5006/1.3584905

35. McCafferty E (2010) Crevice Corrosion and Pitting. In: Introduction to Corrosion Science. Springer New York, New York, NY, pp 263–313

36. Cragnolino GA (2008) Corrosion fundamentals and characterization techniques. In: Lietai Yang (ed) Techniques for Corrosion Monitoring. Woodhead Publishing, pp 6–45

37. Scamans GM, Birbilis N, Buchheit RG (2010) Corrosion of Aluminum and its Alloys. In: Bob Cottis, Michael Graham, Robert Lindsay, et al (eds) Shreir's Corrosion. Elsevier, pp 1974–2010

38. Venugopal A, Raja VS (1996) Evidence of dissolution-redeposition mechanism in activation of aluminium by indium. Br Corros J 31:318–320. https://doi.org/10.1179/BCJ.1996.31.4.318

39. Breslin CB, Friery LP, Carroll WM (1994) The electrochemical behaviour of Al-Zn-In and Al-Zn-Hg alloys in aqueous halide solutions. Corros Sci 36:85–97. https://doi.org/10.1016/0010-938X(94)90111-2

40. Woodall JM, Ziebarth JT, Allen CR, et al (2009) Recent Results on Splitting Water with Aluminum Alloys. Ceram Trans 202:119–127. https://doi.org/10.1002/9780470483428.CH13

41. Hong MS, Park IJ, Kim JG (2017) Alloying effect of copper concentration on the localized corrosion of aluminum alloy for heat exchanger tube. Met Mater Int 23:708–714. https://doi.org/10.1007/s12540-017-6589-9

42. El Warraky AA, El-Aziz AM, Soliman KA (2007) Copper redeposition and surface enrichment during the dissolution of Al-Cu alloys in different concentrations of NaCl solution. Part 1 - Electrochemical measurements. Anti-Corrosion Methods Mater 54:155–162. https://doi.org/10.1108/00035590710748623

43. Afzali P, Yousefpour M, Borhani E (2018) Effect of Deformation-Induced Defects on the Microstructure and Pitting Corrosion Behavior of Al-Ag Alloy. Int J Eng 31:2092–2101. https://doi.org/10.5829/ije.2018.31.12c.14

44. El Shayeb HA, Abd El Wahab FM, Zein El Abedin S (2001) Effect of gallium ions on the electrochemical behaviour of Al, Al-Sn, Al-Zn and Al-Zn-Sn alloys in chloride solutions. Corros Sci 43:643–654. https://doi.org/10.1016/S0010-938X(00)00100-1

45. Gudić S, Smoljko I, Kliškić M (2010) Electrochemical behaviour of aluminium alloys containing indium and tin in NaCl solution. Mater Chem Phys 121:561–566. https://doi.org/10.1016/j.matchemphys.2010.02.040

46. Venugopal A, Raja VS (1997) AC impedance study on the activation mechanism of aluminium by indium and zinc in 3.5% NaCl medium. Corros Sci 39:2053–2065. https://doi.org/10.1016/S0010-938X(97)00082-6

47. Baer DR, Windisch CF, Engelhard MH, et al (2000) Influence of Mg on the corrosion of Al. J Vac Sci Technol A Vacuum, Surfaces, Film 18:131–136. https://doi.org/10.1116/1.582129

48. Birbilis N, Buchheit RG (2005) Electrochemical Characteristics of Intermetallic Phases in Aluminum Alloys. J Electrochem Soc 152:B140. https://doi.org/10.1149/1.1869984

49. Khireche S, Boughrara D, Kadri A, et al (2014) Corrosion mechanism of Al, Al-Zn and Al-Zn-Sn alloys in 3wt.% NaCl solution. Corros Sci 87:504–516. https://doi.org/10.1016/j.corsci.2014.07.018

50. Fang HC, Chao H, Chen KH (2014) Effect of Zr, Er and Cr additions on microstructures and properties of Al-Zn-Mg-Cu alloys. Mater Sci Eng A 610:10–16. https://doi.org/10.1016/j.msea.2014.05.021

51. Gupta RK, Fabijanic D, Zhang R, Birbilis N (2015) Corrosion behaviour and hardness of in situ consolidated nanostructured Al and Al-Cr alloys produced via high-energy ball milling. Corros Sci 98:643–650. https://doi.org/10.1016/j.corsci.2015.06.011

52. Ziebarth JT, Woodall JM, Kramer RA, Choi G (2011) Liquid phase-enabled reaction of Al–Ga and Al–Ga–In–Sn alloys with water. Int J Hydrogen Energy 36:5271–5279. https://doi.org/10.1016/J.IJHYDENE.2011.01.127

53. He TT, Wang W, Chen W, et al (2017) Influence of In and Sn compositions on the reactivity of Al–Ga–In–Sn alloys with water. Int J Hydrogen Energy 42:5627–5637. https://doi.org/10.1016/J.IJHYDENE.2016.11.112

54. Trenikhin M V., Bubnov A V., Nizovskii AI, Duplyakin VK (2006) Chemical interaction of the In-Ga eutectic with Al and Al-base alloys. Inorg Mater 42:256–260. https://doi.org/10.1134/S0020168506030083

55. Villars P, Prince A OH (1997) In: Al-In-Sn phase diagram. In: Handbook of ternary alloy phase diagrams, 2nd ed. ASM International, pp 11045–11045

56. Du BD, He TT, Liu GL, et al (2018) Al-water reactivity of Al–Mg–Ga–In–Sn alloys used for hydraulic fracturing tools. Int J Hydrogen Energy 43:7201–7215. https://doi.org/10.1016/j.ijhydene.2018.02.090

57. Aragon E, Cazenave-Vergez L, Lanza E, et al (1997) Electrochemical behaviour of binary Al-Ga and ternary Al-Zn-Ga alloys as function of thermodynamic properties. Br Corros J 32:121–126. https://doi.org/10.1179/000705997798115011

58. Macdonald DD, Ismail KM, Sikora E (1998) Characterization of the Passive State on Zinc. J Electrochem Soc 145:3141. https://doi.org/10.1149/1.1838777

59. Ahmido A, Sabbar A, Zouihri H, et al (2011) Effect of bismuth and silver on the corrosion behavior of Sn–9Zn alloy in NaCl 3 wt.% solution. Mater Sci Eng B 176:1032–1036. https://doi.org/10.1016/J.MSEB.2011.05.034

60. He T, Chen W, Wang W, et al (2020) Effect of different Cu contents on the microstructure and hydrogen production of Al–Cu-Ga-In-Sn alloys for dissolvable materials. J Alloys Compd 821:153489. https://doi.org/10.1016/j.jallcom.2019.153489

61. Liu D, Gao Q, An Q, et al (2020) Experimental Study on Zn-Doped Al-Rich Alloys for Fast on-Board Hydrogen Production. Cryst 2020, Vol 10, Page 167 10:167. https://doi.org/10.3390/CRYST10030167

62. Liu L, Yu S, Liu E, et al (2021) Investigations on the Microstructure and Degradation Behavior of Hollow Glass Microspheres/Mg Alloy Composites. Adv Eng Mater 23:1–11. https://doi.org/10.1002/adem.202001301

63. Stefanescu DM, Ruxanda R (2004) Solidification Structures of Aluminum Alloys. In: George F. Vander Voort (ed) Metallography and Microstructures. ASM International, pp 107–115

64. Warmuzek M (2004) Metallographic Techniques for Aluminum and Its Alloys. In: George F. Vander Voort (ed) Metallography and Microstructures. ASM International, pp 711–751

65. Bangdeng D, Jun L, Xiaowan W, et al (2021) Effect of Heat Treatment on Microstructure and Al-water Reactivity of Al-Mg-Ga-In-Sn Alloys. Chinese J Mater Res 35:25–35. https://doi.org/10.11901/1005.3093.2020.080

66. He T, Chen W, Wang W, et al (2020) Microstructure and hydrogen production of the rapidly solidified Al–Mg-Ga-In-Sn alloy. J Alloys Compd 827:154290. https://doi.org/10.1016/J.JALLCOM.2020.154290

67. H. Okamoto; M.E. Schlesinger; E.M. Mueller (2016) Binary Alloy Phase Diagrams. In: Alloy Phase Diagrams. ASM International, pp 89–89

68. Speidel MO, Hyatt M V. (1972) Stress-Corrosion Cracking of High-Strength Aluminum Alloys. In: Mars G. Fontana, Roger W. Staehle (eds) Advances in Corrosion Science and Technology. Springer, Boston, MA, Boston, MA, pp 115–335

69. H. Okamoto; M.E. Schlesinger; E.M. Mueller (2016) Al (Aluminum) Binary Alloy Phase Diagrams. In: Alloy Phase Diagrams. ASM International, pp 113–139

70. Ghali E (2010) Corrosion resistance of aluminum and magnesium alloys : understanding, performance, and testing. John Wiley, Hoboken, NJ, USA

71. Ramgopal T, Schmutz P, Frankel GS (2001) Electrochemical Behavior of Thin Film Analogs of Mg (Zn , Cu , Al) 2. J Electrochem Soc 148:B348. https://doi.org/10.1149/1.1386626

72. Meng Q, Frankel GS (2004) Effect of Cu Content on Corrosion Behavior of 7xxx Series Aluminum Alloys. J Electrochem Soc 151:B271. https://doi.org/10.1149/1.1695385

73. Buchheit RG, Martinez MA, Montes LP (2000) Evidence for Cu Ion Formation by Dissolution and Dealloying the Al2CuMg Intermetallic Compound in Rotating Ring-Disk Collection Experiments. J Electrochem Soc 147:119. https://doi.org/10.1149/1.1393164

74. Ogura T, Hirosawa S, Hirose A, Sato T (2011) Effects of microalloying tin and combined addition of silver and tin on the formation of precipitate free zones and mechanical properties in Al-Zn-Mg alloys. In: Materials Transactions. The Japan Institute of Metals and Materials, pp 900–905

75. Ogura T, Otani T, Hirose A, Sato T (2013) Improvement of strength and ductility of an Al-Zn-Mg alloy by controlling grain size and precipitate microstructure with Mn and Ag addition. Mater Sci Eng A 580:288–293. https://doi.org/10.1016/j.msea.2013.05.025

76. Gudić S, Smoljko I, Klikić M (2010) The effect of small addition of tin and indium on the corrosion behavior of aluminium in chloride solution. J Alloys Compd 505:54–63. https://doi.org/10.1016/j.jallcom.2010.06.055

77. Fayomi OSI, Popoola API, Udoye NE (2017) Effect of Alloying Element on the Integrity and Functionality of Aluminium-Based Alloy. Alum Alloy - Recent Trends Process Charact Mech Behav Appl. https://doi.org/10.5772/intechopen.71399

78. Dean S (2003) Electrochemical Methods of Corrosion Testing. https://doi.org/10.31399/ASM.HB.V13A.A0003644

79. Popov BN (2015) Corrosion Engineering: Principles and Solved Problems. Elsevier Inc., Amsterdam

80. Mansfeld F (2003) Electrochemical Methods of Corrosion Testing. Corros. Fundam. Testing, Prot. 13A:0

81. Astm G (2009) Standard test method for conducting potentiodynamic polarization resistance measurements. In: Annual Book of ASTM Standards. pp 237--239

82. Roy RK (2010) A primer on the Taguchi method., 2nd ed. Society of Manufacturing Engineers

83. Saunders N, Miodownik AP (1998) CALPHAD (Calculation of Phase Diagrams): a Comprehensive Guide. Elsevier Science & Technology, London

84. Liu ZK (2009) First-Principles Calculations and CALPHAD Modeling of

Thermodynamics. J Phase Equilibria Diffus 2009 305 30:517–534. https://doi.org/10.1007/S11669-009-9570-6

85. Saunders N (2004) The modelling of stable and metastable phase formation in multi-component al-alloys. Mater Forum 28:96–106

86. Schaffnit P, Stallybrass C, Konrad J, et al (2015) A Scheil–Gulliver model dedicated to the solidification of steel. Calphad 48:184–188. https://doi.org/10.1016/J.CALPHAD.2015.01.002

87. Sundman B, Ansara I (2008) The Gulliver–Scheil method for the calculation of solidification paths. SGTE Caseb Second Ed Thermodyn Work 343–346. https://doi.org/10.1533/9781845693954.3.343

88. Hammadi S (2018) Solidification Modeling of Microsegregation. KTH

89. Chen Q, Sundman B (2002) Computation of Partial Equilibrium Solidification with Complete Interstitial and Negligible Substitutional Solute Back Diffusion. Mater Trans 43:551–559. https://doi.org/10.2320/MATERTRANS.43.551

90. Bäckerud L, Król E, Tamminen J, et al (1986) Solidification characteristics of aluminium alloys. Skanaluminium, Oslo

91. Picard YN (2019) Scanning Electron Microscopy. Mater Charact 543–575. https://doi.org/10.31399/ASM.HB.V10.A0006668

92. Inkson BJ (2016) Scanning electron microscopy (SEM) and transmission electron microscopy (TEM) for materials characterization. Mater Charact Using Nondestruct Eval Methods 17–43. https://doi.org/10.1016/B978-0-08-100040-3.00002-X

93. Goldstein JI, Newbury DE, Echlin P, et al (2003) Special Topics in Electron Beam X-Ray Microanalysis. Scanning Electron Microsc X-ray Microanal 453–536. https://doi.org/10.1007/978-1-4615-0215-9_10

94. Altawell N (2022) Machine olfaction device nanostructure coating. Introd to Mach Olfaction Devices 139–157. https://doi.org/10.1016/B978-0-12-822420-5.00008-8

95. Zhou W, Apkarian RP, Lin Wang Z, Joy D (2006) Fundamentals of Scanning Electron Microscopy. In: Scanning microscopy for nanotechnology. Springer, pp 1–40

96. Han W, Jiao H, Fox D (2018) Scanning electron microscopy. Springer Tracts Mod Phys 272:35–68. https://doi.org/10.1007/978-981-13-0454-5_2/FIGURES/31

97. Kara U, Susoy G, Issa SAM, et al (2020) Scanning electron microscopy (SEM), energy-dispersive X-ray (EDX) spectroscopy and nuclear radiation shielding properties of [α-Fe3+O(OH)]-doped lithium borate glasses. Appl Phys A Mater Sci Process 126:1–14. https://doi.org/10.1007/S00339-020-03683-3/FIGURES/13

98. Leoni M (2019) Introduction to Diffraction Methods. Mater Charact 389–398. https://doi.org/10.31399/ASM.HB.V10.A0006643

99. Suryanarayana C, Norton MG (1998) X-Ray Diffraction. Springer US, Boston, MA

100. Lee M (2017) X-Ray Diffraction for Materials Research : From Fundamentals to Applications, 1st ed. Apple Academic Press, New York

101. Lee M (2016) Directions of X-Ray Diffraction. In: Lee M (ed) X-Ray Diffraction for Materials Research. Apple Academic Press, New York , pp 117–145

102. 21 NT− (2021) Standard Guide for Laboratory Immersion Corrosion Testing of Metals. Houston, TX: NACE

103. Hansson CM, Frølund T, Markussen JB (1985) The effect of chloride cation type on the corposion of steel in concrete by chloride salts. Cem Concr Res 15:65–73. https://doi.org/10.1016/0008-8846(85)90009-2

104. Tuutti K (1982) Corrosion of steel in concrete. Ph.D. Thesis. Swedish Cement and Concrete Research Institute, Stockholm

105. X.-M. L, Starink MJ (2013) Effect of compositional variations on characteristics of coarse intermetallic particles in overaged 7000 aluminium alloys. http://dx.doi.org/101179/026708301101509449 17:1324–1328. https://doi.org/10.1179/026708301101509449

106. Ghosh A, Ghosh M (2018) Microstructure and texture development of 7075 alloy during homogenisation. https://doi-org.login.ezproxy.library.ualberta.ca/101080/1478643520181439596 98:1470–1490. https://doi.org/10.1080/14786435.2018.1439596

107. Wang MF, Xiao DH, Sun BR, Liu WS (2019) Microstructure, mechanical properties and corrosion behavior of Al-Cu-Mg-Sn-Ga-In alloy. J Alloys Compd 776:172–180. https://doi.org/10.1016/J.JALLCOM.2018.10.290

108. Zhang Y, Li R, Chen P, et al (2019) Microstructural evolution of Al2Cu phase and mechanical properties of the large-scale Al alloy components under different consecutive manufacturing processes. J Alloys Compd 808:151634. https://doi.org/10.1016/J.JALLCOM.2019.07.346

109. Ag-Al (2016) Ag (Silver) Binary Alloy Phase Diagrams. Alloy Phase Diagrams 90–113. https://doi.org/10.31399/ASM.HB.V03.A0006143

110. Chen Z, Mo Y, Nie Z (2013) Effect of Zn content on the microstructure and properties of super-high strength Al-Zn-Mg-Cu alloys. Metall Mater Trans A Phys Metall Mater Sci 44:3910–3920. https://doi.org/10.1007/S11661-013-1731-X/TABLES/4

111. Xie F, Yan X, Ding L, et al (2003) A study of microstructure and microsegregation of aluminum 7050 alloy. Mater Sci Eng A 355:144–153. https://doi.org/10.1016/S0921-5093(03)00056-X

112. Mondal C, Mukhopadhyay AK (2005) On the nature of T(Al2Mg3Zn3) and S(Al2CuMg) phases present in as-cast and annealed 7055 aluminum alloy. Mater Sci Eng A 391:367–376. https://doi.org/10.1016/J.MSEA.2004.09.013

113. Fan X, Jiang D, Meng Q, Zhong L (2006) The microstructural evolution of an Al–Zn–Mg–Cu alloy during homogenization. Mater Lett 60:1475–1479.

https://doi.org/10.1016/J.MATLET.2005.11.049

114. Ii Y, Li P, Zhao G, et al (2005) The constituents in Al–10Zn–2.5Mg–2.5Cu aluminum alloy. Mater Sci Eng A 397:204–208. https://doi.org/10.1016/J.MSEA.2005.02.013

115. Birbilis N, Cavanaugh MK, Buchheit RG (2006) Electrochemical behavior and localized corrosion associated with Al7Cu2Fe particles in aluminum alloy 7075-T651. Corros Sci 48:4202–4215. https://doi.org/10.1016/J.CORSCI.2006.02.007

116. Zhu Y, Sun K, Frankel GS (2018) Intermetallic Phases in Aluminum Alloys and Their Roles in Localized Corrosion. J Electrochem Soc 165:C807–C820. https://doi.org/10.1149/2.0931811JES/XML

117. Zhao J-C, Zhao J-C (2007) Methods for Phase Diagram Determination. Elsevier Science & Technology, Oxford, UNITED KINGDOM

118. Rinderer B (2011) The Metallurgy of Homogenisation. Mater Sci Forum 693:264–275. https://doi.org/10.4028/WWW.SCIENTIFIC.NET/MSF.693.264

119. Birol Y (2004) The effect of homogenization practice on the microstructure of AA6063 billets. J Mater Process Technol 148:250–258. https://doi.org/10.1016/J.JMATPROTEC.2004.01.056

120. Srinivas M, Adapaka SK, Neelakantan L (2016) Solubility effects of Sn and Ga on the microstructure and corrosion behavior of Al-Mg-Sn-Ga alloy anodes. J Alloys Compd 683:647–653. https://doi.org/10.1016/j.jallcom.2016.05.090

121. Ma Z, Li X (2011) The study on microstructure and electrochemical properties of Al-Mg-Sn-Ga-Pb alloy anode material for Al/AgO battery. J Solid State Electrochem 15:2601–2610. https://doi.org/10.1007/S10008-010-1253-Z/FIGURES/9

122. Wang J, Liu Z, Bai S, et al (2020) Combined Effect of Ag and Mg Additions on Localized Corrosion Behavior of Al-Cu Alloys with High Cu Content. J Mater Eng Perform 29:6108–6117. https://doi.org/10.1007/S11665-020-05072-6/TABLES/3

123. Yang Y, Tan P, Sui Y, et al (2021) Influence of Zr content on microstructure and mechanical properties of As-cast Al-Zn-Mg-Cu alloy. J Alloys Compd 867:158920. https://doi.org/10.1016/J.JALLCOM.2021.158920

124. Li XM, Starink MJ (2011) Identification and analysis of intermetallic phases in overaged Zr-containing and Cr-containing Al–Zn–Mg–Cu alloys. J Alloys Compd 509:471–476. https://doi.org/10.1016/J.JALLCOM.2010.09.064

125. Chemingui M, Khitouni M, Jozwiak K, et al (2010) Characterization of the mechanical properties changes in an Al–Zn–Mg alloy after a two-step ageing treatment at 70° and 135 °C. Mater Des 31:3134–3139. https://doi.org/10.1016/J.MATDES.2009.12.033

126. Wang D, Ni DR, Ma ZY (2008) Effect of pre-strain and two-step aging on microstructure and stress corrosion cracking of 7050 alloy. Mater Sci Eng A 494:360–366. https://doi.org/10.1016/J.MSEA.2008.04.023

127. Li Z, Xiong B, Zhang Y, et al (2008) Investigation of microstructural evolution and

mechanical properties during two-step ageing treatment at 115 and 160 °C in an Al–Zn–Mg–Cu alloy pre-stretched thick plate. Mater Charact 59:278–282. https://doi.org/10.1016/J.MATCHAR.2007.01.006

128. Senkov ON, Shagiev MR, Senkova S V., Miracle DB (2008) Precipitation of Al3(Sc,Zr) particles in an Al–Zn–Mg–Cu–Sc–Zr alloy during conventional solution heat treatment and its effect on tensile properties. Acta Mater 56:3723–3738. https://doi.org/10.1016/J.ACTAMAT.2008.04.005

129. Lasa L, Rodriguez-Ibabe JM (2002) Characterization of the dissolution of the Al2Cu phase in two Al–Si–Cu–Mg casting alloys using calorimetry. Mater Charact 48:371–378. https://doi.org/10.1016/S1044-5803(02)00283-8

Appendix A - Schiel-Gulliver solidification curves

This section includes Scheil-Gulliver simulation results as well as additional SEM images and EDS maps for the four DAs.

A.1 Scheil Gulliver solidification curves for the DAs

A.2 Additional SEM images and EDS maps for DA13, DA18, DA25, and DA27

A.1 Scheil Gulliver solidification curves for the DAs

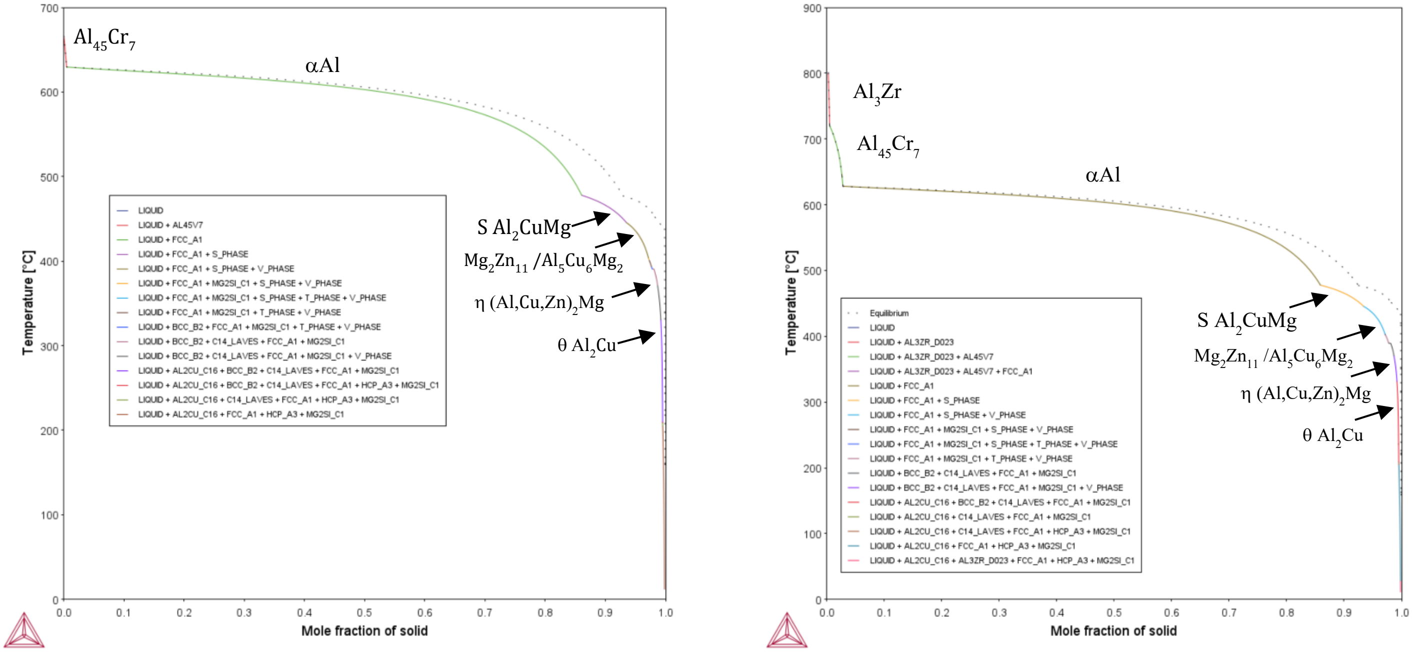

(a)

Al-4.1Cu-4Zn-2.4Mg-0.7Ag-0.88Ga-0.37In-0.25Sn-0.19Cr-0.03Ti-0.01V

(b)

Al-4.1Cu-4Zn-2.4Mg-0.7Ag-0.88Ga-0.37In-0.25Sn-0.60Cr-0.5Zr-0.03Ti-0.01V

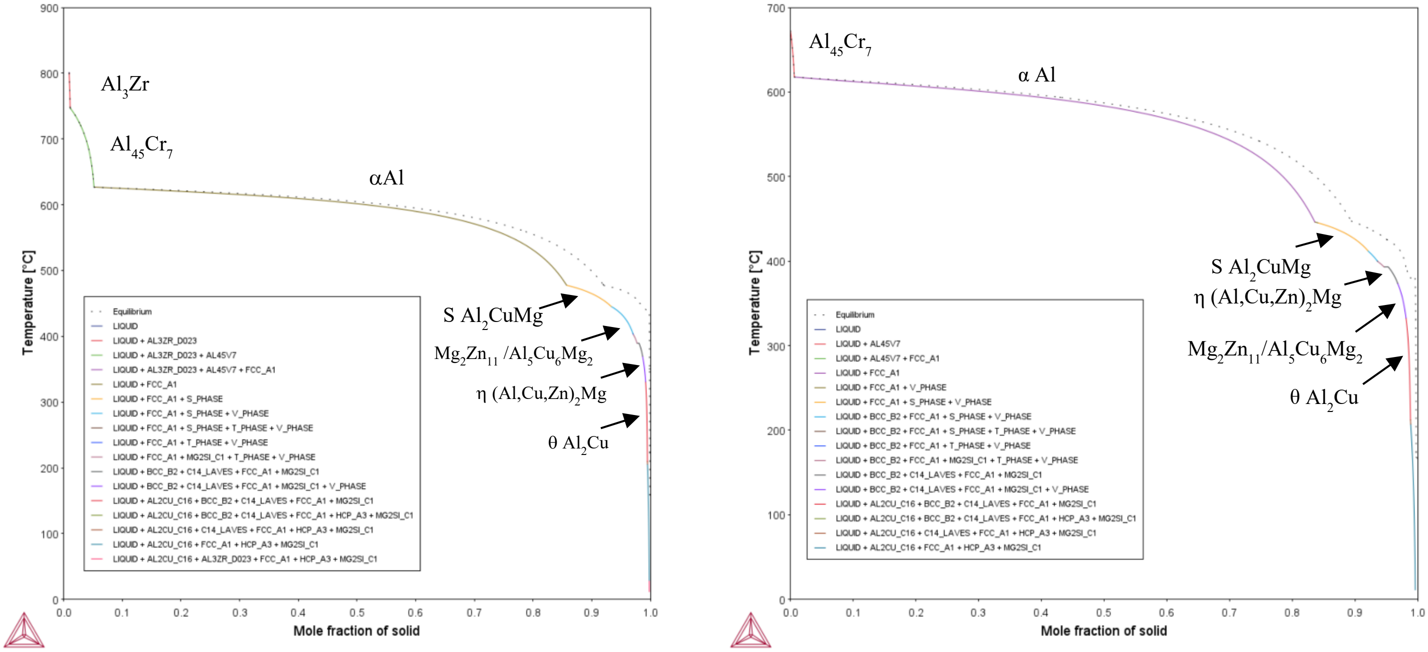

(c)

Al-4.1Cu-4.0Zn-2.4Mg-0.7Ag-0.88Ga-0.37In-0.25Sn-1.0Cr-1.0Zr-0.03Ti-0.01V

(d)

Al-4.1Cu-8.0Zn-2.4Mg-2.14Ag-1.75Ga-0.75In-0.5Sn-0.19Cr-0.03Ti-0.01V

Figure A.1. 1. Scheil-Gulliver solidification curves showing the formed phases (a) DA1, (b) DA2, (c) DA3, and (c) DA4.

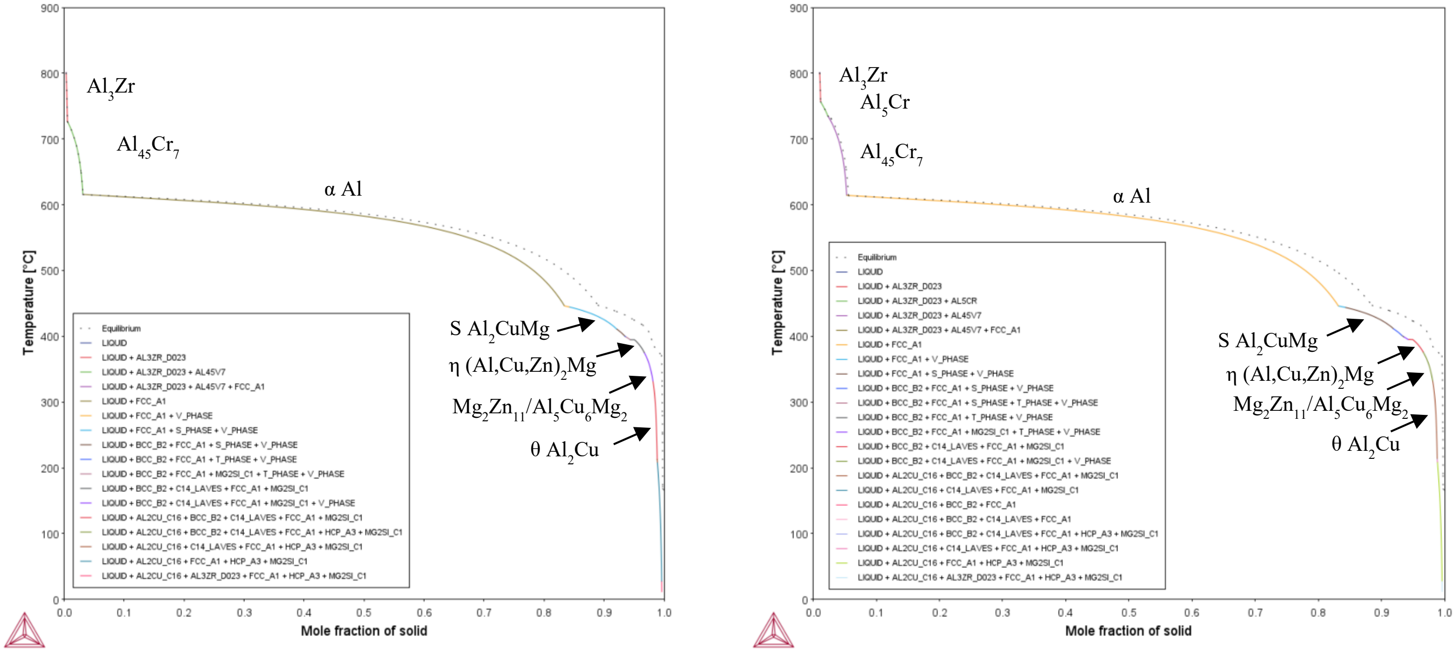

(a)

Al-4.1Cu-8.0Zn-2.4Mg-2.14Ag-1.75Ga-0.75In-0.5Sn-0.6Cr-0.5Zr-0.03Ti-0.01V

(b)

Al-4.1Cu-8.0Zn-2.4Mg-2.14Ag-1.75Ga-0.75In-0.5Sn-1.0Cr-1.0Zr-0.03Ti-0.01V

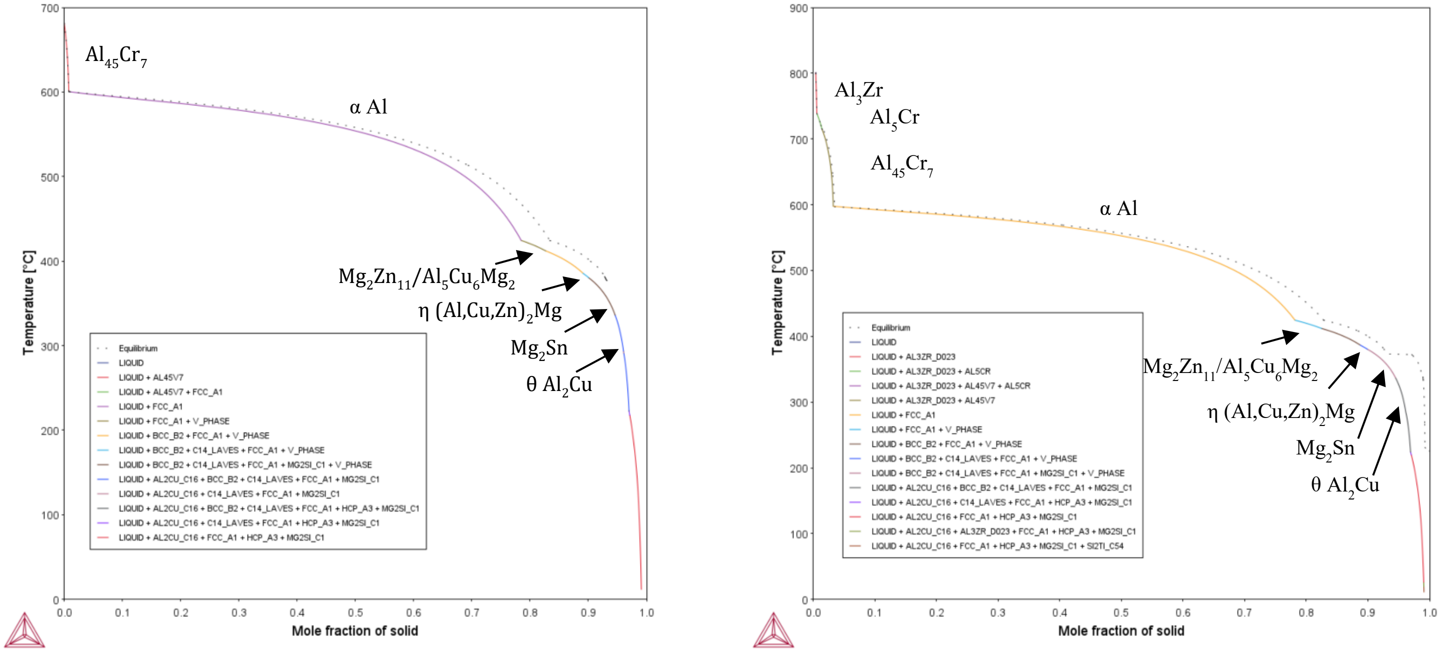

(c)

Al-4.1Cu-12.0Zn-2.4Mg-4.2Ag-3.80Ga-1.5In-0.7Sn-0.19Cr-0.03Ti-0.01V

(d)

Al-4.1Cu-12.0Zn-2.4Mg-4.2Ag-3.80Ga-1.5In-0.7Sn-0.6Cr-0.5Zr-0.03Ti-0.01V

Figure A.1. 2. Scheil-Gulliver solidification curves showing the formed phases (a) DA5, (b) DA6, (c) DA7, and (c) DA8.

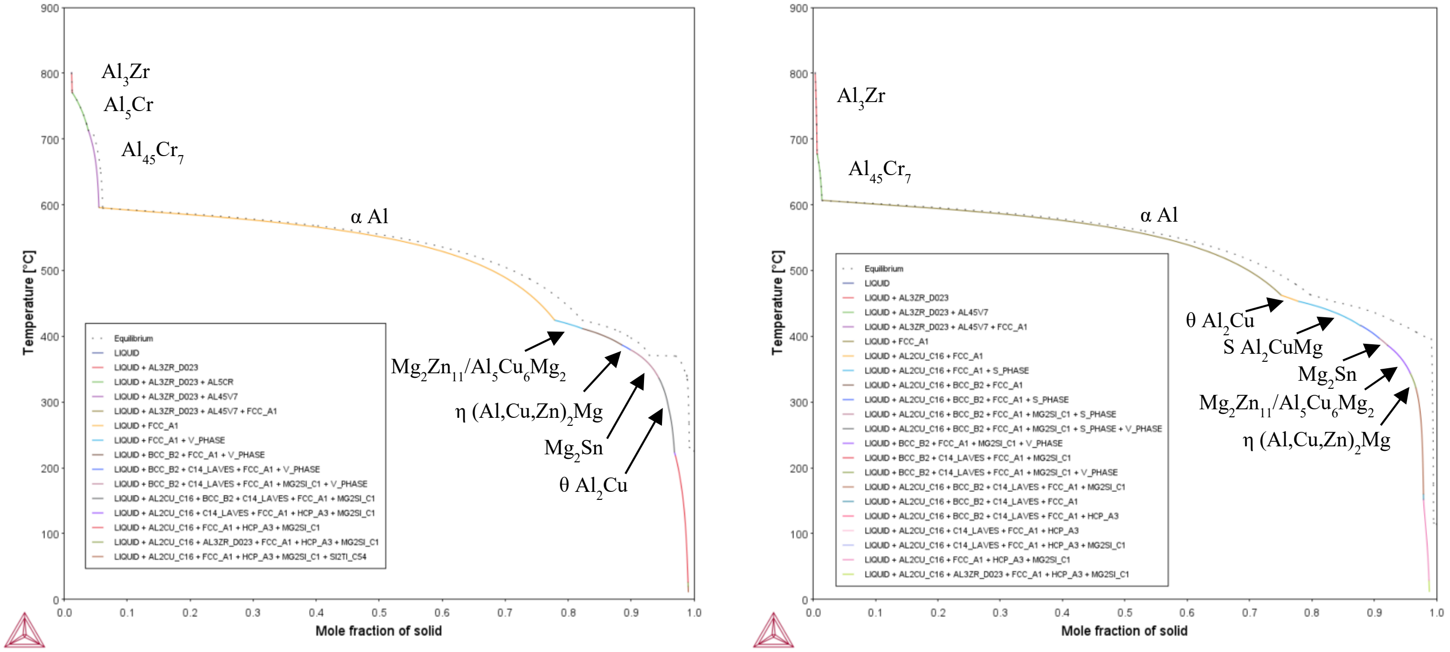

(a) (b)

Al-4.1Cu-12.0Zn-2.4Mg-4.2Ag-3.80Ga-1.5In-0.7Sn-1.0Cr-1.0Zr-0.03Ti-0.01V Al-7.55Cu-4.0Zn-2.4Mg-2.14Ag-3.80Ga-1.5In-0.7Sn-0.19Cr-0.5Zr-0.03Ti-0.01V

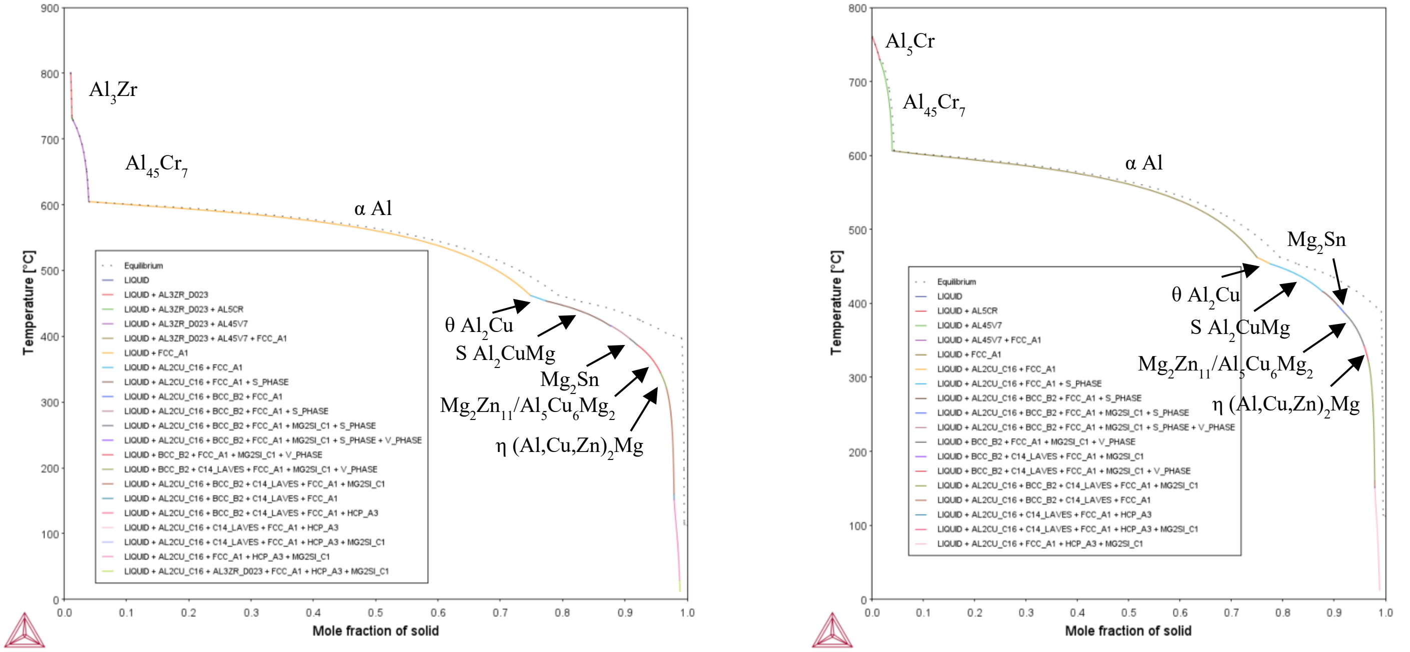

(c) (d)

Al-7.55Cu-4.0Zn-2.4Mg-2.14Ag-3.80Ga-1.5In-0.7Sn-0.6Cr-1.0Zr-0.03Ti-0.01V Al-7.55Cu-4.0Zn-2.4Mg-2.14Ag-3.80Ga-1.5In-0.7Sn-1.0 Cr-0.03Ti-0.01V

Figure A.1. 3. Scheil-Gulliver solidification curves showing the formed phases (a) DA9, (b) DA10, (c) DA11, and (c) DA12.

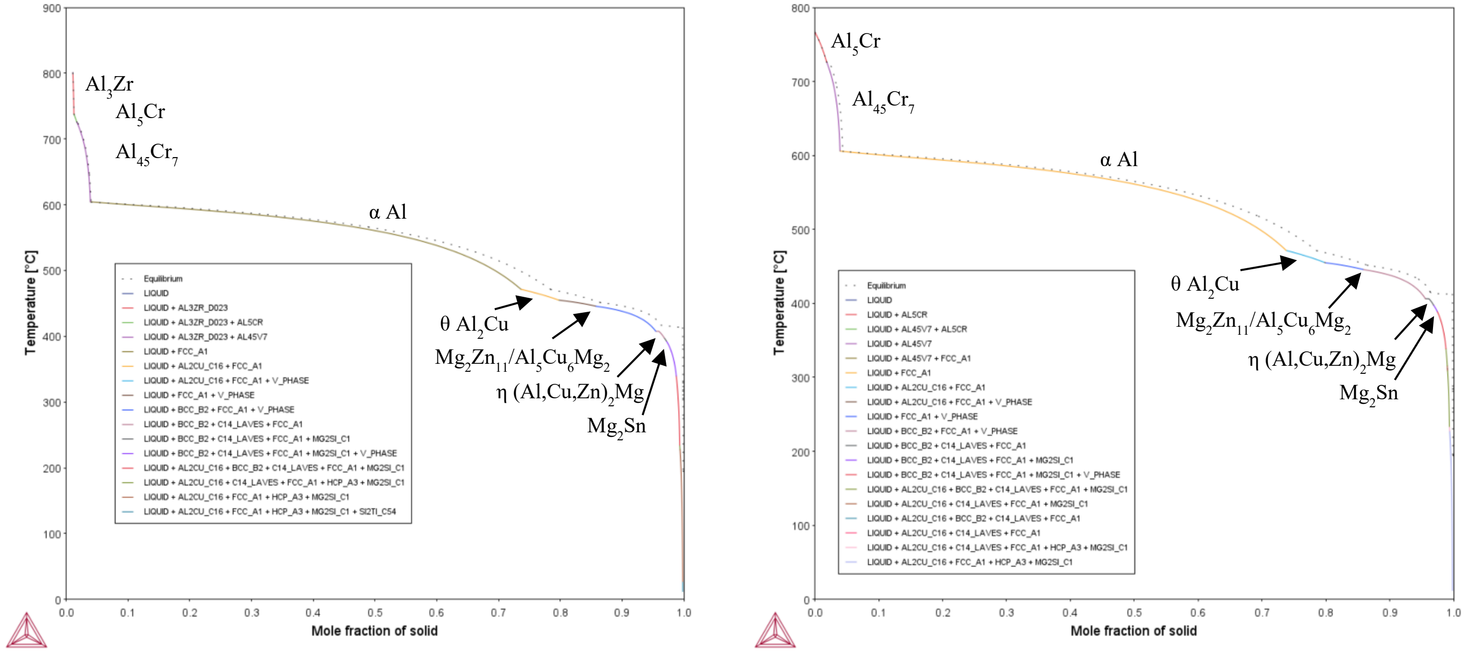

(a)

Al-7.55Cu-8.0Zn-2.4Mg-4.2Ag-0.88Ga-0.37In-0.25Sn-0.6Cr-1.0Zr-0.03Ti-0.01V

(b)

Al-7.55Cu-8.0Zn-2.4Mg-4.2Ag-0.88Ga-0.37In-0.25Sn-1.0Cr-0.03Ti-0.01V

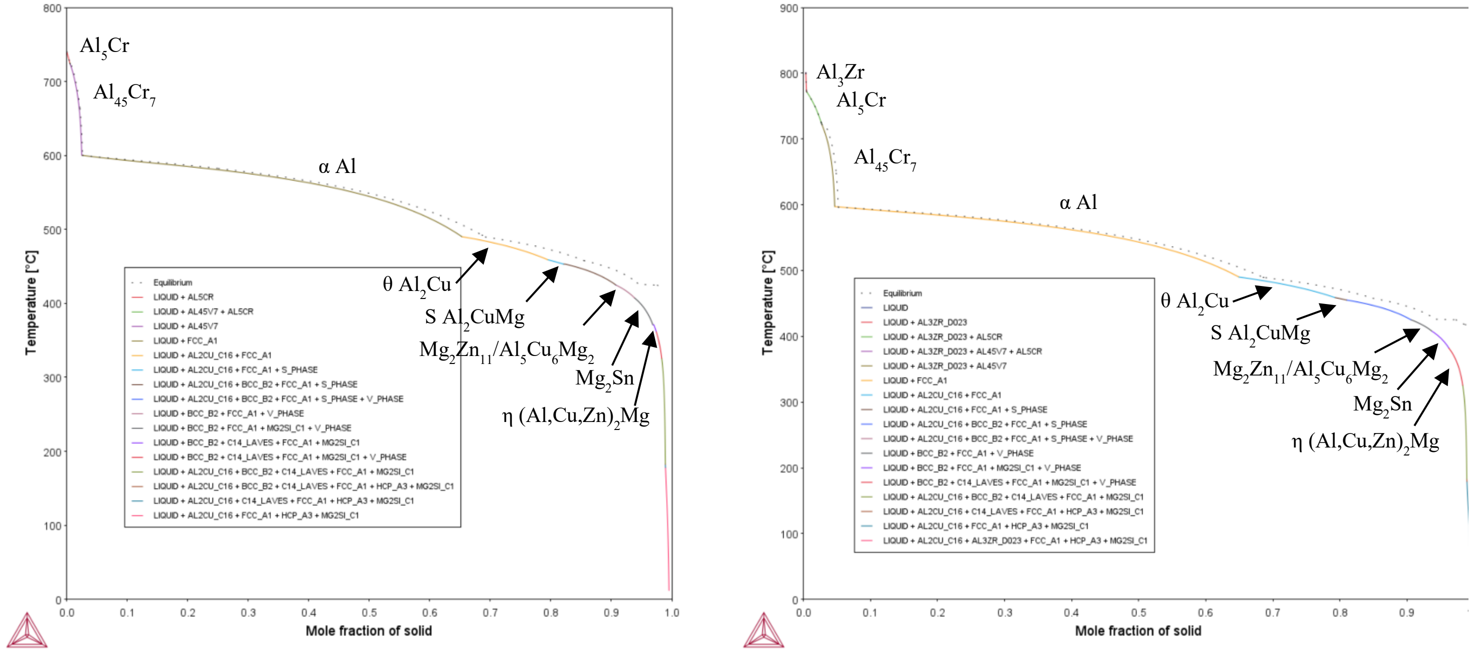

(c)

Al-11Cu-4.0Zn-2.4Mg-4.2Ag-1.75Ga-0.74In-0.5Sn-0.6Cr-0.03Ti-0.01V

(d)

Al-11Cu-4.0Zn-2.4Mg-4.2Ag-1.75Ga-0.74In-0.5Sn-1.0Cr-0.5Zr-0.03Ti-0.01V

Figure A.1. 4. Scheil-Gulliver solidification curves showing the formed phases (a) DA14, (b) DA15, (c) DA20, and (c) DA21.

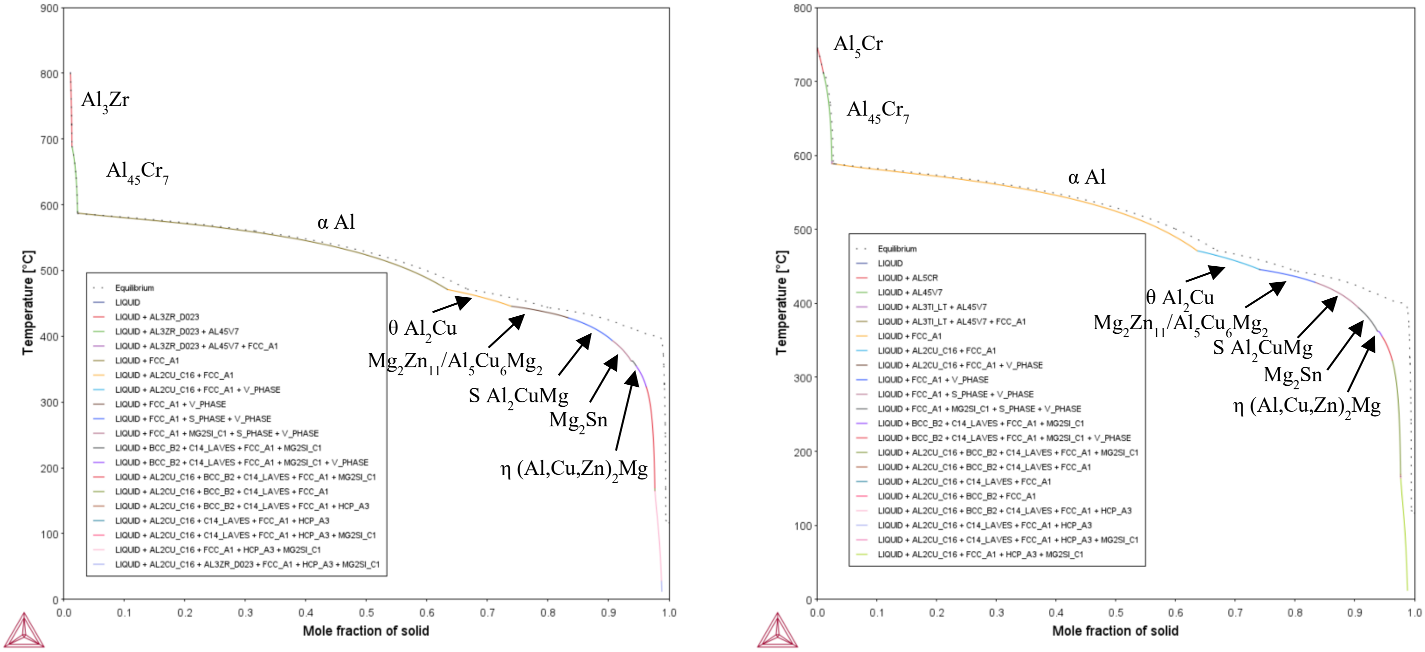

(a)
Al-11Cu-8.0Zn-2.4Mg-0.7Ag-3.8Ga-1.5In-0.7Sn-0.19Cr-1.0Zr-0.03Ti-0.01V

(b)
Al-11Cu-8.0Zn-2.4Mg-0.7Ag-3.8Ga-1.5In-0.7Sn-0.6Cr-0.03Ti-0.01V

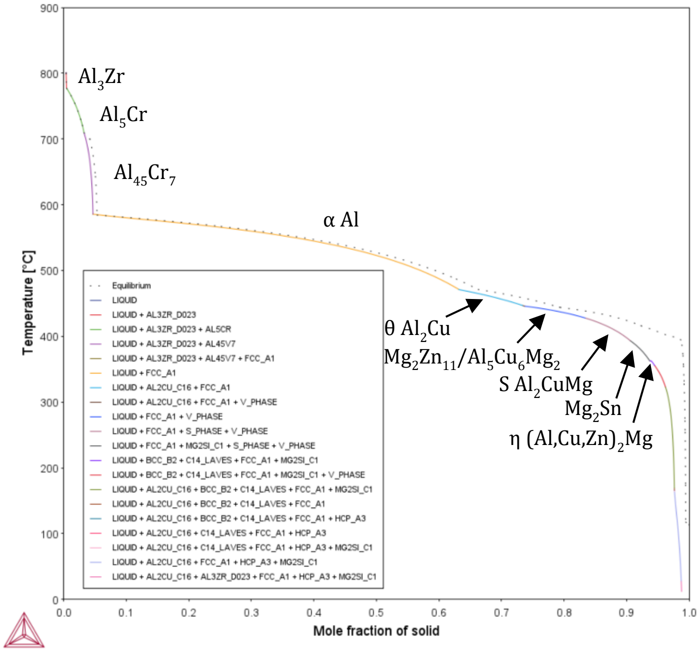

(c)
Al-11Cu-8.0Zn-2.4Mg-0.7Ag-3.8Ga-1.5In-0.7Sn-1.0Cr-0.5Zr-0.03Ti-0.01V

Figure A.1. 5. Scheil-Gulliver solidification curves showing the formed phases (a) DA22, (b) DA23, and (c) DA24.

A.2 Additional SEM images and EDS maps for DA13, DA18, DA25, and DA27

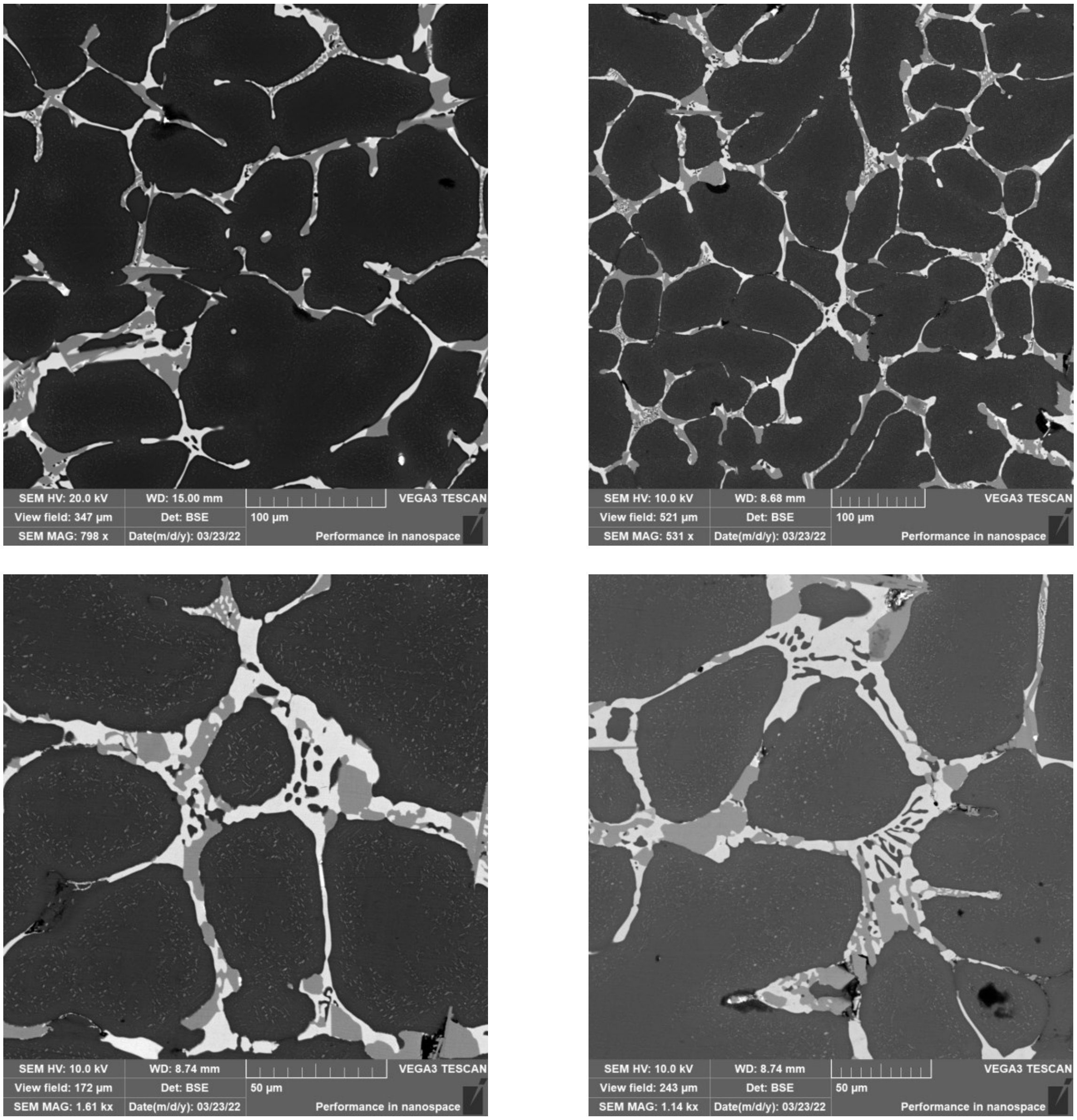

Figure A.2. 1. SEM images for DA13.

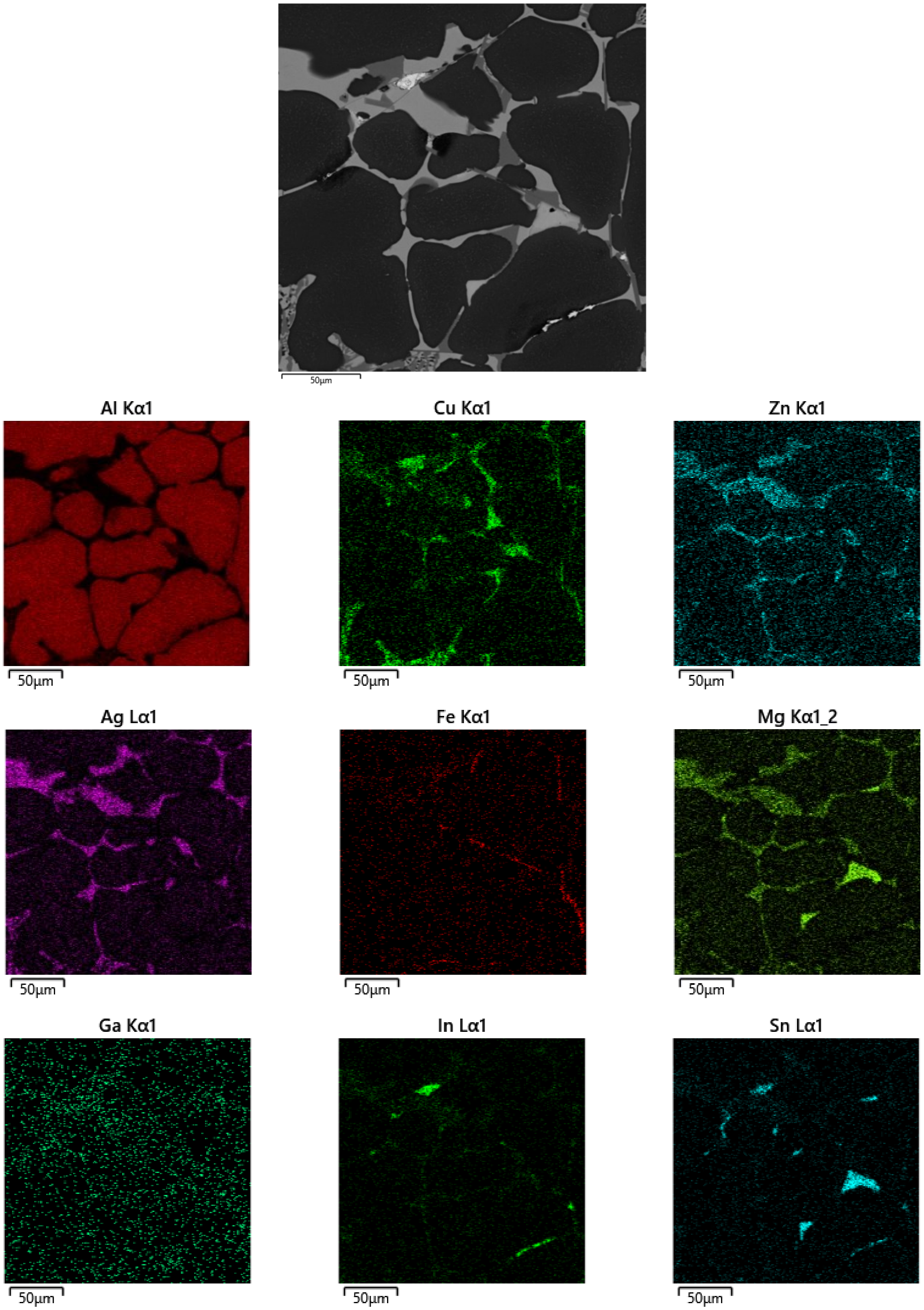

Figure A.2. 2. EDS map for DA13.

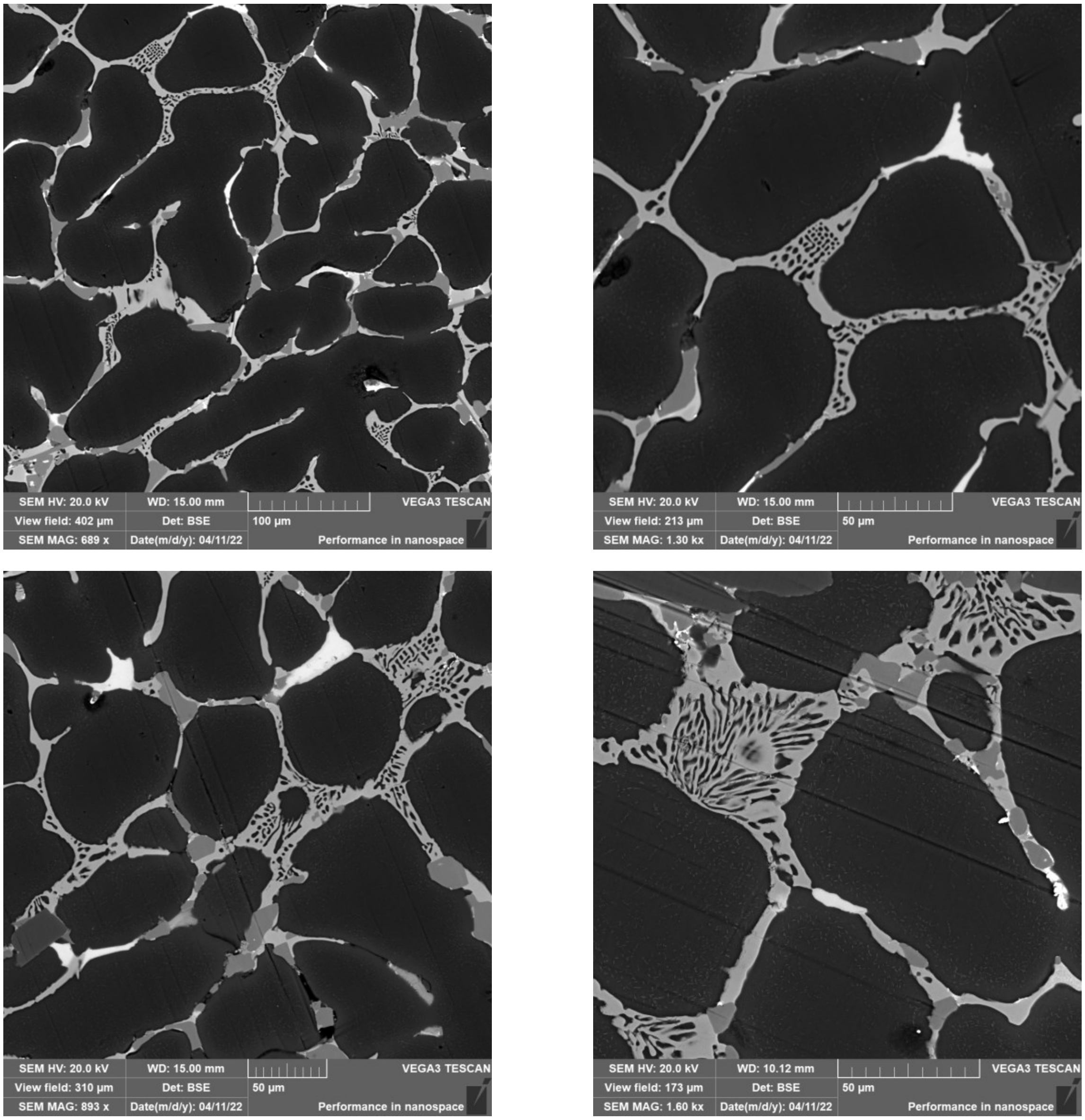

Figure A.2. 3. SEM images DA18.

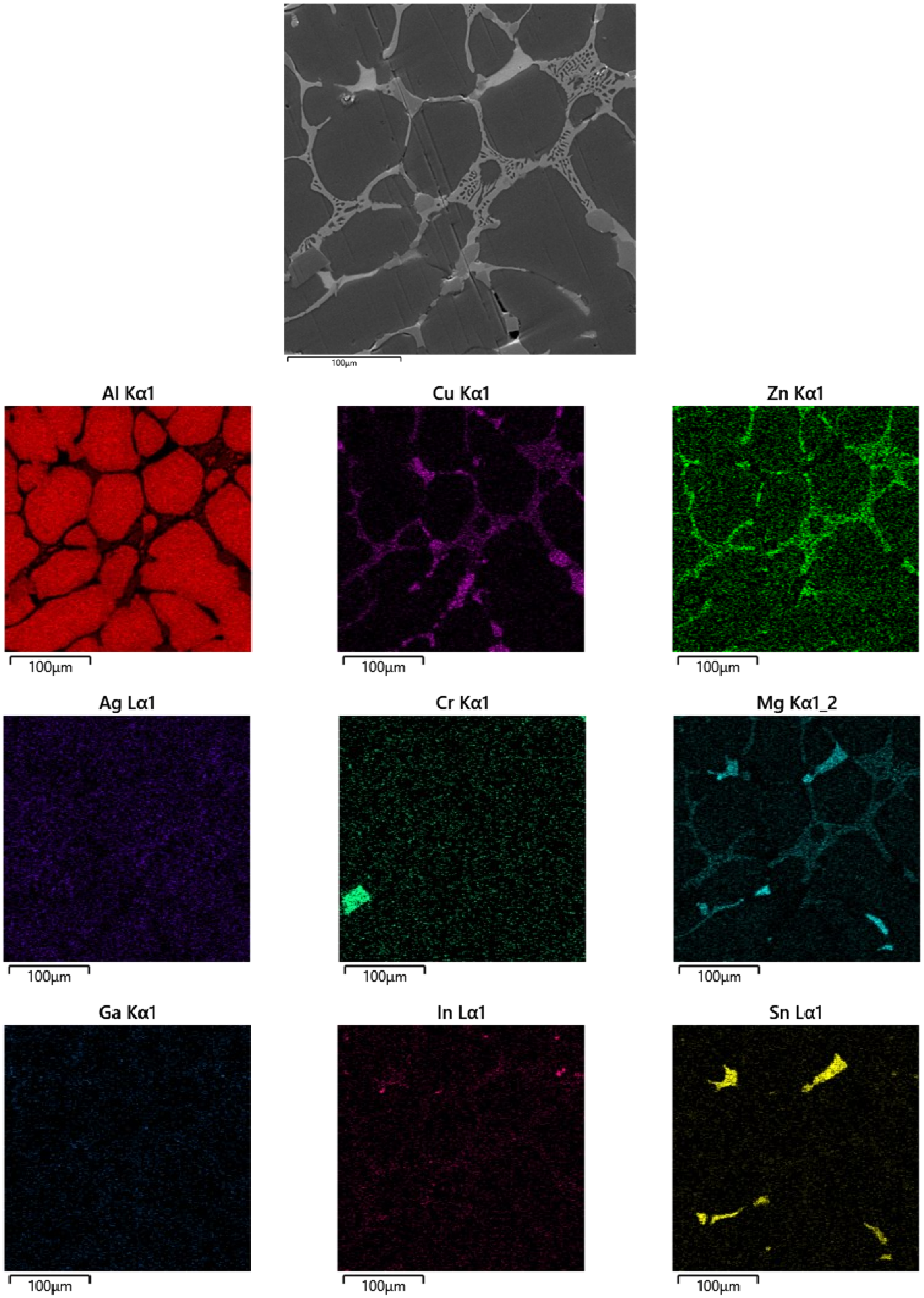

Figure A.2. 4. EDS maps DA18.

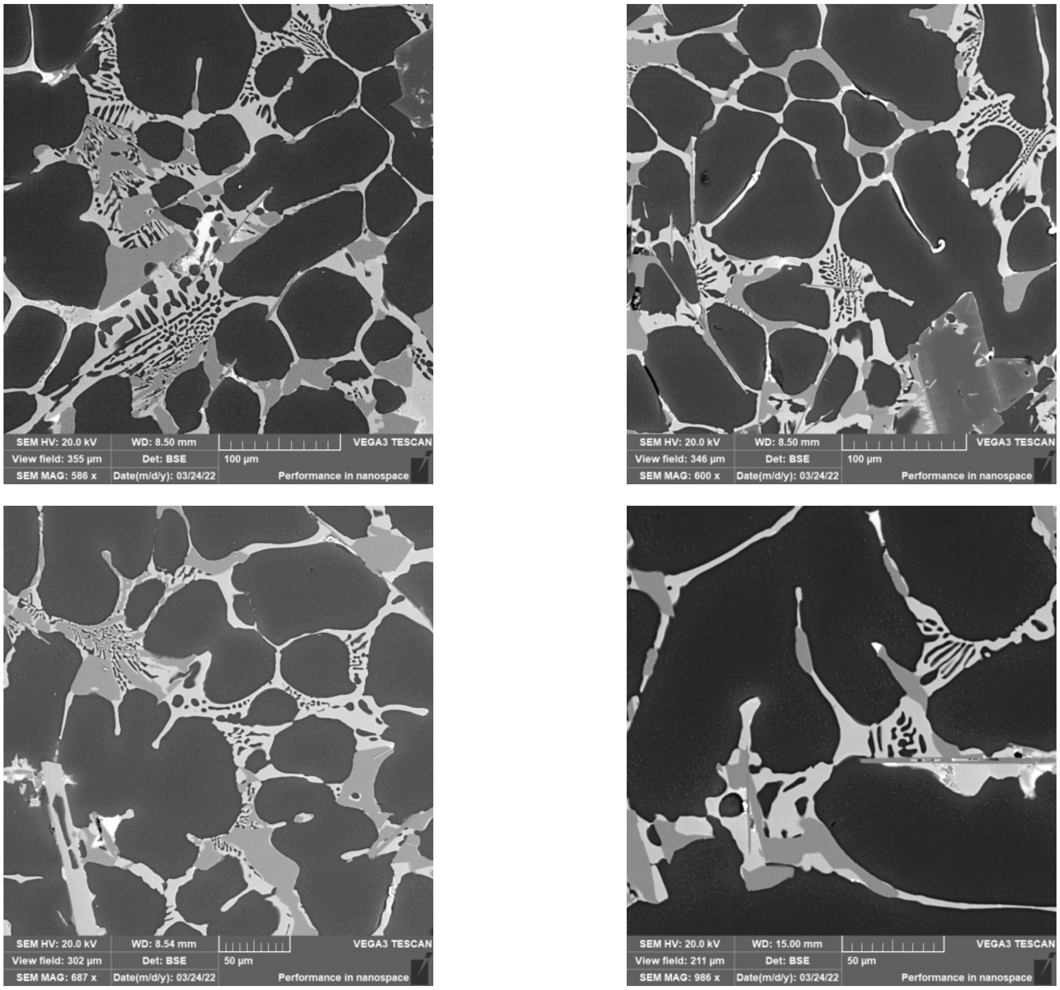

Figure A.2. 5. SEM images for DA25.

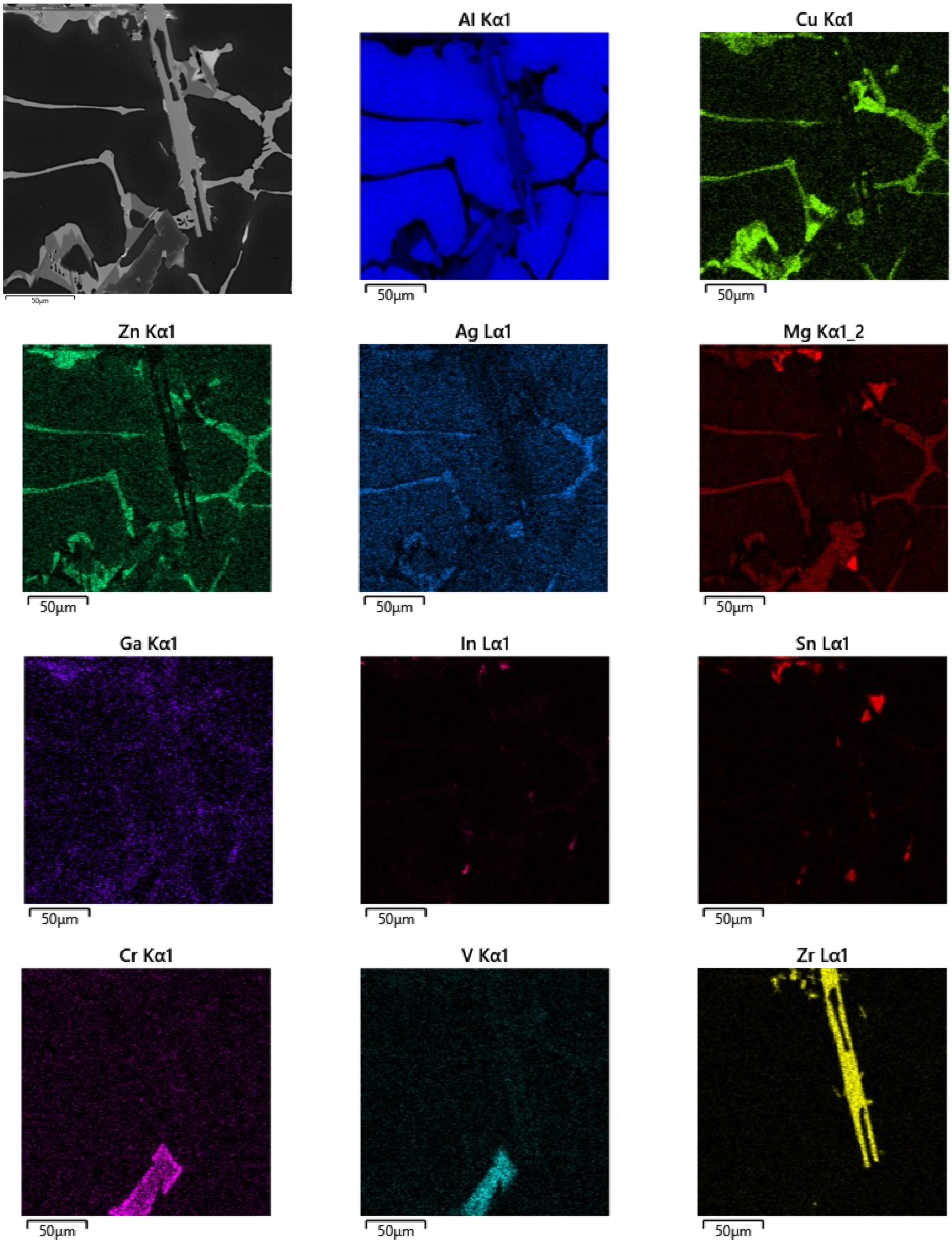

Figure A.2. 6. EDS maps for DA25.

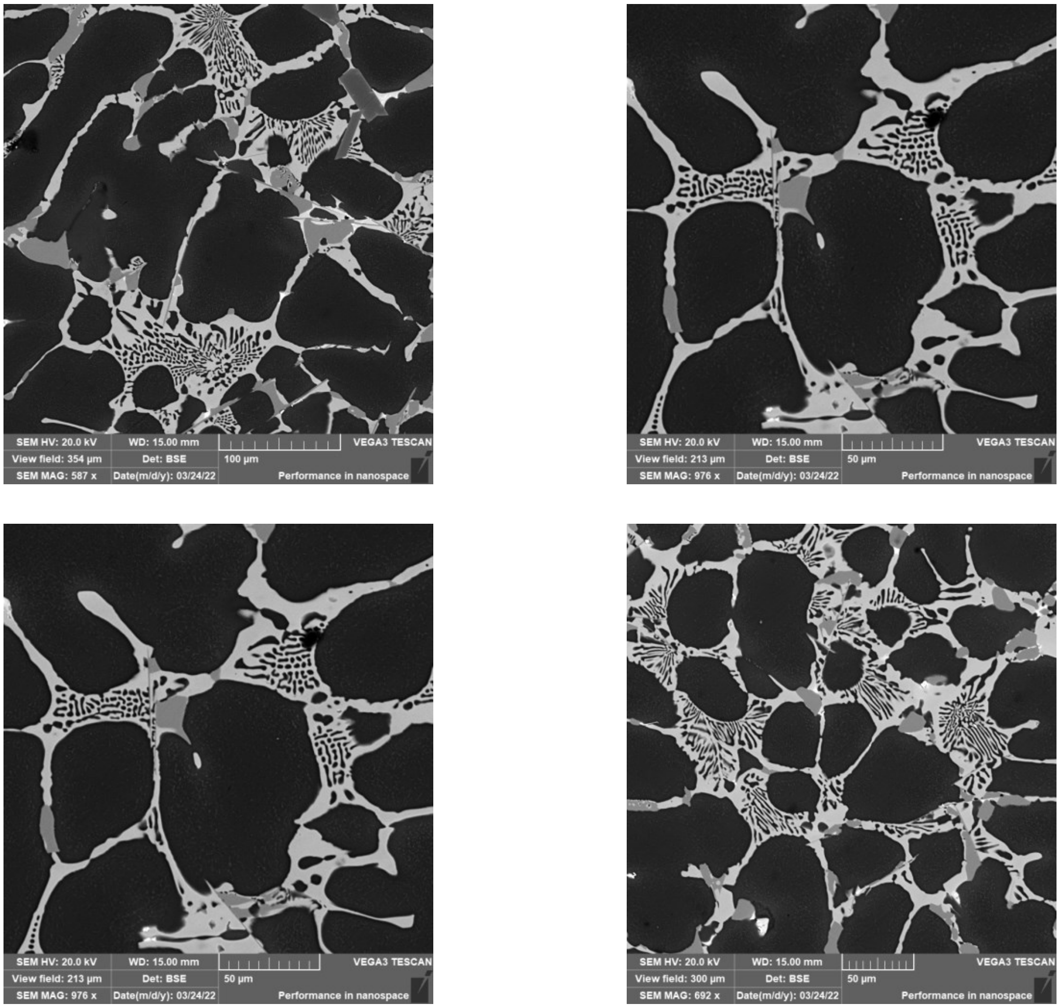

Figure A.2. 7. SEM imaged for DA27.

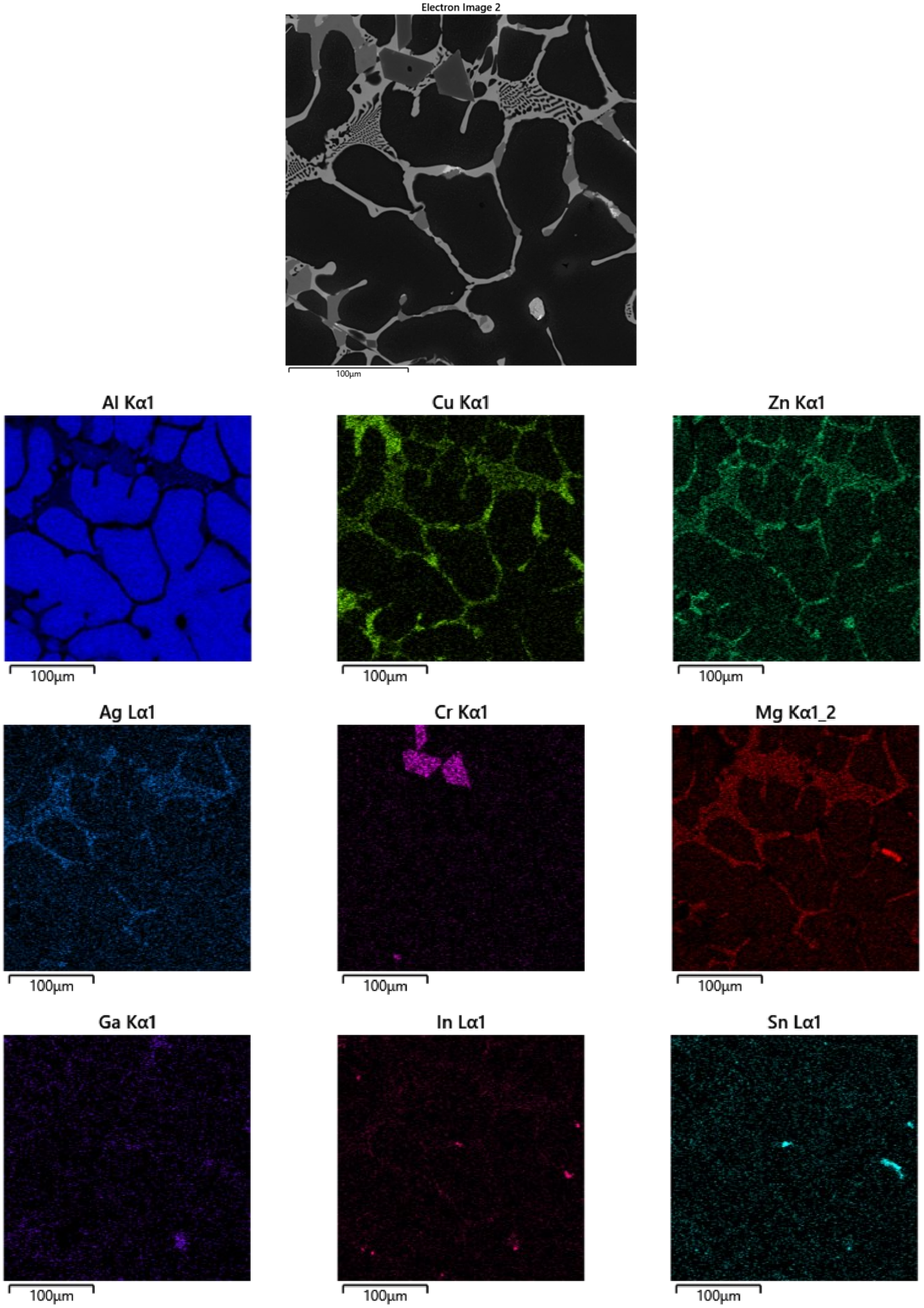

Figure A.2. 8. EDS maps for DA27

Appendix B – Preliminary results for future directions

This section consists of a preliminary study for suggested future work on DA18 as well as a proposal for a new DA composition.

B.1 Preliminary study on further improving DA18 dissolvability.

B.2 Proposal of a new DA chemistry based on the presented results.

B.1 Preliminary study on further improving DA18 dissolvability.

This preliminary experiment aims to investigate the possibility to increase the corrosion rate of the DAs considered in this study. The bases of this study related to the influence of grain size on the corrosion rate. It was found in the literature that the grain size of Al-Ga-In-Sn alloys can be reduced by introducing Cu and/or Mg into the alloy [1]. However, the introduction of such alloying elements interfered with the formation of In-containing phases, thus, reducing their phase fraction (i.e., hindering the reactivity of the alloys). This was also explained by the formation of other intermetallic phases such as θ-Al_2Cu which reduced the contact area between Al and In-containing phases.

However, the reduction of grain size could also be achieved without altering the chemistry of the alloy. Quenching DA18 at a higher temperature around 480 °C reduced the alloy grain size by half. Figures B.1.1 (a) and (b) present the as-cast microstructure of DA18 at different quenching temperatures. Figure B.1.2 shows the EDS maps and the elemental distribution.

---

[1] He, Tiantian, et al. "Effect of different Cu contents on the microstructure and hydrogen production of Al–Cu-Ga-In-Sn alloys for dissolvable materials." *Journal of Alloys and Compounds* 821 (2020): 153489.

He, Tiantian, et al. "Microstructure and hydrogen production of the rapidly solidified Al–Mg-Ga-In-Sn alloy." *Journal of Alloys and Compounds* 827 (2020): 154290.

Wang, M. F., et al. "Microstructure, mechanical properties and corrosion behavior of Al-Cu-Mg-Sn-Ga-In alloy." *Journal of Alloys and Compounds* 776 (2019): 172-180.

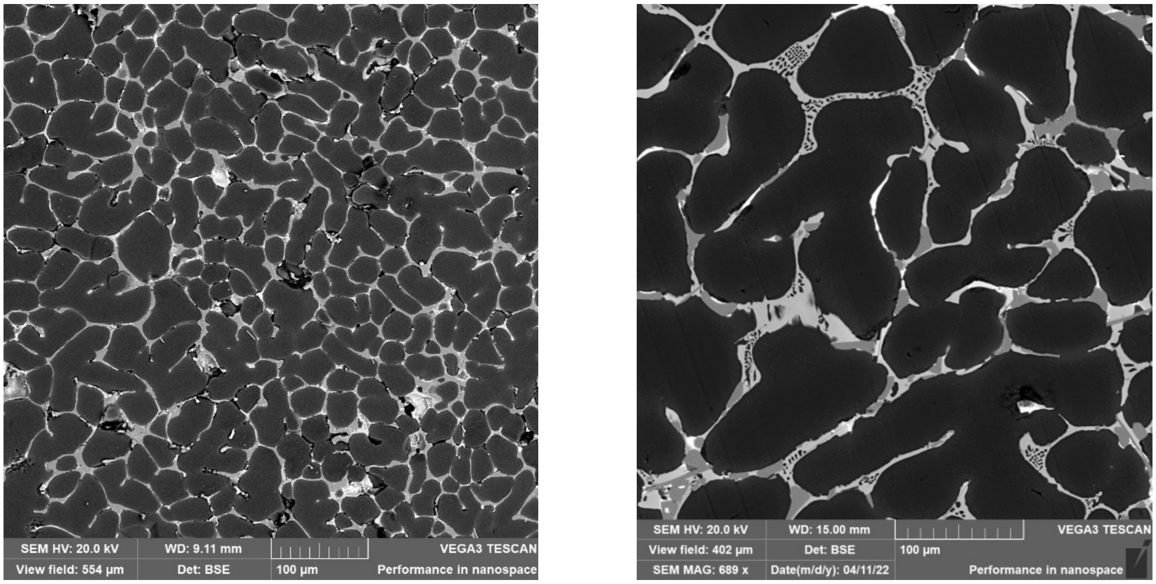

(a) (b)

Figure B.1. 1. SEM images showing the as-cast microstructure of DA18 (a) quenched at 480 °C and (b) quenched at 300 °C.

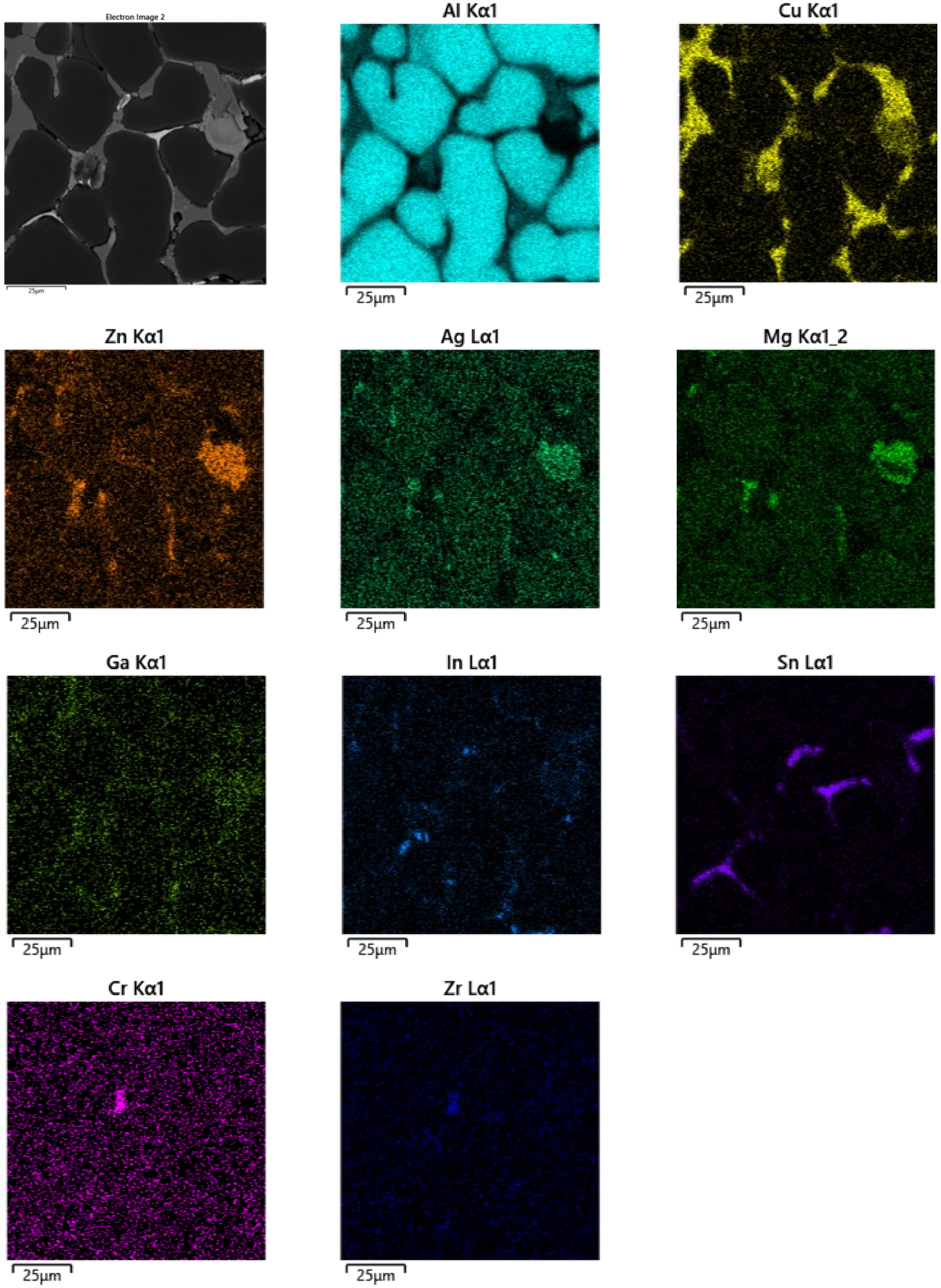

Figure B.1. 2. EDS maps for DA18 quenched at 480 °C.

The dissolution rate of DA18 improved significantly by a factor of 4.56 (i.e., 811.18 compared to 177.76 mg/cm^2 h). Compared to the reference DAs, the enhanced corrosion rate of DA18 is 23.32 and 13.04 times the reference Al-based and Mg-based DAs, respectively. Figure B.1.3 (a) and (b) shows the state of two samples of DA18. The sample in Figure (a) was surprisingly dissolved completely, thus, the calculation for corrosion rate was not possible. A repeated successful run was performed with a bigger sample size to accommodate the fast dissolution rate. Both samples were severely corroded. The fast dissolution could also be explained by the dissociation of Sn from Mg as Figure B.1.2 shows. In this case, Mg does not alter the composition of GIS phases at the grain boundaries.

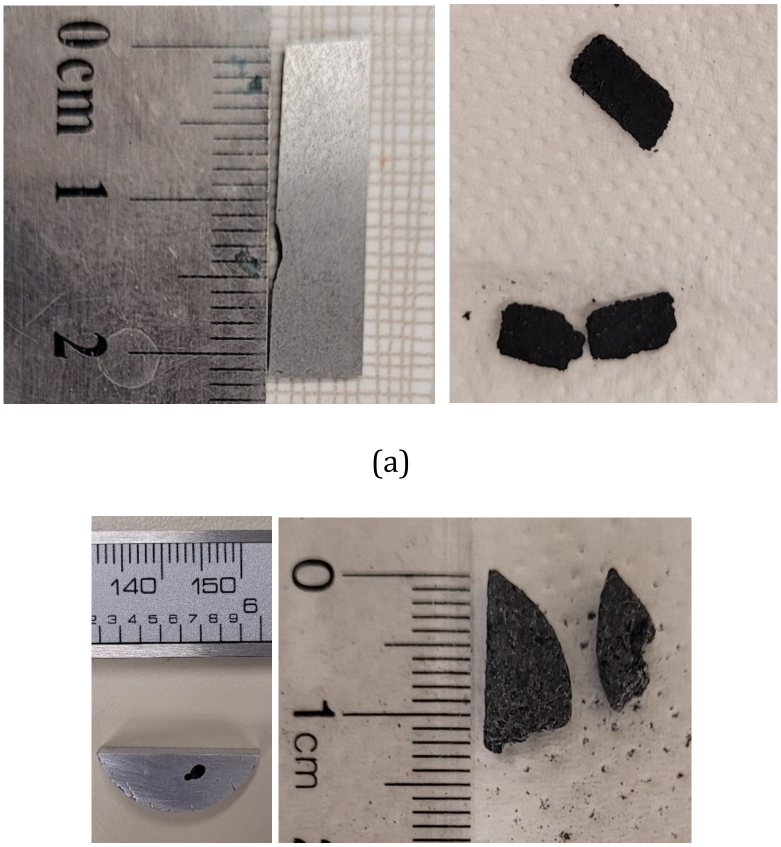

(a)

(b)

Figure B.1. 3. Presentation of the state of DA18 samples after immersion in 0.59 M KCl solution at 90 °C.

In terms of mechanical properties, even though the grain size decrease, further investigations should be carried out as the alloys contain low intermetallic phases. However, even if the mechanical properties of the alloy were not desirable, reducing the low melting point elements would help in improving the mechanical properties.

B.2 Proposal of a new DA chemistry based on the presented results.

Examining the influence of each alloying element presented in Section 4.6, it is possible to increase the mechanical properties by adjusting the DAs chemistry. The composition of the new DA is given in Table B.2.1. The proposed alloy has lower Cr, Zr, and Cu content to prevent the coarsening of their corresponding intermetallic phases. GIS content is also reduced to reduce the content of the low intermetallic phases, giving away some of the dissolvability.

Table B.2. 1. Composition of a proposed DA (wt.%).

	Cu	Zn	Mg	Ag	GIS	Cr	Zr	Ti	Al
Proposed DA	2.00	8.00	2.40	1.00	2.00	0.09	0.09	0.03	Bal

Similar studies on alloys close to the proposed DA composition were reported in the literature [2]. Table B.2.2 lists a review of the main findings.

Table B.2. 2. Mechanical properties of Al-Zn-Mg-Cu alloys close in composition to the proposed DA.

Alloys	**Cu**	**Zn**	**Mg**	**Zr**	**Cr**	**Er**	**Al**	**UTS (Mpa)**	**Reference**
1	1.91	11.66	2.47	-	-	-	Bal.	748	Ziyong et al. (2013)
2	2.10	8.49	2.39	-	-	-	Bal.	704	Fang et al. (2014)
3	2.16	8.53	2.16	0.16	0.17	0.28	Bal.	744	Fang et al. (2014)

---

[2] Mostafapoor, Saman, Mehdi Malekan, and Masoud Emamy. "Effects of Zr addition on solidification characteristics of Al–Zn–Mg–Cu alloy using thermal analysis." *Journal of Thermal Analysis and Calorimetry* 134.3 (2018): 1457-1469.

Chen, Ziyong, Yuanke Mo, and Zuoren Nie. "Effect of Zn content on the microstructure and properties of super-high strength Al-Zn-Mg-Cu alloys." *Metallurgical and Materials Transactions A* 44.8 (2013): 3910-3920.

Based on the present work results, it is believed that the proposed DA will have enhanced mechanical properties for the downhole application.